

**STRANGE PARTICLES  
FROM  
DENSE HADRONIC MATTER**

JOHANN RAFELSKI

Department of Physics, University of Arizona  
Tucson, AZ 85721

JEAN LETESSIER and AHMED TOUNSI

Laboratoire de Physique Théorique et Hautes Energies  
Université Paris 7, Tour 24, 2 Pl. Jussieu, F-75251 Cedex 05, France

*(Received April 3, 1996)*

**Abstract**

After a brief survey of the remarkable accomplishments of the current heavy ion collision experiments up to 200A GeV, we address in depth the role of strange particle production in the search for new phases of matter in these collisions. In particular, we show that the observed enhancement pattern of otherwise rarely produced multi-strange antibaryons can be consistently explained assuming color deconfinement in a localized, rapidly disintegrating hadronic source. We develop the theoretical description of this source, and in particular study QCD based processes of strangeness production in the deconfined, thermal quark-gluon plasma phase, allowing for approach to chemical equilibrium and dynamical evolution. We also address thermal charm production. Using a rapid hadronization model we obtain final state particle yields, providing detailed theoretical predictions about strange particle spectra and yields as function of heavy ion energy. Our presentation is comprehensive and self-contained: we introduce in considerable detail the procedures used in data interpretation, discuss the particular importance of selected experimental results and show how they impact the theoretical developments.

PACS numbers: 25.75.+r, 12.38.Mh, 24.85.+p

(1037)

## Contents

<b>1</b>	<b>Introduction</b>	<b>1039</b>
<b>2</b>	<b>Diagnostic tools</b>	<b>1044</b>
2.1	Principal methods . . . . .	1044
2.2	Particle spectra . . . . .	1045
2.3	Electromagnetic probes . . . . .	1049
2.4	Charmonium suppression . . . . .	1051
2.5	HBT-interferometry . . . . .	1052
<b>3</b>	<b>Strangeness</b>	<b>1053</b>
3.1	Properties of strange particles . . . . .	1053
3.2	Diagnostic signatures . . . . .	1058
3.3	Highlights of strangeness experimental results . . . . .	1060
<b>4</b>	<b>Thermal fireball</b>	<b>1064</b>
4.1	Comparison to kinetic theory approach . . . . .	1064
4.2	Thermal parameters . . . . .	1065
4.3	Stages of fireball evolution . . . . .	1067
4.4	Analysis of properties of the strange particle source . . . . .	1070
<b>5</b>	<b>Thermal QGP fireball</b>	<b>1075</b>
5.1	QGP equations of state . . . . .	1075
5.2	Initial conditions and fireball evolution . . . . .	1078
5.3	Difference between AGS and SPS energy range . . . . .	1084
<b>6</b>	<b>Thermal flavor production</b>	<b>1086</b>
6.1	Population evolution . . . . .	1086
6.2	Thermal strangeness production . . . . .	1090
6.3	Running $\alpha_s$ and flavor production . . . . .	1095
6.4	Thermal charm production . . . . .	1103
<b>7</b>	<b>Evolution of heavy quark Observables</b>	<b>1105</b>
7.1	Flow model . . . . .	1105
7.2	Dynamical description of observables in the fireball . . . . .	1108
7.3	Strangeness and charm in final state . . . . .	1112
<b>8</b>	<b>QGP hadronization</b>	<b>1119</b>
8.1	Hadronization constraints . . . . .	1119
8.2	Entropy content of heavy ion collisions . . . . .	1124
8.3	Final state strange baryon yields . . . . .	1127
<b>9</b>	<b>Summary and conclusions</b>	<b>1133</b>

## 1 Introduction

Our interest is to study under laboratory conditions matter as it existed during the era of the early Universe at which temperatures were in excess of 200 MeV, thought to be less than  $10\ \mu\text{s}$  after the big bang. Beams of heaviest nuclei at relativistic energies are the tools in this research program: in nuclear heavy ion collisions the participating strongly interacting hadronic nuclear matter is compressed and heated. Unlike the early Universe, the volume occupied by such laboratory ‘micro bang’ is small, see Fig. 1. However, our hope and expectation is that collisions of largest nuclei which are now studied experimentally will allow us to explore conditions akin to infinite systems of hot hadronic matter. Another difference with the early Universe condition is, as shown in Fig. 1, that though one of the most characteristic features of these heavy ion collisions is the formation of many new particles, their number per nucleon (baryon) remains considerably smaller than was present at the low baryon density of matter present in the early Universe. Much of the theoretical effort in this field is thus devoted to the understanding and interpretation of the experimental data and in particular their extrapolation to conditions of long lived, statistically equilibrated matter with low baryon density.

The great variety of hadronic particles known (mesons, baryons) implies that the structure and properties of their source will be very rich, and could comprise some new and unexpected phenomena. Our present discussion will, however, be limited to consideration of just two model phases of highly excited hadronic matter:

1. the conventional, confined phase we shall call hadronic gas (HG), consisting of hadronic particles of different type, (including short lived resonances), such as  $\pi$ ,  $\rho$ ,  $N$ ,  $\Delta$ , etc., with masses and degeneracies in most cases well known. Along with Hagedorn [1], we presume that particle interactions in HG are accounted for by giving the resonances the status of independent fractions in the gas;
2. the deconfined phase will be seen as a liquid of quarks and gluons, interacting perturbatively, an approach which is properly justified only in the limit of very high energy densities. We shall call this phase the quark-gluon plasma (QGP). Our specific objective is to discover and explore this new form of matter [2].

There is today considerable interest in the study of the transformation of strongly interacting matter between these two phases. Considerable theoretical effort is committed in the framework of finite temperature lattice gauge theory [3] to perform simulations with the objective to obtain a better understanding of the properties of quantum chromodynamics (QCD)

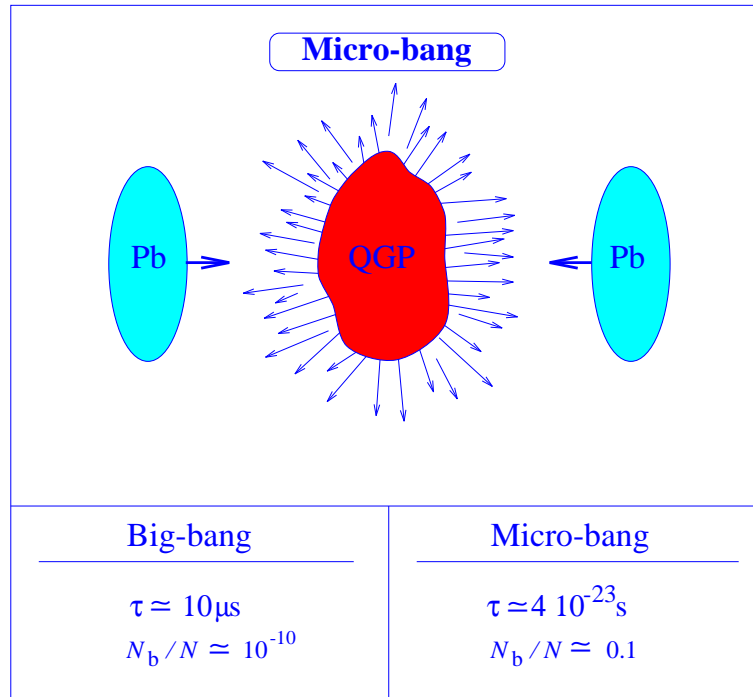


Figure 1: Qualitative illustration of the relativistic nuclear collision and the differences between the Big-Bang and Micro-Bang.

at finite temperature. In analogy to water-vapor transition we expect and indeed see that two phases of hadronic matter are separated by a first order phase transition. However, the theoretical simulations also suggest that it could well be that there is no transition, just a phase cross-over, similar to the situation prevailing in the atomic gas transition to electron-ion plasma. A comparison between theory and experiment will be always subject to the constraint that a true phase transitions cannot develop in a finite system. However, the number of accessible degrees of freedom that are being excited in collisions of heavy nuclei is very large, and this should allow us to explore the properties of the true infinite matter phase transition using finite nuclei as projectiles and targets. It is for this reason that beams of largest nuclei are the required experimental tools in this research program.

Another way to look at the phase transformation between the two prototype phases, HG and QGP, arises from the consideration of the nature and in particular the transport properties of the vacuum state of strong interactions: in the QGP phase (the ‘perturbative vacuum state’) it is al-

lowing for the free propagation of quark and gluon *color* charges. The ‘true vacuum’ in which we live is a color charge insulator, only the color neutral mesons and baryons can propagate. Because at high temperature we cross to the conductive phase, it is possible to consider the change in the properties of the vacuum akin to the situation with normal matter. Moreover, from the theoretical point of view, the observation of the ‘vacuum melting’ and the study of the properties of the perturbative and true vacuum is the primary objective of the nucleus-nucleus high energy collision experimental program — high energy nuclear collisions are today the only known laboratory method allowing the study of extended space-time regions containing a locally modified vacuum state.

Inside the domain of perturbative vacuum, at sufficiently high excitation energy we expect to encounter a quantum gas of quarks and gluons subject to the QCD perturbative interactions characterized by the (running) coupling constant  $\alpha_s$ . Even though the strength of the QCD interactions is considerably greater than the strength of electromagnetic interactions,  $\alpha_{\text{QED}} = 1/137$ , the moderate magnitude  $\alpha_s/\pi \leq 0.3$  at the energy scales corresponding to temperatures of  $T \simeq 250$  MeV should permit us to study the quark matter in a first estimate of its properties, as if it consisted of a gas of quarks and gluons interacting perturbatively. We will consider in this way the strangeness production, and also use perturbative expressions in  $\alpha_s$  to improve the free quantum gas equations of state of quarks and gluons. We use the analytical expressions up to the region of the phase cross-over to the confined hadronic gas world, hoping that the qualitative features of the deconfined phase will be appropriately described in that way. Clearly, this is a domain that will see in future more effort both in terms of improvements of the perturbative expressions, and also due to further exploration of numerical lattice gauge theory results.

Relativistic heavy ion experimental programs at the AGS accelerator at the Brookhaven National Laboratory (BNL) and at the SPS accelerator at the European Center of Nuclear Research (CERN) in Geneva, begun in 1986–87. From the onset of the program it was assumed that the higher the collision energy and the heavier the colliding nuclei, the greater the energy density that could be created and hence more extreme conditions of matter and, e.g., earlier the time since the beginning of our Universe one expects to be able to study. Moreover, it is expected that as the energy and thus the rapidity gap, see Fig. 2, is growing, the chances increase to form a truly baryon-free region on space time, more similar to the conditions prevailing in the early Universe, see Fig. 1. For these reason new facilities were build and before the end of the century, the next generation of experiments will exploit the 100A+100A GeV Relativistic Heavy Ion Collider (RHIC) at BNL, sporting 10 times the CM-energy available today at SPS. The race

is on, and at CERN collisions of heavy ions up to about  $3.5A+3.5A$  TeV will become feasible upon completion of the Large Hadron Collider (LHC). Here yet considerably more extreme conditions should be reached, as the collision energies are 400 times higher than accessible today at SPS. The expected onset of the LHC program follows RHIC schedule by about 7 years.

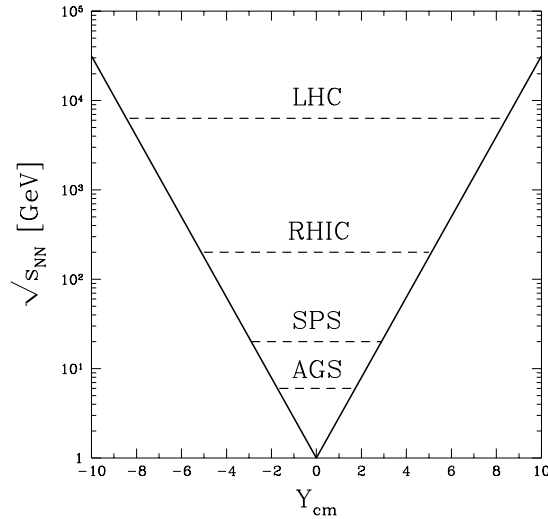


Figure 2: For the nucleon-nucleon center of momentum frame (CM)  $\sqrt{s_{NN}}$  energy the horizontal dashed lines show the maximum rapidity gap between the projectile and target.

In this article we will address mainly strange particle production in collisions at 200A GeV. This center of interest arises from the prediction [6], that the (enhanced) production of (multi)strange antibaryons is specifically related to color deconfinement: in the deconfined QGP phase we find enhanced production of strangeness flavor by thermal glue based processes, leading to high  $\bar{s}$  densities, which in turn leads to highly enhanced production of strange antibaryons. Moreover, the strange antibaryon particle production mechanisms being very different from the usual ones, the behavior of the yields (cross sections) with energy will be shown here to differ considerably from usual expectations. The strange antibaryon particle signature of QGP requires that the transition from the deconfined state to the confined final hadronic gas phase consisting of individual hadrons occurs sufficiently rapidly in order to assure that the memory of the high density of strangeness in the early phase is not erased.

As noted above the enhanced QGP strangeness yield depends to some extent on *thermal* equilibrium gluon collision frequency. Many experimen-

tal results, which we survey in the following suggest that the particles produced in heavy ion collisions are indeed thermal, i.e., that either they have been produced by a thermal source, e.g., in a recombination of thermal constituents, or that they have had time to scatter and thermalize after formation. This means that the thermalization of the energy content in heavy ion reactions is rapid on the time scale of the collision. The required mechanisms of such a rapid thermalization and associated entropy production are today unknown in detail, but plausible given the large number of accessible degrees of freedom in high energy nuclear collisions.

This survey comprises three logical parts

- Experimental results and their analysis,
- Strange quark production and fireball dynamics,
- Final state particle production,

and we outline briefly in the following three paragraphs their respective contents.

It is clearly not possible to present here a comprehensive discussion of the ten years of experimental effort. Rather, in following section 2, we will briefly address the highlights of the experimental results. We then turn to the main topic of the paper in section 3. We introduce strange particle properties, discuss diagnostic tools in more detail and describe the key strangeness (antibaryon) experimental results obtained at SPS in subsection 3.3. In section 4.4 we use the framework of the thermal fireball model to analyze the experimental strange antibaryon ratios and to derive the properties of the source.

In section 5 we develop the equations of state of the QGP-fireball and use these to determine the initial conditions which we expect to be formed in different collisions. Applying conservation of energy and baryon number we also obtain the properties of the fireball at different important instances in its evolution. This is done for all systems studied currently at CERN and BNL experimental facilities and we show that there is a profound difference between the 15A GeV BNL data and the 200A GeV CERN data, which precludes interpretation of the low energy results in terms of a (suddenly disintegrating) QGP-fireball. We then turn our attention in section 6 to a comprehensive study of the QCD-QGP based thermal strangeness production and also discuss briefly the related topics of the thermal charm production. The production of strangeness being strongly dependent on the magnitude of the strong interaction coupling constant, we develop in section 6.3 the renormalization group based description of the appropriate value. In section 7 we explore the variation of the phase space occupancy of strange and charmed particles in the different collision environments.

We now turn our attention to the particle production yields: we discuss the hadronization constraints and parameters in the section 8, and present

the excitation functions of multistrange particles and their ratios in section 8.3. In the final section 9 we give a brief evaluation of our work.

## 2 Diagnostic tools

The reader should be aware from the outset that the observation of a transient new phase of matter, formed and existing just for a brief instant in time, perhaps for no more than  $10^{-22}$ s, is only possible if time reversibility is broken in a shorter time, which is implicitly presumed in this field of research. In our work this is implicitly assumed when we introduce the thermal fireball. However, how this quantum decoherence occurs is one of the great open problems that challenges us today.

### 2.1 Principal methods

Given the assumption of rapid decoherence we can seek accessible observables which can distinguish between micro-bangs comprising the two prototype phases, the HG, or the QGP that subsequently hadronizes. Several useful experimental signatures of dense hadronic matter and specifically the formation and properties of QGP have been now theoretically and experimentally explored. These can be categorized as follows:

#### 1. Electromagnetic probes:

- *direct photons* and *dileptons* [4, 5]. Since quarks are electromagnetically charged, their collisions produce these particles, and the yields are highly sensitive to the initial conditions, for example in relatively ‘cold’ matter the direct photons can be hidden by the  $\pi^0 \rightarrow \gamma\gamma$  process.

#### 2. Hadronic probes:

- *strangeness* [6, 7, 8, 9, 10] (and also charm) is the topic of primary interest here — theoretical considerations show that in the deconfined quark-gluon plasma (QGP) phase high local strange and antistrange particle density is reached permitting abundant formation of strange antibaryons. Furthermore, enhanced production of strangeness is expected comparing QGP-based theoretical strangeness yield to reactions involving cascades of interacting, confined hadrons. Experimental comparison between A–A and N–N collisions reveals indeed such an enhancement at 200 GeV A [11], not seen in N–A interactions at 200 GeV [12].
- Global observables such as *particle abundance* measure the entropy produced in the collision [13, 14].
- *Hanbury Brown-Twiss* (HBT) interferometry allows to determine the particle source size [15].



### 3. Charmonium:

- even though the charmonium state  $c\bar{c} = \Psi$  is a hadronic particle, the way it is proposed as an observable is different from the other hadronic probes, and its small yield also reminds us more of an electromagnetic probe. Once produced in the initial interactions,  $\Psi$  is used akin to X-rays in the Roentgen picture: from the shadows of remaining abundance we seek to deduce a picture of the hadronic matter traversed [16, 5].

We believe that our recent advances [17, 18] in the study of strange particle production have brought about the long aspired substantiation of the formation of deconfined and nearly statistically equilibrated QGP phase at energies available at the SPS accelerator,  $\sqrt{s_{NN}} \simeq 9 + 9$  GeV. We reach this conclusion because the observed abundances of strange antibaryons are closely following the expected pattern characteristic for a rapidly hadronizing deconfined phase, at the same time as an excess of entropy [13] characteristic for melted hidden (color) degrees of freedom is recorded.

We can reach this conclusion because unlike the other particle observables, the final state observable ‘strangeness’ is more than just one average quantity which is enhanced when one compares nucleon-nucleon (N–N) and nucleon-nucleus (N–A) reactions with nucleus-nucleus (A–A) interactions. The interesting aspects of this observable is that there are many different particles, and that certain strange particles (strange antibaryons) appear much more enhanced, since their production is rather suppressed in conventional interactions.

## 2.2 Particle spectra

One of the best studied observables are spectra of hadronic particles — it is convenient to represent these using instead of the longitudinal momentum, the rapidity  $y$  and to use the transverse mass  $m_{\perp}$  instead of the transverse momentum of a particle:

$$y = \frac{1}{2} \ln \left( \frac{E + p_z}{E - p_z} \right), \quad E = m_{\perp} \cosh y, \quad m_{\perp} = \sqrt{m^2 + p_{\perp}^2}, \quad (1)$$

where ‘ $\perp$ ’ is perpendicular to the collision axis ‘ $z$ ’. While  $m_{\perp}$  is invariant under Lorentz transformations along the collision axis, the particle rapidity  $y$  is additive, that is, it changes by the constant value of the transformation for all particles. This allows to choose the suitable (CM — center of momentum) reference frame characterized by its rapidity  $y_{CM}$  for the study of the particle spectra.

Simple kinematic considerations show that the center of momentum frame in nuclear collisions is for symmetric systems just is 1/2 of the pro-

jectile rapidity, and for asymmetric collisions such as S–Au/W/Pb systems with the participating masses  $A_P$ ,  $A_T$  of the projectile and, respectively, target nuclei one finds [20] (neglecting small corrections):

$$y_{\text{CM}} = \frac{y_P}{2} - \frac{1}{2} \ln \frac{A_T}{A_P}. \quad (2)$$

Assuming small impact parameter collisions with a suitable central trigger, all projectile nucleons participate while the target participants  $A_T$  can be estimated from a geometric ‘interacting tube’ model. The geometric picture is well supported by the linear relation of the size of the reaction zone, defined to be  $\sqrt{\sigma}$ , the square root of the reaction cross section, and the geometric size of the interacting nuclei in central collision,  $A_P^{1/3} + A_T^{1/3}$ . We show this in Fig. 3. Once the central rapidity is confirmed experimentally, this allows the determination of the CM-energy involved in the interaction.

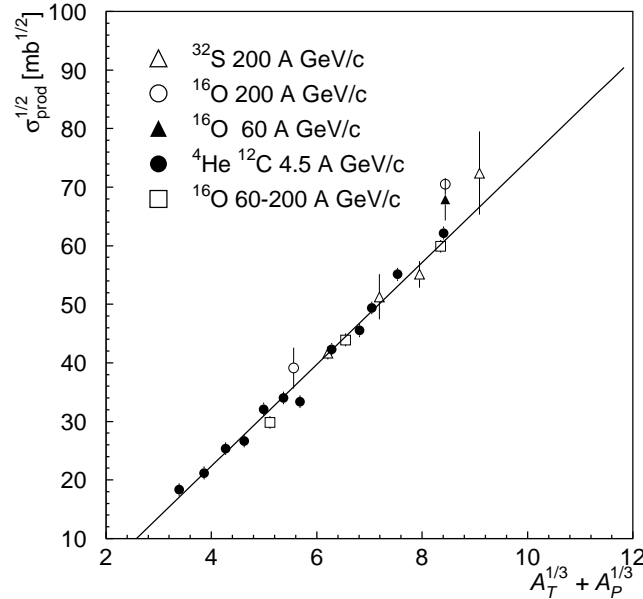


Figure 3: Root of the inelastic reaction cross section  $\sqrt{\sigma}$  as function of geometric size of interacting nuclei,  $A_P^{1/3} + A_T^{1/3}$ , for different collision partners, after Ref. [19].

The geometric approach reproduces well the value of central rapidity around which the particle spectra are centered. In the specific case of 200A GeV S–Au/W/Pb interactions one sees  $y_{\text{CM}} = 2.6 \pm 0.1$  [2]. However, the shape and the width of rapidity spectra is providing proof that much of the primary longitudinal momentum remains as collective longitudinal flow which tends to expand the source in longitudinal direction.

The central rapidity WA85 [21] transverse mass spectra  $m_{\perp}^{-3/2} dN_i/dm_{\perp}$  of diverse strange particles are shown in the Fig. 4. Similar results were also obtained by the NA35 collaboration [11, 22] and these temperatures are consistent with the results considered here. It is striking that within the observed interval  $1.5 < m_{\perp} < 2.6$  GeV the particle spectra are exponential, as required for a thermal source, irrespective of potential presence of longitudinal collision flow. Very significantly, there is clearly a common inverse slope temperature, with its inverse value around  $T = 232$  MeV.

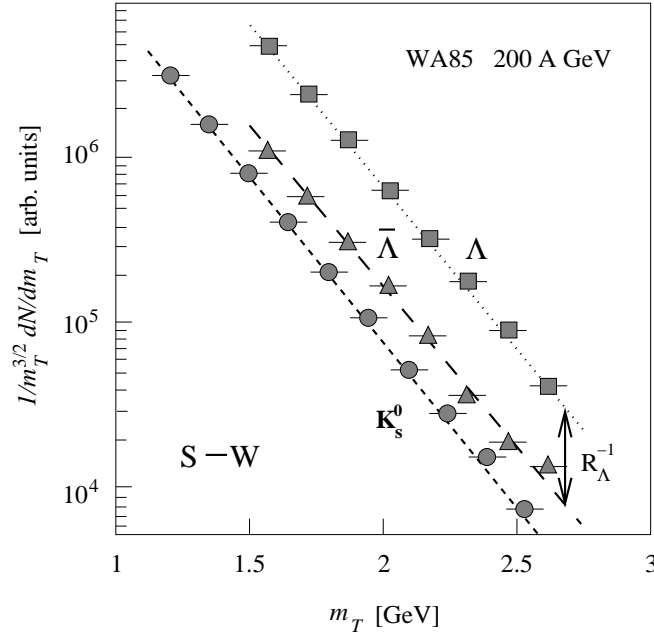


Figure 4: Strange particle spectra for  $\Lambda$ ,  $\bar{\Lambda}$ ,  $K_s^0$ . Line connecting the  $\Lambda$  and  $\bar{\Lambda}$  spectra, denoted  $R_{\Lambda}^{-1}$ , shows how the ratio  $R_{\Lambda}$  of these particle abundances can be extracted. Experimental WA85 results from reference [21].

These spectral  $m_{\perp}$  shapes lead to the suggestion that hadronic particles were produced by a thermal source with temperature  $T$  (particle spectra inverse slopes). We will discuss in more detail the many consequences of this simple remark in the following section 4. Here, we emphasize that the observed temperatures vary for different systems and energies. In collisions of S with Au nuclei at SPS, at 200A GeV, record temperatures of the magnitude of 230 MeV have been observed, which value is much greater than the temperatures  $\mathcal{O}(160$  MeV) that were noted in  $p$ - $p$  collisions [1]. The use of thermal models to describe the  $p$ - $p$  collisions has been often

critically scrutinized. However, the experimental evidence in favor of thermal source in relativistic nuclear collisions is overwhelming and the physics motivation considering the large number of participating degree of freedom considerably stronger.

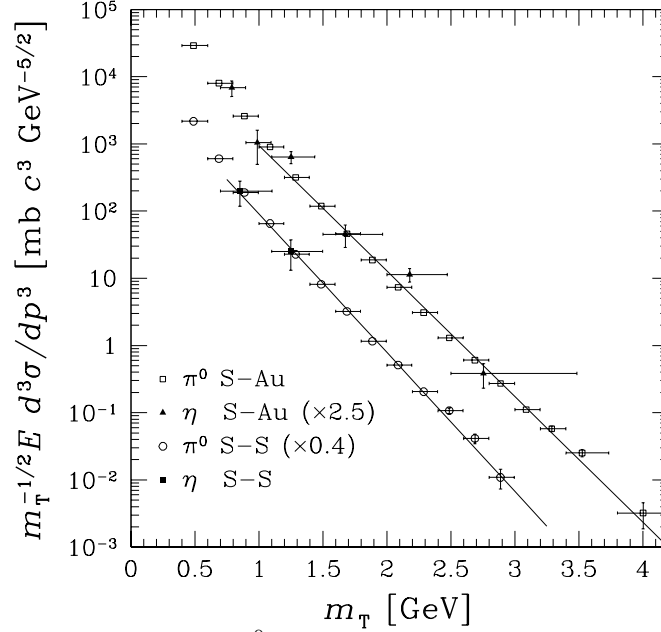


Figure 5: Neutral particle  $\pi^0$ ,  $\eta$  spectra (invariant cross sections divided by  $m_{\perp}^{1/2}$ ) in central rapidity interval  $2.1 < y < 2.9$ . Upper solid line S–Au: thermal spectrum with temperatures  $T = 232$  MeV; lower solid line S–S:  $T = 210$  MeV. Experimental data courtesy of the WA80 collaboration. [23]

It is remarkable that the same thermal behavior was seen for this  $m_{\perp}$  range by the WA80 collaboration [23] for the neutral hadrons  $\pi^0$ ,  $\eta$ . In Fig. 5 we have replotted the WA80 results multiplying the invariant cross sections by the power  $m_{\perp}^{-1/2}$ , so that there is direct correspondence between the data of experiments WA85 and WA80, both experiments focus on the central region in rapidity  $2.1 < y < 2.9$ . The upper straight line in Fig. 5 corresponds to an eye-ball thermal fit (emphasized in the WA85  $m_{\perp}$ -interval  $1.5 < m_{\perp} < 2.5$  GeV), with  $T = 232$  MeV for the S–Ag system, the lower solid line is for S–S collisions and was done with  $T = 210$  MeV. The choice of S–S temperature was based on the WA94 [24] results for spectra of strange antibaryons. Note that we separated by factor 0.4 the  $\pi^0$  S–S results from the S–Au results; and that the relative  $\eta$  to  $\pi^0$  normalization enhancement is 2.5, which factors makes the  $\eta$  abundance fall onto the  $\pi^0$  yields. It

is noteworthy that the WA80 particle spectra span 7 decades. The rise in meson yield at low  $m_{\perp}$  is due to the here unaccounted contribution of decaying resonances produced very abundantly in hot hadronic matter. Similarly, some of the concavity of the spectrum arises from non-trivial and in the current approach unaccounted flow effects.

### 2.3 Electromagnetic probes

Photons and leptons are, on first sight, the most promising probes of dense hadronic matter [4]. Electromagnetic interactions are strong enough to lead to an initial detectable signal, with secondary interactions being too weak to alter substantially the shape and yield of the primary spectra. Thus direct photons and leptons contain information about the properties of dense matter in the initial moments of the collision. Of particular interest could be the exploration of the initial time period leading to the formation of the thermal equilibrium.

In all interactions in which we can form final state photons, also dileptons can be produced in the decay of a off-mass shell photon:  $\gamma^*(M) \rightarrow l(p_l)\bar{l}(p_{\bar{l}})$ . Here, the dilepton pair produced at a given (central) rapidity  $y$  is solely characterized by its invariant mass  $M^2 = (p_l + p_{\bar{l}})^2$ . Because the dilepton formation requires one additional electromagnetic interaction, the dilepton yield is considerably smaller, by a factor 300 or more, compared to the yield of direct photons. However, the presence of numerous hadronic particles that can decay into photons and/or dileptons implies that the experimental sensitivity is also related to the strength of these backgrounds, and in this respect experience has shown that dileptons hold a small edge over direct photons.

The photon backgrounds are substantial, essentially arising from neutral meson decays.  $\pi^0$  decay in flight produces also high energy photons, and in SPS experiments even at several GeV (in the CM frame of a fireball) the backgrounds are significant, covering up within today's experimental precision in S-W/Pb all direct signals of dense matter. On the other hand, the measured high energy  $\gamma$  yield, given the multi-segmentation of the WA80/93/98  $\gamma$ -detector, allows to reconstruct the spectrum of very high energy mesons as shown above in Fig. 5, providing a rare comprehensive glimpse of the hadronic particle spectrum over many decades of yield.

It is not likely that the situation will change greatly in more energetic, thus 'hotter' interactions, unless a major change of the reaction mechanism occurs: the radiance of direct photons and the entropy content, which defines the final hadron multiplicity and thus secondary yield of photons and leptons, are both rising in a similar way with temperature. Consequently, the signal to background ratio is relatively unaffected. What can have considerable impact is the life span of the hot initial state: because we are far

from equilibrium conditions for electromagnetic probes, the direct photon yield is proportional to the life span of the hot matter fireball. Since the size of the initial system is proportional to the life span of a freely exploding fireball, considerable advantage will result when the present experiments with the relatively small system (S–Pb) are extended to the largest available Pb–Pb collisions. We expect an enhancement by factor 4 of the direct photon signal, compared to the hadron decay backgrounds. Consequently, if indeed the current experimental situation, as has been repeatedly suggested, is just at the sensitivity limit, a very strong direct photon signal of new physics should be seen in the ongoing Pb–Pb CERN experiments.

The subtle advantage of dileptons over photons arises from the possibility to consider the yield of dileptons as function of the lepton pair invariant mass  $M$ : hadronic particle decays occur within well defined regions of  $M$  and hence one can expect windows of opportunity in which the backgrounds are small. Specifically, in the rather wide interval  $m_\phi(s\bar{s}) < M < m_\Psi(c\bar{c})$  there are no hadron resonances contributing to the dilepton background. Thus in the middle of this dilepton yield dip, around  $M \simeq 2 \pm 0.6 \text{ GeV}$ , any additional radiance is more easy to note [25].

Several CERN experiments (NA34/3, NA38) have seen in S–Pb/U interactions considerable dilepton yield above background in this kinematic domain [26,27]. A typical calculation of the dimuon yields as function of the invariant mass, taken from our earlier work [25,18] is shown in Fig. 6: the solid line is the sum of the thermal QGP dimuons (short-dashed contribution), the hadron contribution (long-dashed component) and the Drell–Yan (with  $K = 2$ ) together with renormalized  $J/\psi$  contributions (dotted line, chosen to fit the  $J/\psi$  peak).

Recently, NA34/3 and NA45 have furthermore reported considerable enhancement of the dilepton yield in the low  $M \simeq 0.5 \text{ GeV}$  region [26,27,28]. Though more spectacular, the physical meaning of this result hinges on a comprehensive understanding of many possible hadron resonance process that could produce low  $M$ -dileptons, and thus is potentially primarily a probe of the confined hadronic rather than deconfined QGP phase.

All these dilepton enhancements reported do not contradict the lack of associated direct photon signatures, which turn out to be just not visible given the background levels. On the other hand, we can justly expect that if the dilepton phenomena described here are indeed related to primordial new physics effects, we should see them clearly also in photon radiance, when the new data for the much larger Pb–Pb collisions is analyzed. On the other hand, should the dilepton results not manifest themselves in the direct photon enhancement, it is likely that these originate from some not fully understood normal hadronic effect, and thus are of considerable lesser physical relevance.

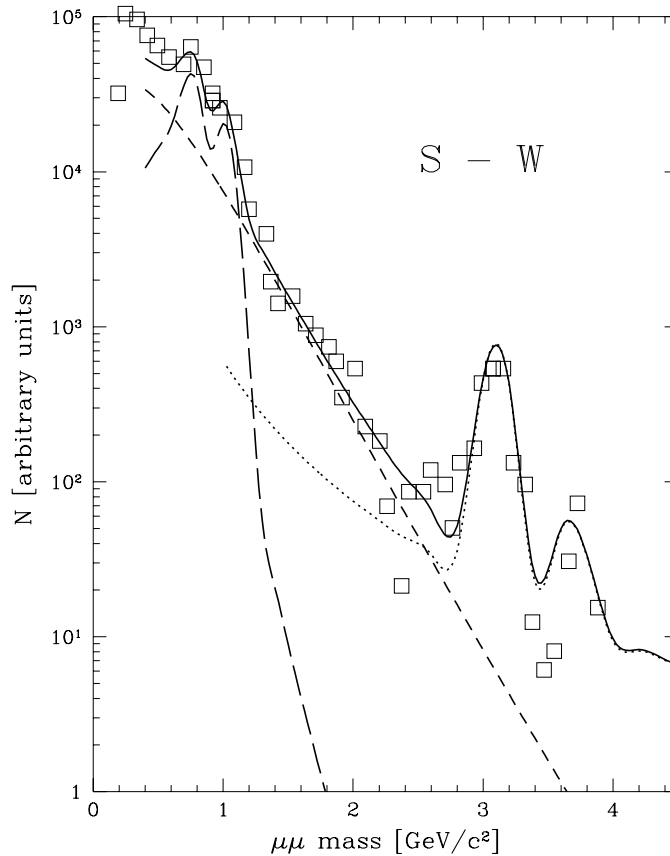


Figure 6: Spectrum of dimuons as a function of the dimuon invariant mass (arbitrary normalization), after Ref. [25,18]. The solid line is the sum of the thermal QGP dimuons (short-dashed contribution), the hadron contribution (long-dashed component) and the Drell-Yan (with  $K = 2$ ) together with normalized  $J/\psi$  contributions (dotted line, chosen to fit the  $J/\psi$  peak). Experimental results (open squares) are from NA34/3 experiment.

## 2.4 Charmonium suppression

Experimental results show the predicted [16] suppression of the Charmonium yield after its interaction with dense matter [29]. Despite early hope that the interaction of charmonium  $c\bar{c} = \Psi$  state with dense hadronic matter will be able to distinguish the difference in structure of the confined and deconfined matter, more recent and detailed theoretical studies accounting for the composite structure of charmonium [30] have revealed that the absorption/dissolution of charmonium in strongly interacting matter is similar for the different structures here considered. Consequently, the sup-

pression of charmonium production in nuclear interactions involving passage of  $\Psi$  through the dense matter, can be now accounted for both by interaction with confined and unconfined dense matter. While we therefore cannot on the basis of this effect obtain evidence for or against formation of QGP phase, the observed suppression phenomenon provides in itself a very clear confirmation of the formation of a rather small and localized, dense hadronic matter region.

## 2.5 HBT-interferometry

Pion and kaon correlation functions are measured to study the space-time evolution of the hadronic source. They are simply obtained from the ratio of the two particle cross section to the product of the two single particle cross sections, taken preferably from two different events to assure exclusion of correlation effects. The resulting correlation  $C_2$  is fitted to the convenient form valid for azimuthally symmetric sources:

$$C_2 = D \left[ 1 + \lambda e^{-(q_o^2 R_o^2 + q_s^2 R_s^2 + q_l^2 R_l^2 + 2q_l q_o R_{l_o}^2)} \right], \quad (3)$$

where ‘ $l$ ’ (longitudinal) denotes the two particle momentum projection onto the axis parallel to the beam, and ‘ $o$ ’ and ‘ $s$ ’ are the directions perpendicular to beam axis: ‘ $o$ ’ (out) is parallel and ‘ $s$ ’ (side) is orthogonal to the two particle transverse momentum sum axis. The last term in Eq. (3), which mixes the components  $q_o$  and  $q_l$  has been often neglected [31].

Compared to HBT interferometry of stars, the situation in heavy-ion collisions is complicated by the finite lifetime and the strong dynamical evolution of the particle emitting source. Thus the interpretation of the observed correlations between the produced particles is in general model-dependent, and a considerable amount of theoretical effort has been spent on the question to what extent this intrinsic model dependence can be reduced by a refined analysis [31].

The HBT type interpretation of experimental results leads to the following hypothesis regarding the particle source:

1. emission of particles is chaotic ( $\lambda \rightarrow 1$ ),
2. correlated particles do not arise primarily from resonance decays,
3. they do not interact subsequent to strong interaction freeze-out — corrections for Coulomb effects are often applied,
4. kinematic correlations, e.g., energy-momentum conservation, are of no relevance.

Considerable wealth of available experimental results [32,33] leads us to a few conclusions of relevance to the understanding of the reaction mechanisms operating in relativistic nuclear collisions.



- The nuclear collision geometry determines the source size of pions and kaons. No evidence is found for a major expansion of the hadronic fireball, required, e.g., for a (long lived) mixed (HG/QGP) intermediate phase.
- The size of the particle source is similar though a bit smaller for strange (kaons) than non-strange (pions) particles.
- There is proportionality of the central hadron multiplicity yield to the geometric volume of the source.
- Evidence is emerging for presence of transverse flow of the particle source.

These results suggest to us that after its formation the (deconfined) fireball expands and then rather suddenly disintegrates and hadronizes, freezing out final state particles at the very early stage of the evolution of strongly interacting matter.

### 3 Strangeness

#### 3.1 Properties of strange particles

We now briefly survey the key properties of strange particles and mention some prototype methods for their detection. Among strange baryons (and antibaryons) we record:

**HYPERONS**  $Y(qqs)$  and  $\bar{Y}(\bar{q}\bar{q}\bar{s})$  comprising two types of particles<sup>1</sup>, the isosinglet  $\Lambda$  and the isotriplet  $\Sigma$ . Among the hyperons we distinguish:

- The isospin singlet lambda  $\Lambda(uds)$ , a neutral particle of mass 1.116 GeV that decays weakly with proper path length  $c\tau=7.9\text{cm}$ . The dominant and commonly observed decay is

$$\Lambda \rightarrow p + \pi^- \quad 64\%,$$

the other important weak decay

$$\Lambda \rightarrow n + \pi^0 \quad 36\%,$$

has only the hard to identify neutral particles in the final state. The decay of a neutral particle into a pair of charged particles forms a characteristic ‘V’ structure shown in Fig. 7.

Aside of the ground state (positive parity, spin 1/2) we encounter a spin  $1/2^-$  resonance  $\Lambda(1.405)$  and also  $3/2^-$  state  $\Lambda(1.520)$ . These and higher

<sup>1</sup>Here and below the valence quark content is indicated in parenthesis

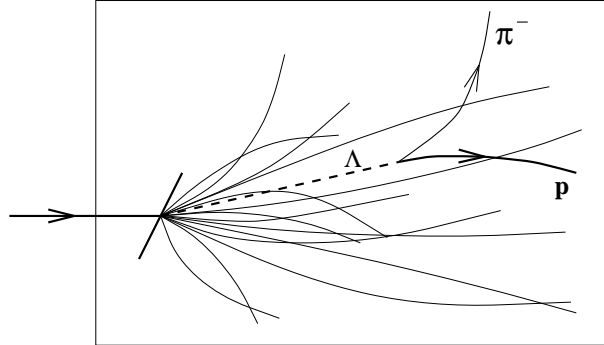
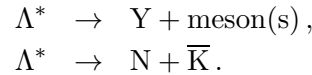


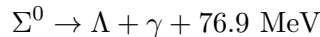
Figure 7: Schematic representation of the  $\Lambda$ -decay topological structure showing as dashed line the invisible  $\Lambda$  and the decay ‘V’ of the final state charged particles. Other directly produced charged particle tracks propagating in a magnetic field normal to the figure plane are also shown.

excited resonance states (13 are presently known with mass below 2.350 GeV) decay hadronically with the two principle channels:



Since the hadronic decays have free space proper decay paths of 1–10 fm (widths  $\Gamma = 16\text{--}250$  MeV), all these resonances contribute to the abundance of the observed ‘stable’ strange particles  $\Lambda, K$ . The practical approach to the observation of  $\Lambda$  is to observe the (dominant) decay channel with two final state charged particles pointing to a formation vertex remote from the collision vertex of projectile and target. This approach includes in certain kinematic region the events which originate from the  $K_S$  decay (see below). The well established method of data analysis has been reviewed elsewhere [36].

- The isospin triplet  $\Sigma^0, \Sigma^\pm$  of mass 1.189 GeV. The decay of neutral



occurs within  $c\tau = 2.22 \cdot 10^{-9}$  cm, thus well away from the reaction region, but for the observer in the laboratory this remains indistinguishable from the interaction vertex. Consequently all measurements of  $\Lambda$  combine the abundances of  $\Lambda$  and  $\Sigma^0$ , and all the higher resonances that decay hadronically into  $\Sigma^0$ .  $\Sigma^0$  is taken to be produced with a thermally reduced rate compared to the abundance of  $\Lambda$ :

$$N_{\Sigma^0} = \left(\frac{m_\Sigma}{m_\Lambda}\right)^a e^{-(m_\Sigma - m_\Lambda)/T} N_\Lambda. \quad (4)$$

Here the power  $a$  depends on what precisely is measured. For example when  $N$  stands for  $Ed^3N/d^3p$  we have  $a = 1$ ; when this spectral distribution is integrated over a wide region of rapidity,  $N$  stands for  $dN/dM_\perp$  and we find  $a = 3/2$  since we have  $m/T \gg 1$  ( $a = 0$  follows when  $m/T \ll 1$ ).

As with  $\Lambda$  there are several (nine) heavier  $\Sigma$  resonances known at  $m \leq 2.250$  GeV. When produced, they all decay hadronically producing  $\bar{K}, \Lambda, \Sigma$ .

Turning briefly to the charged  $\Sigma^\pm$  we note that there is only one dominant decay channel for the  $\Sigma^-$  decay:

$$\Sigma^- \rightarrow n + \pi^- \quad c\tau = 4.43 \text{ cm}.$$

Because there are two isospin allowed decay channels of similar strength for the  $\Sigma^+$ :

$$\begin{aligned} \Sigma^+ &\rightarrow p + \pi^0 & 51.6\%, \\ &\rightarrow n + \pi^+ & 48.3\%, \end{aligned}$$

the decay path here is nearly half as long,  $c\tau = 2.4$  cm.  $\Sigma^\pm$  have not yet been studied in the context of QGP studies, as they are relatively more difficult to observe compared to  $\Lambda$  — akin to the  $\Xi$  decay (see below) there is always an unobserved neutral particle in the final state, but unlike  $\Xi$  the kink that is generated by the conversion of one charged particle into another, accompanied by the emission of a neutral particle, is not associated with subsequent decay of the invisible neutral particle accompanied by a ‘V’ charged particle pair.

It is generally subsumed that abundances of all three  $\Sigma$  are equal.

#### **CASCADES** $\Xi(qss)$ and $\bar{\Xi}(\bar{q}\bar{s}\bar{s})$

The double strange cascade baryons and antibaryons  $\Xi^0(ssu)$  and  $\Xi^-(ssd)$  are below the mass threshold for hadronic decays into hyperons and kaons, also just below the weak decay threshold for  $\pi + \Sigma$  final state. Consequently we have one primary decay in each case:

$$\begin{aligned} \Xi^-(1321) &\rightarrow \Lambda + \pi^- & c\tau = 4.9 \text{ cm}, \\ \Xi^0(1315) &\rightarrow \Lambda + \pi^0 & c\tau = 8.7 \text{ cm}. \end{aligned}$$

The first of these reactions can be found in charged particle tracks since it involves conversion of the charged  $\Xi^-$  into the charged  $\pi^-$ , with the invisible  $\Lambda$  carrying the ‘kink’ momentum. For  $\Xi^-$  to be positively identified it is required that the kink combines properly with an observed ‘V’ of two charged particles which identify a  $\Lambda$  decay. This decay topology situation is illustrated in Fig. 8.

There are also several  $\Xi^*$  resonances known, which (with one exception) feed down into the hyperon and kaon abundances by weak decays. The

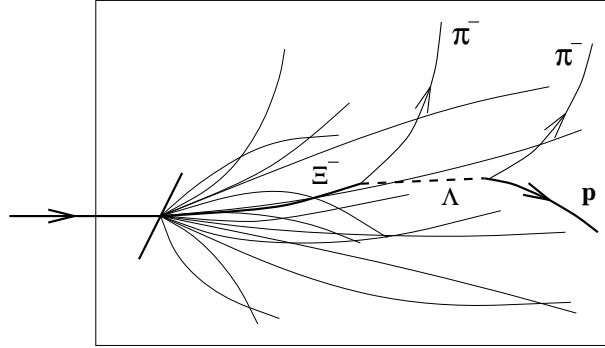
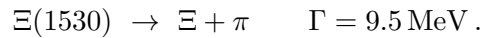


Figure 8: Schematic representation of the  $\Xi^-$ -decay topological structure showing as dashed line the invisible  $\Lambda$  emerging from the decay kink and the decay ‘V’ of the final state charged particles. Other directly produced charged particle tracks propagating in a magnetic field normal to the figure plane are also shown.

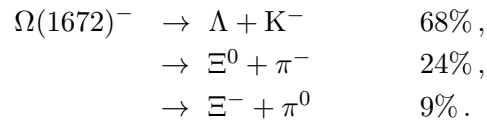
exception is the hadronic decay of the spin-3/2 recurrence of the spin-1/2 ground state:



Since the 3/2 state is populated twice as often as is the spin 1/2 ground state, the penalty due to the greater mass is almost compensated by the statistical factor, in particular should the source of these particles be at high (that is  $T > 180 \text{ MeV}$ ) temperatures.

#### OMEGAS $\Omega(sss)^-$ and $\bar{\Omega}(\bar{s}\bar{s}\bar{s})$

There are several primary weak interaction decay channels leading to the relatively short proper decay path  $c\tau = 2.46 \text{ cm}$ :



The first of these decay channels is akin to the decay of the  $\Xi^-$ , except that the pion is now a kaon. In the other two options, after cascading has finished, there is a neutral pion in the final state, which makes the detection of these channels not practical. There is only one known, rather heavy,  $\Omega^*(2250)$  resonance.

It should be remembered that the abundance of  $\Omega$  benefits from the spin-3/2 statistical factor.

**KAONS**  $K(q\bar{s}), \bar{K}(\bar{q}s)$ • **neutral kaons**  $K_S, K_L$ 

This is not the place to describe in detail the interesting physics of the short and long lived neutral kaons, except to note that both are orthogonal combinations of the two neutral states ( $d\bar{s}$ ), ( $\bar{d}s$ ). The short lived combination has a  $c\tau = 2.676$  cm and can be observed in its charged decay channel:

$$\begin{aligned} K_S &\rightarrow \pi^+ + \pi^- & 69\%, \\ &\rightarrow \pi^0 + \pi^0 & 31\%. \end{aligned}$$

Care must be exercised to separate the  $K_S$  decay from  $\Lambda$  decay, since in both cases there are two a priori not identified charged particles in the final state, making a ‘V’ originating in an invisible neutral particle.

The long lived kaon  $K_L$  with  $c\tau = 1549$  cm has not been studied in relativistic heavy ion collision experiments.

• **charged kaons**  $K^+(u\bar{s}), K^-(\bar{u}s) = \bar{K}^+$ 

Charged kaons can be observed directly since their mass differs sufficiently from the lighter  $\pi^\pm$  and the heavier proton/antiproton. However, at the SPS energies the CM-frame has rapidity 2.5–3 and thus the distinction between the different charged particles is not easy, though not impossible, such that directly measured spectra should become available in the near future.  $K^\pm(494)$  decay with  $c\tau = 371$  cm, with three dominant channels, of which the one with only charged particles in final state (smallest branching ratio) has been used in our field:

$$\begin{aligned} K^+ &\rightarrow \mu^+ + \nu_\mu & 63.5\%, \\ &\rightarrow \pi^+ + \pi^0 & 21.2\%, \\ &\rightarrow \pi^+ + \pi^+ + \pi^- & 5.6\%. \end{aligned}$$

In general it is subsumed that the mean abundance of the charged kaons is similar to the abundance of the neutral  $K_S$ .

 **$\phi$ -MESON**  $\phi(s\bar{s})$ 

The vector meson  $\phi$  with mass 1019.4 MeV has a relatively narrow full width  $\Gamma_\phi = 4.43$  MeV, since it is barely above the threshold for the decay into two kaons. Consequently, the total width and thus particle yield could be easily influenced by hadronic medium effects: these could facilitate induced decays. On the other hand the slow decays into two leptons

$$\begin{aligned} \phi &\rightarrow e^+ + e^- & 0.031\%, \\ &\rightarrow \mu^+ + \mu^- & 0.025\%, \end{aligned}$$

which have partial widths 1.37 keV and 1.1 keV allow the determination of the number of  $\phi$ -mesons that emerge from the interaction region. While absolute particle yields may be difficult to determine, one can compare the yield of  $\phi$  to the yield of  $\rho(770)$ -meson, the non-strange partner of the  $\phi$ .

### 3.2 Diagnostic signatures

Several effects combine to make strangeness a very interesting diagnostic tool of dense hadronic matter. All strange matter has to be made in inelastic reactions, while light  $u$ ,  $d$  quarks are also brought into the reaction by the colliding nuclei. The strange quarks  $s$  are found abundantly in relativistic nuclear collisions [34], at 200A GeV much more so than it could be expected based on simple scaling of  $p$ - $p$  reactions [11, 37], while this enhancement is not reported in  $p$ -A collisions [38]. Because there are many different strange particles, we have a very rich field of observables with which it is possible to explore diverse properties of the source. This is a trivial but indeed the most important reason why ‘Strangeness’ is such a very informative observable of dense hadronic matter. Strange antibaryons were from the beginning recognized as being very important in the study of the dense hadronic matter. The high strange particle density in the QGP led to the prediction [6] of highly amplified abundance of multistrange antibaryons. Considering that these particles are rarely produced in conventional collisions, while they can be easily formed in a primordial dense soup containing many  $\bar{s}$  quarks, one is easily led to suggest that their abundance is a significant signature of deconfinement. Because of the experimental complexity related to detection of strange particles, only recently, results experiments became available, allowing a thorough test of the theoretical ideas. These results obtained at CERN with 200A GeV projectiles [21, 11, 39, 40] support the contention that strange antibaryons are found in greatly anomalous abundance. It remains to be seen if the systematic behavior as function of, e.g., collision energy will confirm QGP-fireballs as the source of strange antibaryons. But it can be safely concluded today that strangeness has fulfilled the high expectations about being a useful signature of the nature of the dense hadronic phase.

Generally, not only (relative) abundances but also the spectra of several strange particles  $K^\pm$ ,  $K_S$ ,  $\phi$ ,  $\bar{p}$ ,  $\Lambda$ ,  $\bar{\Lambda}$ ,  $\Xi^-$ ,  $\bar{\Xi}^-$ ,  $\Omega$ ,  $\bar{\Omega}$  are studied as function of rapidity and transverse mass. We have included in above list the closely related antiprotons  $\bar{p}$ , which are also fully made in the collision. The classic observables based on these particles are their abundance ratios: leaving out an overall normalization factor associated with the reaction volume, and recalling that there are relations between the abundances such as of kaons ( $K^+ + K^- \simeq 2K_S$ ) we have 9 independent normalization parameters describing the yields of  $K^\pm$ ,  $K_S$ ,  $\phi$ ,  $\bar{p}$ ,  $\Lambda$ ,  $\bar{\Lambda}$ ,  $\Xi^-$ ,  $\bar{\Xi}^-$ ,  $\Omega$ ,  $\bar{\Omega}$ . These can

be redundantly measured with the help of the  $36 = 9 \cdot 8/2$  independent particle yield ratios. Aside of the yield normalization parameters, there are in principle 11 different spectral shapes which we presume to be closely related to each other and to be governed by the same inverse slope parameter (temperature) parameter. The experimental fact that once effects related to particle decays and matter expansion (transverse flow) are accounted for, the  $m_{\perp}$  spectra of all these particles are characterized by a common temperature, cannot be taken lightly and suggest strongly some deeper connection between all these particles that arise from quite different individual formation processes in the confined phase. Our point of view is that the source of all strange particles is a thermalized fireball permitting a common mechanism to govern the production of the very different strange particles, as well as  $\bar{p}$ . We will develop in full below, in our theoretical approach this picture of strange particle production. We will presume that the strong interactions allow to achieve local thermally equilibrated fireball, a fact which is very much in experimental evidence, but which is far from being understood, as we stressed above. Our analysis based on the results obtained at 200A GeV favors a picture of the reaction in which the hadronization occurs rapidly such that the observed strange particles can have properties representative of the expected properties of the primordial phase.

Several global properties of the final state strange particle abundance carry such information. Consider that, when finite baryon density is present, which breaks the particle/antiparticle symmetry, the exact balance between  $s$  and  $\bar{s}$  quarks requires non-trivial relations between the parameters characterizing the final state hadron abundances. These strangeness conservation constraints imply different particle distributions for different structures of the source. It turns out that in the statistical approach the key parameter is the strange quark chemical potential  $\mu_s$ :

1. In a deconfined state in which quark bonds are broken, the strangeness neutrality implies  $\mu_s = 0$ , independent of prevailing temperature and baryon density.
2. In any state consisting of locally confined hadronic clusters,  $\mu_s$ , for finite baryon density, is generally different from zero, in order to compensate the asymmetry introduced by the finite baryon content.

The vanishing strange quark potential  $\mu_s \simeq 0$  is a striking result of different analysis of the today available data of the CERN experiments WA85 and NA35 [41, 17, 42, 8]. This important conclusion arises from study of particle abundance ratios, which act as remote thermo- and chemico-meters of the particle source. Aside of the strange quark chemical potential, one also is able to derive the light ( $u, d$ ) quark chemical potentials from strange baryon abundances.

Other generic observables that determine abundance of the final state strange particles and thus can be derived from the particle abundances are:

- Specific (with respect to baryon number  $B$ ) strangeness yield  $\langle \bar{s} \rangle / B$   
Once produced strangeness escapes, bound in diverse hadrons, from the evolving fireball and hence the total abundance observed is characteristic for the initial extreme conditions reached in the collision. Theoretical calculations suggest that glue–glue collisions in the QGP phase provide a sufficiently fast mechanism and thus an explanation for strangeness enhancement comprised in this observable.
- Phase space occupancy  $\gamma_s(t_f)$ .  
Strangeness freeze-out conditions at particle hadronization time  $t = t_f$ , given the initially produced abundance, determine the final state observable phase space occupancy of strangeness  $\gamma_s(t = t_f)$ .

### 3.3 Highlights of strangeness experimental results

We now briefly describe the key experimental results on which our here presented theoretical developments are based either in detail or/and conceptual design:

#### • Centrality of strangeness production

We consider a measure of the abundance of  $\langle s + \bar{s} \rangle$  in Fig. 9. We show here the integrated transverse mass  $m_\perp = \sqrt{m^2 + p_\perp^2}$  distribution for  $1.6\Lambda + 4K_S + 1.6\bar{\Lambda}$  as determined by the experiment NA35 [43], as function of rapidity. For the case of S–S the open circles are the measured data points, the open triangles are the symmetrically reflected data points, and squares are the results of N–N (isospin symmetric nucleon–nucleon) collisions scaled up by pion multiplicity; the difference, most pronounced at central rapidity  $y \simeq 3$  shows a new source of strangeness in the collision, and the important lesson to be drawn from this result is that strangeness enhancement originates in the central rapidity region. We also show in Fig. 9 similar results for S–Ag collisions: here the open circles are the measured points, open triangles are estimates based on S–S and the ‘reflected’ S–Ag results, and the open squares are pion multiplicity scaled p–S results.

#### • Anomalies of strange antibaryon abundances

The WA85 collaboration has extensively studied in the central rapidity region the relative abundance of the different strange baryons and antibaryons. The particle spectra ratios have been obtained at  $p_\perp \geq 1$  GeV. The results for relative abundances can be presented both for the sum of abundance with  $p_\perp \geq 1$  GeV or using as cut a fixed value  $m_\perp \geq 1.7$  GeV. In the thermal model this latter set of values is of primary interest. However,



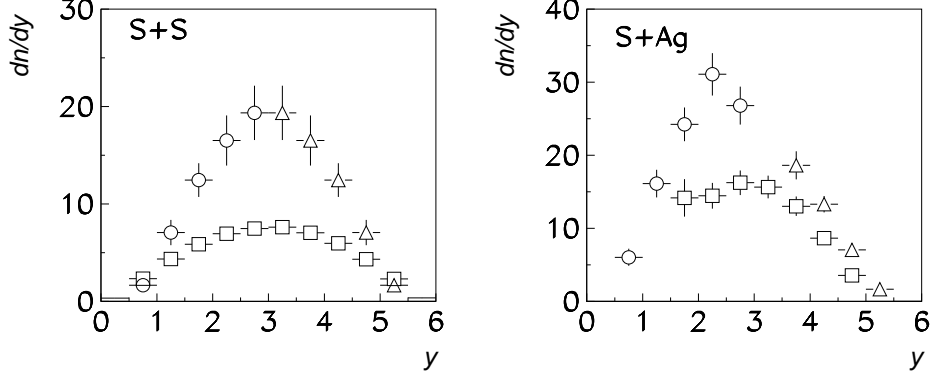


Figure 9: Abundance of  $1.6\Lambda + 4K_S + 1.6\bar{\Lambda}$  as function of rapidity. On the left S-S, on the right S-Ag (open circles are the directly measured data). The triangles are reflected data points for S-S and reflected-interpolated data employing S-S and S-Ag. The squares in S-S case are the results for N-N collisions scaled up by the pion multiplicity ratio, for S-Ag these are the scaled up p-S results. Courtesy of NA35 collaboration [43].

given prior studies of relative particle abundances one often identifies the anomalies using the fixed  $p_{\perp}$  approach. Moreover such ratios correspond more closely to the total particle abundance ratio, as we shall see in section 8.3. The experiment WA85 [44] has reported the following ratios between same baryons and antibaryons:

$$\begin{aligned} R_{\Lambda} &= 0.20 \pm 0.01 \\ R_{\Xi} &= 0.41 \pm 0.05 \end{aligned} \quad \text{for } y \in (2.3, 2.8) \text{ and } m_{\perp} > 1.9 \text{ GeV.} \quad (5)$$

have been analyzed carefully in our recent work [41, 17], and the chemical properties of the source were derived.

Strangeness abundance (phase space occupancy) at moment of particle emission is probed when ratio of particles is considered that contains a different number of strange quarks. In Fig. 10 such a World sample of strange baryon and antibaryon data is presented. We note the strong enhancement of the ratios seen in heavy ion reactions (S-S/W at 200A GeV). In the kinematic domain of Eqs. (5) the experimental results reported by the WA85 collaboration are:

$$\frac{\bar{\Xi}^-}{\Lambda + \Sigma^0} = 0.4 \pm 0.04, \quad \frac{\Xi^-}{\Lambda + \Sigma^0} = 0.19 \pm 0.01. \quad (6)$$

If the mass difference between  $\Lambda$  and  $\Sigma^0$  is neglected, this implies that an

equal number of  $\Lambda$ 's and  $\Sigma^0$ 's are produced, such that

$$\frac{\overline{\Xi}^-}{\overline{\Lambda}} = 0.8 \pm 0.08, \quad \frac{\Xi^-}{\Lambda} = 0.38 \pm 0.02. \quad (7)$$

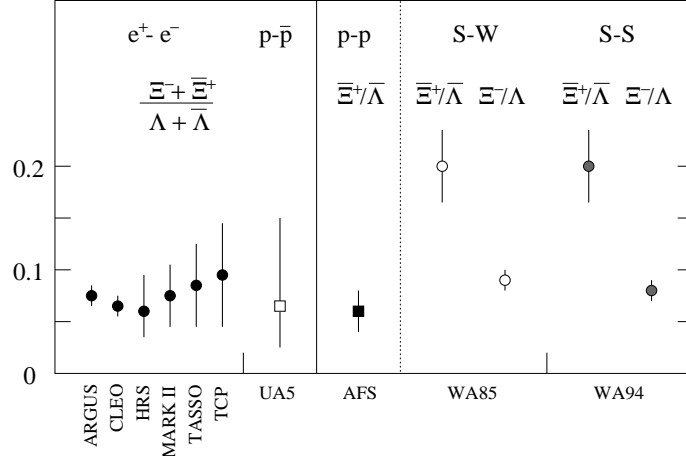


Figure 10: Ratio (at fixed  $p_{\perp}$ ) of (multi)strange baryon-antibaryon particle abundance, measured in the central rapidity region at 200A GeV S-S/W collisions, compared to ratios obtained in lepton and nucleon induced reactions. Data assembled by the WA85/94 collaboration [44].

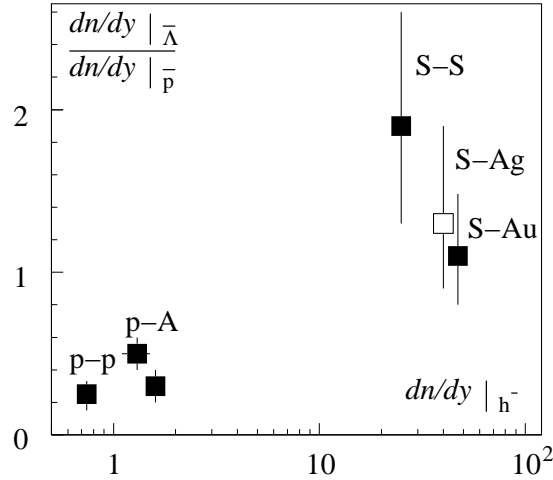


Figure 11: Ratio of the rapidity density  $dn/dy$  for  $\overline{\Lambda}/\overline{p}$ , measured at central  $y$ , as function of the negative hadron central rapidity density  $dn/dy|_{h^-}$ . Courtesy of NA35 collaboration [40].

The fact that the more massive and stranger anticascade practically equals at fixed  $m_{\perp}$  the abundance of the antilambda is most striking. These results are inexplicable in terms of hadron-cascade models for the heavy-ion collision [45]. The relative yield of  $\bar{\Xi}^{-}$  is 3.5 times greater than seen in the  $p$ - $p$  ISR experiment [46] and all other values reported in the literature, which amounts to a 4 s.d. effect [44].

Another most remarkable result related to these findings is due to the NA35 collaboration [40]: in Fig. 11 we show the ratio of the rapidity density  $dn/dy$  at central  $y$  of  $\bar{\Lambda}/\bar{p}$ , as function of the negative hadron central rapidity density  $dn/dy|_{h^{-}}$ . The  $p$ - $p$  and  $p$ -A reactions are at small values of  $dn/dy|_{h^{-}}$ , while the S-S, S-Ag, S-Au reactions are accompanied by a relatively high  $dn/dy|_{h^{-}}$ . We observe that there is an increase in this ratio by nearly factor 5, and even more significantly, the abundance of the heavier and strange  $\bar{\Lambda}$  is similar if not greater than the abundance of  $\bar{p}$ .

#### • Collectivity of strange particle production

The WA85 collaboration [44] has shown that there is a trend in these anomalous strange baryon abundances in that the yields in nuclear collision S-W (normalized by  $h^{-}$  abundance) when compared to the  $p$ -W collisions are increasing with the strangeness content, as illustrated in Fig. 12. This indicates that strange particles are formed in some collective mechanism, which favors the assembly of multiply strange hadrons. Comparable result

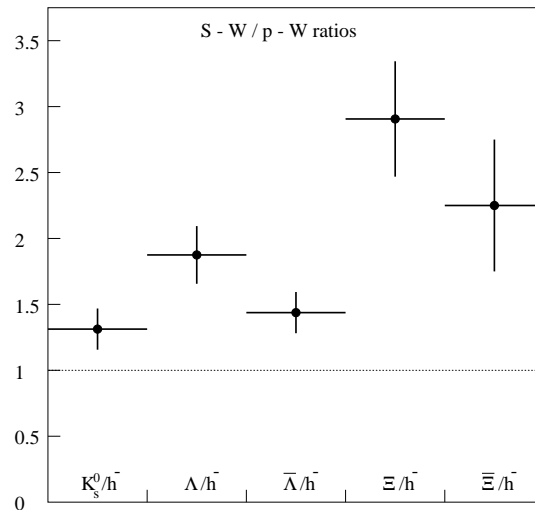


Figure 12: Ratio of  $h^{-}$  normalized particle abundances: S-W results divided by  $p$ -W results at 200A GeV in the same rapidity window near  $2.5 < y < 3$ . Dotted line: expected yields. Courtesy of WA85 collaboration [44].

is reported by the NA38 collaboration [47] which has shown that the ratio

$$\frac{\phi}{\rho + \omega} \propto \frac{s\bar{s}}{q\bar{q}},$$

rises by nearly a factor three in S–U compared to p–W reactions, in collisions with greatest particle density.

• **Thermal nature of (strange) particle spectra**

We have discussed these remarkable results above and refer here in particular to Fig. 4 and the accompanying discussion for further details.

## 4 Thermal fireball

### 4.1 Comparison to kinetic theory approach

The special virtue of the thermal fireball framework is that the spectra and particle abundances can be described in terms of a few parameters which have very intuitive meaning. In this the thermal model analysis of the experimental results differs fundamentally from other efforts made with individual particle cascade type models. These contain as inputs detailed data and their extrapolations, and often also assumptions about unknown reaction cross sections. The attainment of thermal equilibrium is in these calculations result of many individual particle-particle collisions. However, for the nucleon-nucleon (N–N) collisions we already know that the appearance of the thermal particle distributions in the final state is inexplicable in terms of dynamical microscopic models [14]. Consequently, there is no reason to expect that some microscopic dynamical approach invoking multiple series of N–N type interactions lead to any better understanding of the thermalization process. Moreover, if the underlying and yet not understood thermalization processes are, as is likely in view of the N–N situation, much faster than those operating in the numerical cascade codes, these results would not be adequate.

Such an uncertainty about the microscopic mechanisms does not beset the thermal approach, where we do not implement microscopic approach to thermalization, but rather analyze the data assuming that, though not understood, thermalization is the fastest, nearly instantaneous, hadronic process. The prize one pays in this approach is that under certain conditions one loses the ability to describe some details of the collision evolution. For example, we have not been able to identify within a thermal model a method to determine the stopping fractions (i.e., energy or baryon number deposition rate) governing the different collisions and we extract this parameter in qualitative form from the data. In the microscopic kinetic theory models one can in principle claim to ‘derive’, e.g., the energy-momentum

stopping. This current deficiency of the thermal model disappears under conditions which could lead to full stopping. In the near future we will see up to which energy this may occur for the Pb–Pb reactions. The initially studied maximum energy is 158A GeV and we hope that in a very near future the energy range between 40A and 158A GeV can be explored.

It should be noted here that in a rough survey of the particle yields one ought to observe the considerable impact of the surface of the colliding nuclei, always present in symmetric systems. Consequently, it is no surprise that many observed particle rapidity yields are wider than expected even in presence of full stopping — the degree of stopping reached can be more effectively explored considering the rapidity shapes of particles which cannot be easily made in single hadron interactions (e.g.,  $\bar{\Lambda}$ ).

## 4.2 Thermal parameters

We now discuss in qualitative terms the global parameters of the thermal fireball model. We suppose that the primordial source is a space-time localized region of thermal hadronic matter which is the source of all particle Boltzmann type spectra. At relatively high  $m_{\perp}$  the exponential spectral shape is relatively little deformed by resonance decay and the fireball dynamics, here in particular flow phenomena. Thus this portion of the spectrum should be similar for different particles, which would allow a reduction of all data to just one basic spectral shape form:

$$\frac{dN}{d^3p} = N_i e^{-E^{(i)}/T} = N_i e^{-\cosh(y-y_{\text{CM}}) m_{\perp}^i / T} . \quad (8)$$

The parameters of each particle distribution include the inverse slope  $T$  (‘temperature’) of the  $m_{\perp}$  distribution, centered around the  $y_{\text{CM}}$ .

The fireball is created in central symmetric collisions at the CM-rapidity of the N–N system, which is for relativistic systems just is 1/2 of the projectile rapidity. For asymmetric collisions such as S–Au/W/Pb the CM rapidity depends on the ratio of the participating masses  $A_{\text{P}}$ ,  $A_{\text{T}}$  of the projectile and, respectively, target nuclei, see Eq. (2).

The relative abundance of particles emerging from the thermal fireball is controlled the chemical (particle abundance) parameters, the particle fugacities [17], which allow to conserve flavor quantum numbers. Three fugacities are introduced since the flavors  $u$ ,  $d$ ,  $s$  and as appropriate  $c$  are separately conserved on the time scale of hadronic collisions and can only be produced or annihilated in particle-antiparticle pair production processes<sup>2</sup>. The fugacity of each hadronic particle species is the product of the valence

---

<sup>2</sup>We will in general not introduce and/or discuss the fugacities for quarks heavier than  $s$ . While we explore in qualitative terms the charm production, it remains a rather small effect even at LHC energies.

quark fugacities, thus, for example, the hyperons have the fugacity  $\lambda_Y = \lambda_u \lambda_d \lambda_s$ . Fugacities are related to the chemical potentials  $\mu_i$  by:

$$\lambda_i = e^{\mu_i/T}, \quad \lambda_{\bar{i}} = \lambda_i^{-1} \quad i = u, d, s. \quad (9)$$

Therefore, the chemical potentials for particles and antiparticles are opposite to each other, provided that there is complete chemical equilibrium, and if not, that the deviation from the full phase space occupancy is accounted for by introducing a non-equilibrium chemical parameter  $\gamma$  (see below).

In many applications it is sufficient to combine the light quarks into one fugacity

$$\lambda_q^2 \equiv \lambda_d \lambda_u, \quad \mu_q = (\mu_u + \mu_d)/2. \quad (10)$$

The slight isospin asymmetry in the number of  $u$  and  $d$  quarks is described by the small quantity

$$\delta\mu = \mu_d - \mu_u, \quad (11)$$

which may be estimated by theoretical considerations: we introduce the light flavor imbalance in the fireball:

$$\delta q = \frac{\langle d - \bar{d} \rangle - \langle u - \bar{u} \rangle}{\langle d - \bar{d} \rangle + \langle u - \bar{u} \rangle}. \quad (12)$$

In a central S–W collisions, considering a tube with the transverse area of the S projectile swept out from the W target, and in Pb–Pb collisions one has

$$\delta q^{\text{S–W}} \simeq 0.08 \quad \delta q^{\text{Pb–Pb}} = 0.15.$$

The value of  $\delta\mu$  is at each fixed  $T$  determined by the value of  $\delta q$ , but depends on the assumed structure of the source such as the HG and the QGP. For the QGP [41], the ratio  $\delta\mu/\mu_q$  is independent of  $\lambda_s$ , due to the decoupling of the strange and non-strange chemical potentials in the partition function. For  $\mu_q < \pi T$  we find the simple relation:

$$\delta q^{\text{QGP}} \simeq 2 \frac{\mu_d - \mu_u}{\mu_d + \mu_u} = \frac{\delta\mu}{\mu_q}. \quad (13)$$

The relation between  $\delta q^{\text{HG}}$  and  $\delta\mu$  was obtained numerically computing the partition function with all mesons and baryons up to 2 GeV mass [17]. In a large region of interest to us here ( $T \sim 150\text{--}200$  MeV) it was found that  $\delta q^{\text{HG}} \simeq \delta q^{\text{QGP}}$ . Thus irrespective of the state of the source:

$$\frac{\delta\mu}{\mu_q} = \delta q \quad \simeq 0.08 \text{ for S–W} \quad \simeq 0.15 \text{ for Pb–PB}. \quad (14)$$

Since a wealth of experimental data can be described with just a few model parameters, this leaves within the thermal model a considerable predictive power and a strong check of the internal consistency of the thermal approach we develop. Specifically, in the directly hadronizing off-equilibrium QGP-fireball considered here there are 5 particle multiplicity parameters (aside of  $T$  and  $y_{\text{CM}}$ ) characterizing all particle spectra: the fireball size  $V$ , two fugacities  $\lambda_q, \lambda_s$ , of which the latter one is not really a parameter in our approach, as we will set  $\lambda_s = 1$  because of strangeness conservation in the QGP phase, and two particle abundance non-equilibrium parameters we will discuss at length below in section 8: the strangeness occupancy factor we call  $\gamma_s$  and the ratio  $R_C^s$ , see Eq. (102), of meson to baryon abundances normalized to hadronic gas equilibrium. Only the last of these parameters is related to the mechanism governing the final state hadronization process, the others will be determined using a dynamical picture of the collision, in which the input is derived from more general qualitative conditions of the colliding system, such as the energy content or stopping power. Thus the validity of thermal and (approach to) chemical equilibrium can be conclusively tested, comparing the observed particle spectra and yields with the theoretical predictions. We can do this without the need and in particular, without the capability to modify and adapt the theoretical description to each new experimental result. Therefore, the thermal hypothesis can be relatively easily falsified, but so far this has not been the case.

### 4.3 Stages of fireball evolution

We now look at the different stages of the temporal evolution [18] and the related parameters of the fireball. The scenario we adopt is in view of the current understanding of hadronic physics the most natural one in qualitative terms, in accord with the general properties of the strong interactions and hadronic structure widely known and accepted today and it is in quantitative agreement with experimental results obtained in relativistic nuclear collisions, see section 2.

When studying collisions up to maximum available SPS energies we suppose that the relevant time development stages of the relativistic nuclear collision comprise:

1. The pre-thermal stage lasting perhaps 0.2–0.4 fm/c, during which the thermalization of the initial quark-gluon distributions occur. During this time most of the entropy obtained in the collision must be created by mechanisms that are not yet understood — this is also alluded to as the period of de-coherence of the quantum collision system. Our lack of understanding of this stage will not impact our results, as the reason that we lack in understanding is that the hadronic interactions erase the memory of this primordial stage, except for the entropy

content.

2. The subsequent inter-penetration of the projectile and the target lasting about  $\sim 1.5$  fm/ $c$ , probably also corresponding to the time required to reach chemical equilibrium of gluons  $g$  and light non-strange quarks  $q = u, d$ .
3. A third time period ( $\simeq 5$  fm/ $c$ ) during which the production and chemical equilibration of strange quarks takes place. During this stage many of the physical observables studied here will be initiated.
4. Hadronization of the deconfined state ensues: it is believed that the fireball expands at constant specific entropy per baryon, and that during this evolution or at its end it decomposes into the final state hadrons, under certain conditions in an (explosive) process that does not allow for re-equilibration of the final state particles.

In the sudden hadronization picture of the QGP fireball suggested by certain features seen in the analysis of the strange antibaryon abundances for the 200A GeV nuclear collision data [17, 41], the hadronic observables we study are not overly sensitive to the details of stage 4. Akin to the processes of direct emission, in which strange particles are made in recombination-fragmentation processes [48, 49], the chemical conditions prevailing in the deconfined phase are determining many relative final particle yields. Recent theoretical models show that such a sudden hadronization may occur [50]. Furthermore if the hadronization occurs as suggested by recent lattice results [3] at a relatively low temperature (e.g., 150 MeV), the total meson abundance which is determined by the entropy contents of the fireball at freeze-out of the particles, is found about 100% above the hadronic gas equilibrium expectations [13]. This is consistent with the source of these particles being the QGP [17, 13]. The freeze-out entropy originates at early time in collision since aside of strangeness production which is responsible for about 10% additional entropy there is no significant entropy production after the initial state has occurred [13].

The above remarks apply directly to the 200A GeV data. The general features of particle multiplicities obtained at 15A GeV are consistent with the thermal equilibrium hadronic gas state expectations [51, 52]. However, the source of these particles could also be a QGP fireball, provided that a slow re-equilibration transition occurs under these conditions, leading to the equilibrium state among many final hadron gas particles.

The temperature of the fireball evolves in time and within our schematic model we introduce here a few characteristic values which have both intuitive meaning and are useful in future considerations. We characterize the above described stages by the following temperatures:



$T_{\text{th}}$	temperature associated with the initial thermal equilibrium, ↓ <i>production of <math>q, \bar{q}, G</math>;</i>
$T_{\text{ch}}$	chemical equilibrium for non-strange quarks and gluons, ↓ <i>production of <math>s, \bar{s}</math> quarks and fireball expansion;</i>
$T_0$	condition of maximal chemical equilibrium: ‘visible’ temperature, ↓ <i>fireball expansion/particle radiation;</i>
$T_{\text{f},s}$	temperature at freeze-out for non-strange or strange particles.

We encounter a considerable drop in temperature and obviously  $T_{\text{th}} > T_{\text{ch}} > T_{\text{f}}$ . However, the entropy content which determines the final particle multiplicities evolves more steadily, indeed it remains nearly constant: aside of the initial state entropy formation, in our model additional entropy increase is due to the formation of the strangeness flavor. Thus strangeness formation processes are acting like a viscosity slowing down the transverse flow of hadronic matter.

Initially, temperature decreases rapidly from  $T_{\text{th}}$  to  $T_{\text{ch}}$  since there is rapid quark and gluon production which establishes the chemical equilibrium, as we have shown [53] these processes generate little entropy. We will explicitly compute the values of  $T_{\text{ch}}$  for different systems balancing the energy per baryon and the collision pressure.

If the final state particles emerge directly, without re-equilibration, from the fireball [41, 48], this observed temperature  $T_{\perp}$  in the particle spectra would be closely related to the full chemical equilibration temperature  $T_0$  :

In the transverse mass spectra of strange (anti)baryons an inverse temperature slope  $T_{\perp}$  ( $= 232 \pm 5$  MeV in S–A collisions at 200A GeV) is found, and the important matter is to relate this observed value to the initial  $T_{\text{ch}}$  condition of the fireball. It is to this end that we have introduced above the quantity  $T_0$  which arises from  $T_{\text{ch}}$  when we relax strangeness to (nearly) full chemical equilibrium, keeping the entropy content of gluons and light flavor unchanged.  $T_0$  is always somewhat smaller than  $T_{\text{ch}}$  since energy has been spend to produce strangeness [18]. Even more energy is spend into the transverse expansion and thus the temperature at freeze out is nearly certainly considerably lower than  $T_0$ . When the final state particles emerge from the flowing surface, they are blue-shifted by the flow velocity. This Doppler shift effect restores the high apparent  $T_{\perp}$  in high  $m_{\perp}$  particle spectra [54]:

$$T_{\perp} \simeq \sqrt{\frac{1+v_{\text{f}}}{1-v_{\text{f}}}} T_{\text{f}}, \quad (15)$$

and  $T_{\perp}$  is found in model calculations to be close if not exactly equal to the value  $T_0$  that would be present in the chemically equilibrated fireball, provided that no reheating has occurred in a strong phase transition of first order. Despite our still considerable ignorance of the dynamics of

fireball and particle freeze-out mechanisms and conditions, we believe that the uncertainty in the value of the temperature  $T_0$  as derived from the value of  $T_\perp$  is not large. Namely, if QGP phase is directly dissociating by particle emission, this is trivially so, since we see what happened in a direct observation. If, as is generally assumed, there were to be substantial flow, one can assume some temperature  $T_0$ , and given equations of state (EoS), obtain the hydrodynamic radial expansion [25]; especially at the high  $m_\perp \simeq 2$  GeV the resulting inverse slope temperature  $T_\perp$  of the particle is found smaller but almost equal to  $T_0$ .

#### 4.4 Analysis of properties of the strange particle source

In the thermal fireball model with sudden non-equilibrium hadron formation, the observed particle yields can be relatively easily related to the physical properties of the fireball.

The abundance of particles emerging is, according to Eq. (8), determined by the normalization constant:

$$N_j = C_{j=M,B} V \prod_i n_i, \quad n_i = g_i \lambda_i \gamma_i, \quad (16)$$

where it is assumed that the final state particle of type  $j$  contains the quark valence components of type  $i$  and these are counted using their statistical degeneracy  $g_i$ , fugacity  $\lambda_i = \exp(\mu_i/T)$  and the chemical equilibration factor  $\gamma_i$ .  $V$  is the emission source volume. Particle fragmentation has been found to change the recombination results in a minor way [48], because the fragmentation enhances the number of all quarks, and thus contributes in a similar way to all flavors, and further, since in the ratio of particle abundances a partial cancelation of fragmentation effect occurs. Moreover, fragmentation, by its intrinsic nature primarily increase the yield of particles at small  $m_\perp$ .

Once chemical non-equilibrium features are accounted for by three significant chemical non-equilibrium abundance factors  $\gamma_s(t_f)$ , the strangeness phase space occupancy, and  $C_{M,B}$ , meson and baryon particle yield compared to chemical equilibrium yield in hadronic gas, see section 8, the chemical potentials for particles and antiparticles are opposite to each other and the particle and antiparticle abundances are related, see Eq. (9). As indicated in Eq. (16), the fugacity of each final state hadronic species is the product of the valence quark fugacities.

Thus the ratios of strange antibaryons to strange baryons *of same particle type*:

$$R_\Lambda = \bar{\Lambda}/\Lambda, \quad R_\Xi = \bar{\Xi}/\Xi \quad \text{and} \quad R_\Omega = \bar{\Omega}/\Omega,$$

are in our approach simple functions of the quark fugacities. For the avail-

able two ratios in experiment WA85 one has specifically

$$R_{\Xi} = \frac{\overline{\Xi}^-}{\Xi^-} = \frac{\lambda_d^{-1} \lambda_s^{-2}}{\lambda_d \lambda_s^2}, \quad R_{\Lambda} = \frac{\overline{\Lambda}}{\Lambda} = \frac{\lambda_d^{-1} \lambda_u^{-1} \lambda_s^{-1}}{\lambda_d \lambda_u \lambda_s}. \quad (17)$$

These ratios can easily be related to each other, in a way which shows explicitly the respective isospin asymmetry factors and strangeness fugacity dependence. Eq. (17) implies:

$$R_{\Lambda} R_{\Xi}^{-2} = e^{6\mu_s/T} \cdot e^{2\delta\mu/T}, \quad R_{\Xi} R_{\Lambda}^{-2} = e^{6\mu_q/T} \cdot e^{-\delta\mu/T}. \quad (18)$$

Eq. (18) is generally valid, irrespective of the state of the system (HG or QGP), as long as the momentum spectra of the radiated particles are “thermal” with a common temperature (inverse slope). We see that once the left hand side is known experimentally, it determines rather accurately the values of  $\mu_q, \mu_s$  which enter on the right hand side with a dominating factor 6, while the (small) flavor asymmetry  $\delta\mu$ , Eq. (11), plays only a minor, but significant role, given the precision of the experimental results [17]. This explains how, by applying these identities to the early WA85 data [44], it has been possible [41] to determine the chemical potentials with considerable precision in spite of the still relatively large experimental errors on the measured values of  $R_{\Lambda}, R_{\Xi}$ .

We obtain the following values of the chemical potentials for S–W central collisions at 200A GeV:

$$\frac{\mu_q}{T} = \frac{\ln R_{\Xi}/R_{\Lambda}^2}{5.94} = 0.39 \pm 0.04, \quad \lambda_q = 1.48 \pm 0.06 \quad (19)$$

$$\frac{\delta\mu}{T} = \frac{\mu_q}{T} \delta q = 0.031 \pm 0.003, \quad (20)$$

$$\frac{\mu_s}{T} = \frac{\ln R_{\Lambda}/R_{\Xi}^2 - 0.062}{6} = 0.02 \pm 0.05. \quad (21)$$

Where  $\delta q$ , see Eq. (14) is valence quark flavor asymmetry. In our dynamical description of the collision [18], see section 5, we have been able to determine the value  $\lambda_q$  reached in the collision. Naturally, as long as a QGP fireball is rapidly hadronizing, we have  $\mu_s \simeq 0$  that is  $\lambda_s \simeq 1$ . We find in section 8.3 below substantial variation of  $\lambda_q$  with fireball energy content. Therefore the agreement of our here presented analysis with these theoretical results can not be seen as being accidental.

We now show how in the thermal model the ratios between antibaryons with different strange quark content are dependent on the degree of the strangeness saturation. Now it is important to remember that our evaluation of the ratios is at fixed  $m_{\perp}$ . Up to cascading corrections a complete cancelation of the fugacity and Boltzmann factors occurs when we form

the product of the abundances of baryons and antibaryons, comparing this product for two different particle kinds [41], e.g.:

$$\left. \frac{\Xi^-}{\Lambda} \cdot \frac{\overline{\Xi^-}}{\overline{\Lambda}} \right|_{m_\perp > m_\perp^{\text{cut}}} = \gamma_s^2, \quad (22)$$

where we neglected resonance feed-down contribution in first approximation, which are of course considered in numerical studies [17]. Similarly we have

$$\gamma_s^2 = \left. \frac{\Lambda}{p} \cdot \frac{\overline{\Lambda}}{\overline{p}} \right|_{m_\perp > m_\perp^{\text{cut}}} = \left. \frac{\Omega^-}{2\Xi^-} \cdot \frac{\overline{\Omega^-}}{2\overline{\Xi^-}} \right|_{m_\perp > m_\perp^{\text{cut}}}, \quad (23)$$

where in the last relation the factors 2 in the denominator correct for the spin-3/2 nature of the  $\Omega$ .

Combining the experimental result Eq. (7) with Eqs. (22), we find the value  $\gamma_s = 0.55 \pm 0.04$ . In a full analysis [17] which accounts more precisely for resonance decay and flow, this result becomes

$$\gamma_s = 0.75 \pm 0.15. \quad (24)$$

In part, the error stems from the dependence of the resonance cascading on the temperature  $T_f$  at which the final state hadrons are formed, assuming that the relative population of different hadrons is determined by the thermal populations. The calculation of the resonance decay effect is actually not simple, since resonances at different momenta and rapidities contribute to a given daughter particle  $m_\perp$ . As the experimental measurements often sum the  $m_\perp$  distributions with  $m_\perp \geq m_\perp^{\text{cut}}$  it is convenient to consider this integrated abundance for particle ‘i’ at a given (central) rapidity  $y$ :

$$\left. \frac{dN_i}{dy} \right|_{m_\perp \geq m_\perp^{\text{cut}}} = \int_{m_\perp^{\text{cut}}}^{\infty} dm_\perp^2 \left\{ \frac{dN_i^0(T)}{dy dm_\perp^2} + \sum_R b_{R \rightarrow i} \frac{dN_i^R(T)}{dy dm_\perp^2} \right\}, \quad (25)$$

showing the direct ‘0’ contribution and the daughter contribution from decays into the observed channel  $i$ ) of resonances  $R \rightarrow i$ , with branching ratio  $b_{R \rightarrow i}$ , see Ref. [17, 56]. Extracting the degeneracy factors and fugacities of the decaying resonances, we write shortly

$$N_i^R \equiv \gamma_R \lambda_R \tilde{N}_i^R, \quad (26)$$

and imply that particles of same quantum numbers are comprised in each  $N_i^R$ . Here  $\gamma_R$  is the complete non-equilibrium factor of hadron (family)  $R$ . Between particles and anti-particles we have the relation

$$N_i^{\overline{R}} = \gamma_R \lambda_R^{-1} \tilde{N}_i^R = \lambda_R^{-2} N_i^R. \quad (27)$$

Thus the above considered particle ratios now become:

$$\left. \frac{\Xi^-}{\Xi^-} \right|_{m_\perp \geq m_\perp^{\text{cut}}} = \frac{\gamma_s^2 \lambda_q^{-1} \lambda_s^{-2} \tilde{N}_{\Xi^-}^* + \gamma_s^3 \lambda_s^{-3} \tilde{N}_{\Xi^-}^{\Omega^*}}{\gamma_s^2 \lambda_q \lambda_s^2 \tilde{N}_{\Xi^-}^* + \gamma_s^3 \lambda_s^3 \tilde{N}_{\Xi^-}^{\Omega^*}}, \quad (28)$$

$$\left. \frac{\bar{\Lambda}}{\Lambda} \right|_{m_\perp \geq m_\perp^{\text{cut}}} = \frac{\lambda_q^{-3} \tilde{N}_{\Lambda}^{N^*} + \gamma_s \lambda_q^{-2} \lambda_s^{-1} \tilde{N}_{\Lambda}^{Y^*} + \gamma_s^2 \lambda_q^{-1} \lambda_s^{-2} \tilde{N}_{\Lambda}^{\Xi^*}}{\lambda_q^3 \tilde{N}_{\Lambda}^{N^*} + \gamma_s \lambda_q^2 \lambda_s \tilde{N}_{\Lambda}^{Y^*} + \gamma_s^2 \lambda_q \lambda_s^2 \tilde{N}_{\Lambda}^{\Xi^*}}, \quad (29)$$

$$\left. \frac{\Xi^-}{\Lambda} \right|_{m_\perp \geq m_\perp^{\text{cut}}} = \frac{\gamma_s^2 \lambda_q \lambda_s^2 \tilde{N}_{\Xi^-}^* + \gamma_s^3 \lambda_s^3 \tilde{N}_{\Xi^-}^{\Omega^*}}{\lambda_q^3 \tilde{N}_{\Lambda}^{N^*} + \gamma_s \lambda_q^2 \lambda_s \tilde{N}_{\Lambda}^{Y^*} + \gamma_s^2 \lambda_q \lambda_s^2 \tilde{N}_{\Lambda}^{\Xi^*}}. \quad (30)$$

$\tilde{N}_{\Lambda}^{Y^*}$  contains also (in fact as its most important contribution) the electromagnetic decay  $\Sigma^0 \rightarrow \Lambda + \gamma$ .

Three different cases were considered [17] and results are presented in the table 1:

- A:** a thermal model without flow,  $\beta_f = 0$ , where the temperature  $T_f$  is assumed to correspond directly to the apparent value  $T_{\text{app}} = 232$  MeV following from the slope of the transverse mass spectra of high- $m_\perp$  strange (anti-)baryons;
- B:** a model with a freeze-out temperature of  $T_f \simeq 150$  MeV, *i.e.*, a value consistent with the kinetic freeze-out criterion developed in [54] and with lattice QCD data [3] on the phase transition temperature, which entails a flow velocity at freeze-out of  $\beta_f = 0.41$  in order to allow for the blue-shift of the transverse particle spectra inverse slope to the value  $T = 232$  MeV;
- C:** in order to maintain zero net strangeness in the HG fireball without additional off-equilibrium population factor characterizing the relative chemical equilibrium between strange meson and baryon abundances, the case  $T_f = 190$  MeV with  $\beta_f = 0.20$  was also explored.

Several interesting results can be deduced by inspection of the table 1:

1. The value of  $\lambda_q$  are little affected by resonance decays and by the origin of the slope of the  $m_\perp$ -spectrum (thermal or flow). The absolute value of the associated chemical potentials does by definition depend on the freeze-out temperature  $T_f$ .
2. The conclusion of [41] that the WA85 data on strange baryon and anti-baryon production from 200 GeV A S-W collisions establish a vanishing strange quark chemical potential is firmly confirmed, this result was found to remain stable under large variations in the freeze-out temperature and transverse flow velocity.

Table 1: Thermal fireball parameters extracted from the WA85 data [44] on strange baryon and anti-baryon production, for three different interpretations of the measured  $m_{\perp}$ -slope. Resonance decays were included. For details see text.

	<b>A</b>	<b>B</b>	<b>C</b>
T(MeV)	232	150	190
$\beta_f$	0	0.41	0.20
$\lambda_s$	$1.03 \pm 0.05$	$1.03 \pm 0.05$	$1.03 \pm 0.05$
$\mu_s/T$	$0.03 \pm 0.05$	$0.03 \pm 0.05$	$0.03 \pm 0.05$
$\mu_s$ (MeV)	$7 \pm 11$	$4 \pm 7$	$6 \pm 9$
$\lambda_q$	$1.49 \pm 0.05$	$1.48 \pm 0.05$	$1.48 \pm 0.05$
$\mu_q/T$	$0.40 \pm 0.04$	$0.39 \pm 0.04$	$0.39 \pm 0.04$
$\mu_B$ (MeV)	$278 \pm 23$	$176 \pm 15$	$223 \pm 19$
$\gamma_s$	$0.69 \pm 0.06$	$0.79 \pm 0.06$	$0.68 \pm 0.06$
$\varepsilon$	-0.22	0.37	0
$S/B$	$18.5 \pm 1.5$	$48 \pm 5$	$26 \pm 2.5$
$D_Q$	$0.135 \pm 0.01$	$0.08 \pm 0.01$	$0.12 \pm 0.01$

3. In the strangeness saturation factor  $\gamma_s$  the effects from resonance decays and flow can be clearly seen and are of magnitude 15%. However, no final state condition could be found allowing the chemical equilibrium value  $\gamma_s^{\text{eq}} = 1$ .

Particle production at  $T_f = 190$  leads to strangeness balanced emission, as indicated by the value of strangeness asymmetry in the produced particle population  $\varepsilon$ :

$$\varepsilon \equiv \frac{\langle \bar{s} \rangle - \langle s \rangle}{\langle s \rangle}, \quad (31)$$

If the fireball disintegrates into equilibrium abundances of meson and baryons, which is not necessarily the case in a sudden reaction picture, then the high  $T$  case (A) would lead to preferential emission of  $s$ -quarks, distilling a residue of  $\bar{s}$ -nuggets, while the low  $T$  case (B) would distill an  $s$ -nugget. This change in distillation properties of the evaporating fireball was noted long ago [55]. On the other hand, a suddenly disintegrating fireball should not be seen as leading to equilibrium meson to baryon abundances and this effect can restore the symmetric evaporation of strange and antistrange quarks, at the same time as the excess entropy content of the deconfined phase is resolved. We will discuss further the nonequilibrium hadronization features in section 8, while the entropy content of the fireball will preoccupy

our attention in section 8.2; the relevant variables are shown at the bottom of the table 1.

An avid reader of this analysis will of course observe that there are three independent particle ratios we have considered:

$$\Lambda/\bar{\Lambda}, \quad \Xi/\bar{\Xi}, \quad \bar{\Xi}/\bar{\Lambda}$$

(the fourth ratio is a product  $\Xi/\Lambda = \Xi/\bar{\Xi} \cdot \bar{\Xi}/\bar{\Lambda} \cdot \bar{\Lambda}/\Lambda$ ) but we also introduced here three parameters to be measured,  $\lambda_q, \lambda_s, \gamma_s$ . The question which can be posed is: are the properties we derive *consistent* with the other particle abundances? Is there a dynamical model which will lead to the here ‘measured’ values of the three parameters?

Looking at the baryon-antibaryon sector, there were two recent results that we have already described, that should be consistent with this analysis, the NA35  $\bar{\Lambda}/\bar{p}$  ratio [40] and the first determination of the  $\Omega$ -sector [39]. In both instances, the observed yields are as predicted when our original analysis was made [17] — this provides strong support for the usage of strange baryons as chemico-meters of rapidly dissociating fireball. We will return to discuss these results when we present the dynamical model which indeed leads to prediction of chemical properties with agreement with the results of this analysis (‘as has been measured’).

## 5 Thermal QGP fireball

### 5.1 QGP equations of state

The QGP equations of state (EoS) are of considerable relevance for the understanding of the magnitudes of different variables we consider here. We use a rather standard, perturbative/nonperturbative QCD improved set of relations based on the Fermi/Bose liquid model with thermal particle masses. The partition function of the interacting quark-gluon phase can be written as:

$$\ln Z^{\text{QGP}} = \sum_{i \in \text{QGP}} \frac{g_i(\alpha_s)V}{2\pi^2} \int \pm \ln \left( 1 \pm \gamma_i \lambda_i e^{-\sqrt{m_i^2(T)+p^2}/T} \right) p^2 dp, \quad (32)$$

where  $i = g, q, \bar{q}, s, \bar{s}$ , with  $\lambda_{\bar{i}} = \lambda_i^{-1}$  and  $\gamma_{\bar{i}} = \gamma_i$ . We take into account the QCD interactions between quarks and gluons by allowing for thermal masses

$$m_i^2(T) = (m_i^0)^2 + (cT)^2. \quad (33)$$

For the current quark masses we take:

$$m_q^0 = 5 \text{ MeV}, \quad m_s^0 = 160 \text{ MeV}, \quad m_g^0 = 0.$$

We have  $c^2 \propto \alpha_s$ ,  $\alpha_s$  being the QCD coupling constant. We fix  $c = 2$ , arising for  $\alpha_s \sim 1$  (the exact value was not of essence), while also allowing for another effect of the QCD-interactions, the reduction of the number of effectively available degrees of freedom: we implement the following effective counting of gluon and quark degrees of freedom, motivated by the perturbative QCD formulæ:

$$\begin{aligned} g_g = 16 &\quad \rightarrow \quad g_g(\alpha_s) = 16 \left( 1 - \frac{15\alpha_s}{4\pi} \right), \\ g_{i-T} = 6 &\quad \rightarrow \quad g_{i-T}(\alpha_s) = 6 \left( 1 - \frac{50\alpha_s}{21\pi} \right), \\ g_{i-B} = 6 &\quad \rightarrow \quad g_{i-B}(\alpha_s) = 6 \left( 1 - 2\frac{\alpha_s}{\pi} \right), \end{aligned} \quad (34)$$

where  $i = u, d$  (we do not correct the strange quark degeneracy). In Eq. (34) two factors are needed for quarks: the factor  $g_{i-T}$  controls the expression when all chemical potentials vanish (the  $T^4$  term in the partition function for massless quarks) while  $g_{i-B}$  is taken as coefficient of the additional terms which arise in presence of chemical potentials. We took  $\alpha_s = 0.6$  which turned out to be the value best suited for the experimental data points. We explore the physical properties of the QGP fireball by considering the constraint between  $T, \lambda_q$  arising from a given initial specific energy content<sup>3</sup>  $E/B$ . The collision energy gives us the values of the constraints to consider:

$$\frac{E}{B} = \frac{\eta_E E_{CM}}{\eta_B A_{\text{part}}} \simeq \frac{E_{CM}}{A_{\text{part}}}, \quad (35)$$

where  $\eta_E$  and  $\eta_B$  are respectively the stopping fraction [57] of energy and baryonic number and  $A_{\text{part}}$  is the number of nucleons participating in the reaction. The last equality follows when the stopping fractions are equal — the experimental particle spectra we are addressing here, and in particular the visible presence of baryons in the central rapidity region, are implying that this is a reasonable assumption for the current experimental domain. In consequence, the energy per baryon in the fireball is to be taken as being equal to the kinematic energy available in the collision. In the current laboratory target experiments we have the following kinematic energy content:

---

<sup>3</sup>Here  $B$  is the baryon number. To avoid confusion, below the bag constant is denoted  $\mathcal{B}$ .



Au–Au at 10.5A GeV	→	$E/B = 2.3$ GeV ,
Si–Au at 14.6A GeV	→	$E/B = 2.6$ GeV ,
A–A at 40A GeV	→	$E/B = 4.3$ GeV ,
Pb–Pb at 158A GeV	→	$E/B = 8.6$ GeV ,
S–W/Pb at 200A GeV	→	$E/B = 8.8$ GeV ,
S–S at 200A GeV	→	$E/B = 9.6$ GeV ,

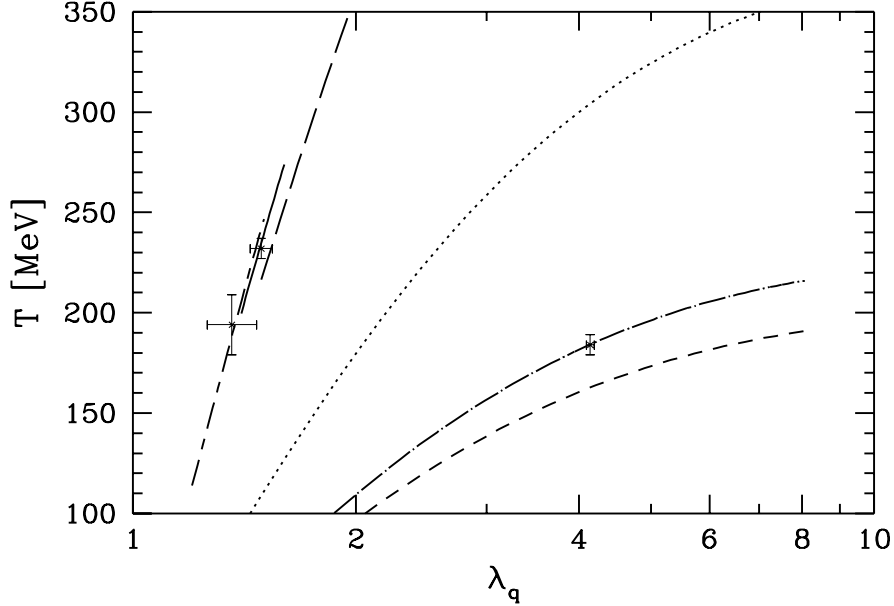


Figure 13: QGP-EoS constraint between temperature  $T$  and light quark fugacity  $\lambda_q$  for a given fireball energy content per baryon  $E/B$  appropriate for the AGS and SPS collision systems. Left to right: 2.3 (Au–Au), 2.6 (Si–Au), 4.3 (A–A), 8.6 (Pb–Pb), 8.8 (S–PB/W) and 9.6 (S–S) GeV. See text for a discussion of experimental point.

Note that above we assumed collision with the geometric target tube of matter [20], see section 2, when the projectile is smaller than the target. In Fig. 13 we show in the  $T$ – $\lambda_q$  plane the lines corresponding to this constraint on the QGP-EoS. In the middle the line corresponding to the lowest SPS accessible energy, 4.3 GeV, is depicted, which bridges the current SPS domain shown to the left to the BNL region on the lower right. The experimental crosses show the values of  $\lambda_q$  arising in our data analysis [17, 51, 52], combined with the inverse slope temperatures, extracted from transverse mass particle spectra. The fact that the experimental results fall on the lines shown in Fig. 13 is primarily due to the choice  $\alpha_s = 0.6$  — as this is

the usual value in this regime of energy it implies for a QGP fireball EoS hypothesis that the assumption that stopping of energy and baryon number is similar deserves further consideration.

## 5.2 Initial conditions and fireball evolution

There now remains the issue what physical constraint or principle determines which of the possible pair of  $T$ ,  $\lambda_q$  values along the individual curves depicted in Fig. 13 (see experimental crosses shown) is actually initially reached in the reaction. We have explored the properties of the QGP phase along these lines of constant energy per baryon and have noticed that with increasing  $T$  the pressure in the QGP phase increases, and that the experimental points coincide with the dynamical pressure generated in the collision. This gives birth to the intuitive idea that the initial conditions reached in the central fireball arise from the equilibrium between the fireball internal thermal pressure and the external compression pressure.

This condition takes the form [18]:

$$P_{\text{th}}(T, \lambda_i, \gamma_i) = P_{\text{dyn}} + P_{\text{vac}}. \quad (36)$$

The thermal pressure follows in usual way from the partition function

$$P_{\text{th}} = T/V \ln Z(T, \lambda_q, \lambda_s; \gamma_g, \gamma_q, \gamma_s), \quad (37)$$

where aside of the temperature  $T$ , we encounter the different fugacities  $\lambda_i$  and the chemical saturation factors  $\gamma_i$  for each particle. For the vacuum pressure we will use:

$$P_{\text{vac}} \equiv \mathcal{B} \simeq 0.1 \text{ GeV}/\text{fm}^3. \quad (38)$$

The pressure due to kinetic motion follows from well-established principles, and can be directly inferred from the pressure tensor [58]

$$T^{ij}(x) = \int p^i u^j f(x, p) d^3p, \quad i, j = 1, 2, 3. \quad (39)$$

We take for the phase-space distribution of colliding projectile and target nuclei

$$f_{\text{P,T}}(x, p) = \rho_{\text{P,T}}(x) \delta^3(\vec{p} \pm \vec{p}_{\text{CM}}), \quad (40)$$

and hence in Eq. (39)  $u^j = \pm p_{\text{CM}}^j / E_{\text{CM}}$ . We assume that the nuclear density is uniform within the nuclear size,  $\rho_0 = 0.16 / \text{fm}^3$ .

To obtain the pressure exerted by the flow of colliding matter, we consider the pressure component  $T^{jj}$ , with  $j$  being the direction of  $\vec{v}_{\text{CM}}$ . This gives

$$P_{\text{dyn}} = \eta_p \rho_0 \frac{p_{\text{CM}}^2}{E_{\text{CM}}}. \quad (41)$$

Here it is understood that the energy  $E_{\text{CM}}$  and the momentum  $p_{\text{CM}}$  are given in the nucleon–nucleon CM frame and  $\eta_p$  is the momentum stopping fraction — only this fraction  $0 \leq \eta_p \leq 1$  of the incident CM momentum can be used by a particle incident on the central fireball (the balance remains in the unstopped longitudinal motion) in order to exert dynamical pressure. For a target transparent to the incoming flow, there would obviously be no pressure exerted. The simple expression Eq. (41) is illustrated in Fig. 14 as function of the stopping fraction. At current energies with stopping being above 50% we explore the conditions above  $0.7 \text{ GeV}/\text{fm}^3$ .

We now can determine the initial conditions reached in heavy ion col-

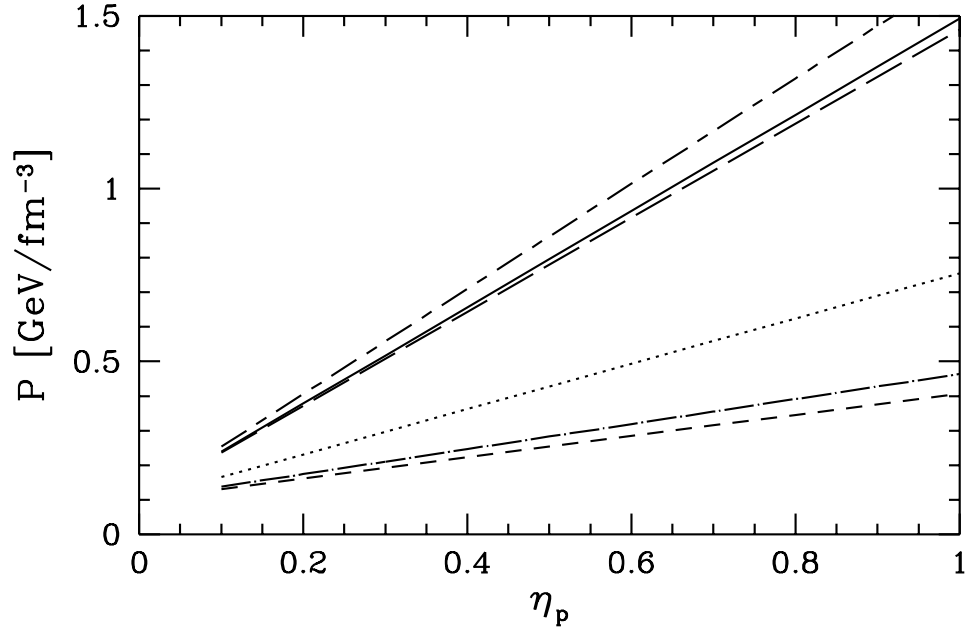


Figure 14: The collision pressure  $P$  as function of momentum stopping  $\eta_p$  for different values of  $E/B$  — 2.3, 2.6, 4.3, 8.6, 8.8 and 9.6 GeV (from bottom to top, solid line is for 8.8 GeV), from Ref. [18].

Table 2: Properties and evolution of different collision systems.

Phase space occupancy	$\langle s - \bar{s} \rangle = 0$ $\lambda_s \equiv 1$	$E/B$ [GeV]					
		2.35	2.6	4.3	8.8	8.6	8.6
		$\eta = 1$ Au-Au	$\eta = 1$ Si-Au	$\eta = 1$ Pb-Pb	$\eta = 0.5$ S-Pb	$\eta = 0.75$ Pb-Pb	$\eta = 1$ Pb-Pb
$\gamma_q = 0.2$	$T_{th}$ [GeV]	0.238	0.260	0.361	0.410	0.444	0.471
	$\lambda_q$	13.3	9.95	3.76	1.78	1.91	2.00
	$n_g/B$	0.15	0.20	0.54	1.55	1.36	1.25
	$n_q/B$	3.00	3.00	3.13	5.12	3.89	3.77
	$n_{\bar{q}}/B$	0.00	0.00	0.13	2.12	0.89	0.77
$\gamma_g = 0.2$	$n_{\bar{q}}/B$	0.00	0.00	0.13	2.12	0.89	0.77
	$n_{\bar{s}}/B$	0.02	0.02	0.06	0.16	0.14	0.13
	$P_{th}$ [GeV/fm <sup>3</sup> ]	0.42	0.46	0.76	0.79	1.12	1.46
$\gamma_s = 0.03$	$\rho_B$	3.34	3.34	3.30	1.70	2.44	3.18
	$S/B$	10.7	11.8	18.8	40.0	35.8	33.4
	$T_{ch}$ [GeV]	0.200	0.212	0.263	0.280	0.304	0.324
$\gamma_q = 1$	$\lambda_q$	4.92	4.14	2.36	1.49	1.56	1.61
	$n_g/B$	0.47	0.56	1.08	2.50	2.24	2.08
	$n_q/B$	3.06	3.11	3.51	5.16	4.81	4.62
$\gamma_g = 1$	$n_{\bar{q}}/B$	0.06	0.11	0.51	2.16	1.81	1.62
	$n_{\bar{s}}/B$	0.04	0.05	0.11	0.25	0.22	0.21
	$P_{ch}$ [GeV/fm <sup>3</sup> ]	0.42	0.46	0.76	0.79	1.12	1.46
$\gamma_s = 0.15$	$\rho_B$	3.34	3.35	3.31	1.80	2.45	3.19
	$S/B$	11.0	12.3	19.7	41.8	37.4	34.9
	$\gamma_s$	1	1	1	0.8	1	1
$\gamma_q = 1$	$T_0$ [GeV]	0.176	0.184	0.215	0.233	0.239	0.255
	$\lambda_q$	4.92	4.14	2.36	1.49	1.56	1.61
$\gamma_g = 1$	$n_g/B$	0.47	0.56	1.08	2.50	2.25	2.09
	$n_q/B$	3.11	3.06	3.51	5.12	4.81	4.60
	$n_{\bar{q}}/B$	0.06	0.11	0.51	2.12	1.81	1.62
$\gamma_s = 0.8$ or $\gamma_s = 1$	$n_{\bar{s}}/B$	0.29	0.34	0.68	1.27	1.43	1.33
	$P_0$ [GeV/fm <sup>3</sup> ]	0.28	0.30	0.41	0.47	0.54	0.71
$\gamma_s = 1$	$\rho_B$	2.29	2.17	1.80	1.05	1.19	1.56
	$S/B$	12.9	14.5	24.0	49.5	46.5	43.4

lisions, since the two constraints, energy per baryon and pressure allow to fix the values of  $\lambda_q$  and  $T$ , provided that we make a hypothesis about the degree of chemical equilibration of the state considered. In order to have some understanding of the conditions prevailing in the early stages

of the collision process, when the thermal equilibrium is reached, but the chemical equilibrium for all components is still far away, we take 20% occupancy for gluons and light quarks, and 3% for strange quarks and solve the EoS for  $T_{\text{th}}$ , and the associated  $\lambda_{\text{q}}$  which are shown along with other interesting properties of the fireball (number of gluons per baryon, number of light quarks and antiquarks per baryon, number of anti-strange quarks per baryon, the pressure in the fireball, baryon density and the entropy per baryon) in the top section of the table 2. Because the QGP phase is strangeness neutral we have always  $\lambda_{\text{s}} = 1$ . The columns of table correspond to the cases of specific experimental interest, in turn: Au–Au and Si–Au collisions at AGS, possible future Pb–Pb collisions at SPS with 40A GeV, S–Pb at 200A GeV, and for the Pb–Pb collisions at 158A GeV we considered two possible values of stopping, see Eq. (41):  $\eta = 0.75$  and  $\eta = 1$ .

Next in our consideration of the system is the configuration when the  $u$ ,  $d$  quarks and gluons have reached their chemical equilibrium abundances,  $\gamma_{\text{q}} \rightarrow 1$ ,  $\gamma_{\text{g}} \rightarrow 1$ .  $T_{\text{ch}}$  and  $\lambda_{\text{q}}$  are shown in the middle section of the table 2. It is worth observing that the baryon density in the fireball introduces from the onset a rather large quark density, which thus needs not to be produced, and thus the approach to chemical equilibrium of the light quarks is here faster than in the baryon-free central region environments expected at much higher RHIC/LHC energies. It can be argued that this partial (excluding strangeness) chemical equilibrium occurs at the end of the nuclear penetration, about 1.5 fm/c after the beginning of the collision. Though of major physical interest this observation has no relevance to the results we present below. There is no change in the pressure between top and middle sections of table 2, as the dynamical compression with the given  $P$  is present at this stage of the fireball evolution. But we see here that  $T_{\text{th}} > T_{\text{ch}}$ , since the number of quarks and gluons present is considerably lower in the early stages of the collision.

At  $T_{\text{ch}}$  the strange flavor is still far from equilibrium and we considered  $\gamma_{\text{s}}(t = 1.5 \text{ fm}) \simeq 0.15$ , appropriate for strange quark relaxation time 7 times larger than the light quark one [59]. The exact initial value is of little consequence for the final yields, since we find near saturation of strangeness abundance.

After the collision has ended, for times  $1.5 \leq t \leq 5\text{--}10 \text{ fm/c}$ , the strange quarks relax to their equilibrium abundance and the temperature drops from  $T_{\text{ch}}$  to the value  $T_0$ , shown along with other properties in the bottom section of table 2. We make exception to this full chemical equilibrium for

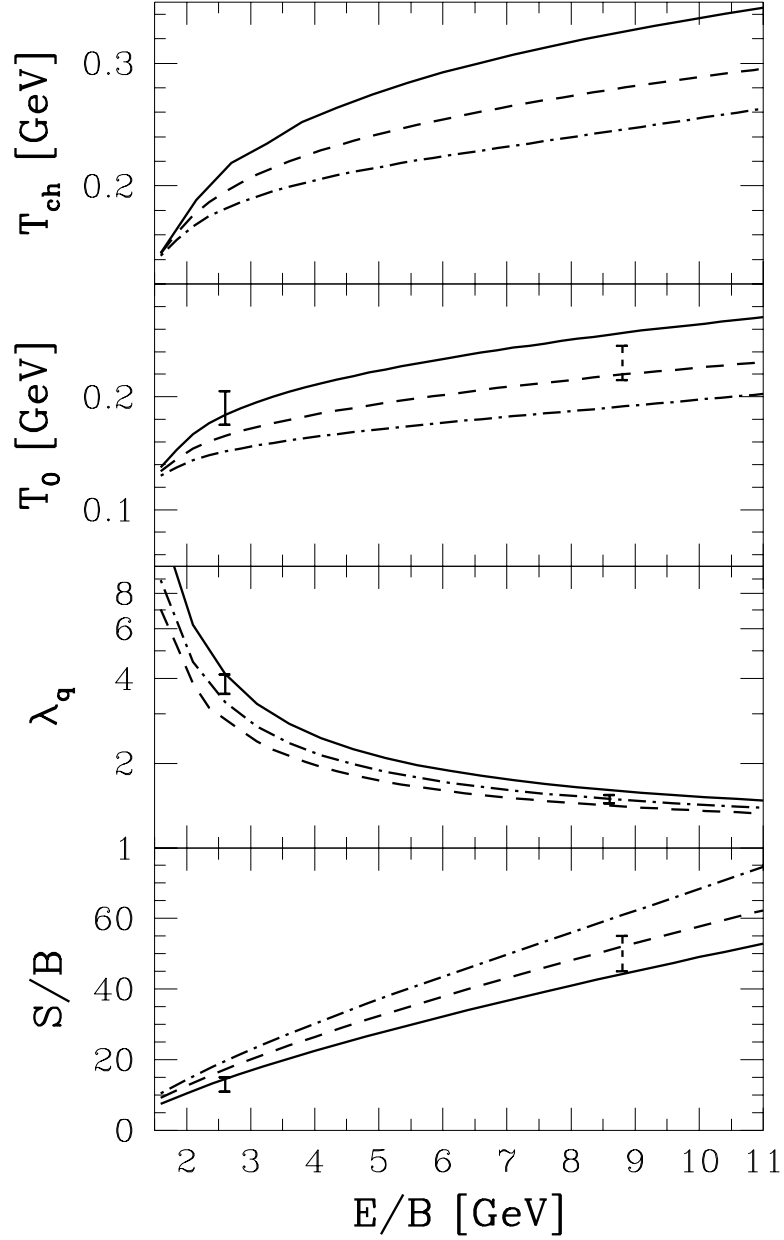


Figure 15: Initial fireball temperature  $T_{ch}, T_0$ , light quark fugacity  $\lambda_q$  and entropy per baryon  $S/B$  at the time of maximum chemical equilibration, as function of the QGP-fireball energy content  $E/B$ ; stopping  $\eta = 1$  (solid line),  $1/2$  (dot-dashed line) and  $1/4$  (dashed line). See text for comparison with analysis results.

the S–W case, for which we assume that strange quarks have reached 80% of phase space occupancy as suggested by the experimental results [17, 60]. During the formation of the strangeness flavor there is already evolution of the fireball outside of the collision region and we allow for this by keeping  $\lambda_q = \text{Const.}$ . This effectively freezes the entropy content of gluons and light quarks, allowing for significant drop in pressure and some cooling due to conversion of energy into strangeness. Aside of this chemical cooling [53], there is cooling due to (adiabatic) expansion of the fireball, in which  $\lambda_q = \text{Const.}$ , such that  $T$  decreases from  $T_{\text{ch}}$  to the full chemical equilibrium value  $T_0$ . We consider also in the simple model calculations devoted to the study of the strangeness production in section 7, see Fig. 32.

For the S–Pb/W collisions the temperature values shown in the bottom portion of the table are similar to the inverse slopes observed in particle spectra and shown in Fig. 13. Remarkably, the values of temperature  $T_0$  found for the case of  $E/B = 8.6$  GeV at  $\eta = 0.5$  is just 233 MeV, which corresponds nearly exactly to the reported inverse slopes of the WA85 results [44], and  $\lambda_q = 1.49$  also agrees exactly with the results of our analysis [17], also shown in Fig. 13. Even though there are a number of tacit and explicit parameters (in particular  $\eta = 0.5, \alpha_s = 0.6$ ) we believe that this result supports strongly the validity of our model involving the QGP fireball.

It is of interest for many applications to determine the initial fireball conditions systematically as function of the specific energy. In Fig. 15 we show as function of the specific energy content  $E/B$ , in top portion the behavior of temperature  $T_{\text{ch}}$  at which light quarks and gluons have reached chemical equilibrium. Below it, we show values of  $T_0$ , determined by requiring that also strange quarks are in chemical equilibrium. In the next segment of the figure the fireball light quark fugacity  $\lambda_q$  and in the bottom section the entropy per baryon  $S/B$  at maximum chemical equilibration in the QGP fireball. The experimental bars show for high (8.8 GeV) energy the result of the data analysis [17] discussed above, and those for low energy (2.6 GeV) are taken from the analysis of the AGS data [51, 52]. The range of the possible values as function of stopping  $\eta$  is indicated by showing the results for  $\eta = 1$  (solid line),  $1/2$  (dot-dashed line) and  $1/4$  (dashed line). These results are in many respects fulfilling our expectations. We note the drop in temperature with decreasing energy and stopping; for a given specific energy the value of  $\lambda_q$  is relatively insensitive to the stopping power; there is a (rapid) rise of specific entropy with  $E/B$ .

### 5.3 Difference between AGS and SPS energy range

In the analysis of the collisions of S-ions at 200A GeV with different nuclear targets carried out at SPS we have shown in the framework of the thermal model that the strange-quark fugacity is  $\lambda_s \simeq 1$ , i.e.,  $\mu_s = 0$ , see section 3.3. Even a cursory look [51,52] at the AGS results [61,62,63] shows that  $\mu_s \neq 0$ , actually  $\lambda_s \simeq 1.7$  and  $\lambda_q \simeq 3.6$ . This implies that in Si-Au 15A GeV collisions the final state particles are not displaying the required symmetry properties expected for a deconfined source. This implies that:

- the deconfined phase was not formed at all in these ‘low’ energy collisions, or,
- that complete re-equilibration occurs when the primordial deconfined high baryon density matter hadronizes.

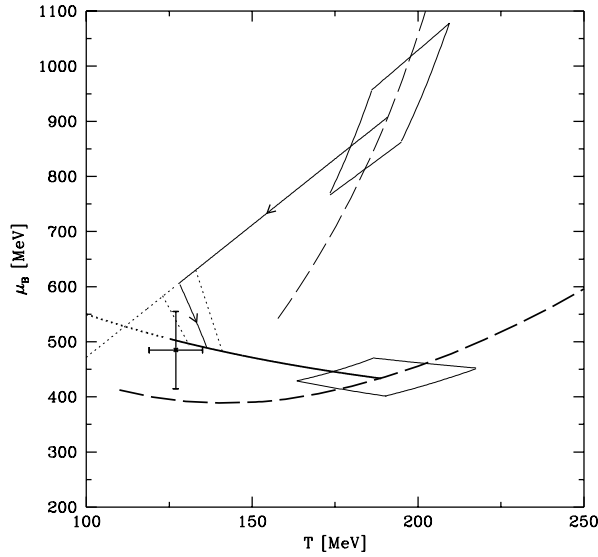


Figure 16:  $\mu_B$ - $T$  plane with thick lines: HG model; thin lines: QGP model. Dashed lines: fixed energy per baryon  $E/B = 2.55$  GeV, lower for HG, upper for QGP. Solid lines: fixed specific entropy  $S/B = 13$ , upper for QGP, lower for HG model. Trapezoidal regions enclose the initial condition, given the experimental uncertainty (see [52]). Solid line connecting QGP and HG with dotted lines left/right: possible phase transition at  $P = 0.04 \pm 0.01$  GeV/fm<sup>3</sup>. Note that continuations of  $S/B = 13$  lines beyond transition/hadronization are shown dotted, after Ref. [52].

In Fig.16 we show in the  $\mu_B$ - $T$  plane for the HG case (thick lines) and QGP case (thin lines) the two different hypothetical histories of the



collision. The dashed lines show the constraint arising from consideration of the fixed energy per baryon 2.55 GeV  $A$  in the CM frame for HG (upper-) and QGP (lower line), while the solid lines are for fixed specific entropy per baryon  $S/B = 13$ , deduced from the particle abundance observed in the final state [52]. Where the solid and dashed lines meet, within a trapezoidal region determined by one unit error in entropy and an error of 0.15 GeV in CM energy, we have a consistency conditions satisfied between the initial specific energy and the final state entropy, thus presumably these are the initial values of thermal parameters for the two phases. The initial HG state (for  $S/B = 13$ ,  $E/B = 2.55$  GeV) has an energy density  $\varepsilon_0^{\text{HG}} = 2.3$  GeV fm $^{-3}$ , and baryon density  $\rho_0^{\text{HG}} = 6\rho_N$ . The initial pressure is  $P_0^{\text{HG}} = 0.3$  GeV fm $^{-3}$ . In the QGP phase we find  $\varepsilon_0^{\text{QGP}} = 1.2$  GeV fm $^{-3}$ ,  $\rho_0^{\text{QGP}} = 2.9\rho_N$ ,  $P_0^{\text{QGP}} = 0.39$  GeV fm $^{-3}$ . Somewhat surprisingly, the QGP is the more dilute phase at these condition. Kinetic HG simulations such as ARC [64] also reach such rather high baryon and energy densities in these collisions.

We also obtain very large difference in  $\mu_B$  which takes an initial value  $\mu_0^{\text{HG}} = 440 \pm 40$  MeV in the HG scenario and  $\mu_0^{\text{QGP}} = 910 \pm 150$  MeV in the QGP case — not shown in the Fig. 16 is that the strangeness conservation requirement leads in the HG to an *initial* value  $\mu_{s,0}^{\text{HG}} = 0$ , just as is in the case of the QGP. We see in Fig. 16 that the initial temperatures  $T_0$  for QGP and HG scenarios are practically equal. For  $E/B = 2.55 \pm 0.15$  GeV and  $S/B = 13 \pm 1$  we have  $T_0 = 190 \pm 30$  MeV. The QGP fireball at  $S/B = 13$  (thin solid line) evolves practically at fixed  $\lambda_q = 4.8$  and  $\lambda_s = 1$ . However, for the HG fireball at fixed  $S/B = 13$  (thick solid line) there is a strong variation in both these fugacities but the ratio  $R_\lambda^{\text{HG}} = \lambda_q/\lambda_s = 2.17$  remains practically constant, assuring that the specific entropy is constant [52]. The ‘experimental’ cross is set at  $\mu_{B,f} = 485 \pm 70$  MeV and  $T_f = 127 \pm 8$  MeV corresponding to the freeze-out conditions (with  $\mu_{s,f} = 68$  MeV) deduced from the final state particle spectra and abundances [52]. However, in a three dimensional display including  $\lambda_s$  we would see that only the HG is consistent with the freeze-out point.

In Fig. 16 the connecting nearly vertical lines between the two evolution paths (QGP/HG) denote a possible phase transformation from QGP to HG. This was obtained assuming a first order phase transition and using the equations of state of both phases with bag pressure  $\mathcal{B} = 0.1$  GeV fm $^{-3}$  (corresponding to  $\mathcal{B}^{1/4} = 170$  MeV) — we note that there is minor re-heating occurring while the baryochemical potential drops by 15% — however, the

major re-equilibration is in the jump from  $\lambda_s = 1$  in the plasma to  $\lambda_s \sim 1.7$  in the HG phase. Thus the ‘short’ connection between the QGP to HG paths would be considerably stretched in full three dimensional display, reflecting on the need to well re-equilibrate the matter in transition, due to substantial differences in the properties of the QGP and HG phases reached at AGS energies.

Given considerable differences in the statistical parameters in the two evolution scenarios, and the different initial baryon and energy densities that would be reached, we believe [52] that it is possible to distinguish between HG and QGP reaction alternatives at AGS energies, though a critical test has not been proposed yet.

## 6 Thermal flavor production

### 6.1 Population evolution

The production of heavy flavor is a considerably slower process compared to the multitude of different reactions possible in a quark-gluon gas, which are leading to redistribution of energy between the available particles and lead to thermal equilibrium. Thus even if we assume without microscopic understanding that thermal equilibration is rapid, we should not expect the chemical (i.e., particle abundance) equilibrium to be present, especially so for heavy flavor. A well studied example of this situation is strangeness production which constitutes a bottleneck in (chemical) equilibration of strongly interacting confined matter.

We will evaluate in the following the dominant particle fusion contributions to the relaxation constant  $\tau_s$  of strangeness. The first order strangeness production processes at fixed values of  $\alpha_s = 0.6$  and  $m_s = 160\text{--}180$  MeV, have been studied 14 years ago [49, 59]. Thermal non-perturbative effects were more recently explored in terms of thermal temperature dependent particle masses [65]. After the new production rates, including the now possible thermal gluon decay, were added up, the total strangeness production rate was found little changed compared to the free space rate. This finding was challenged [66], but a more recent reevaluation of this work [67] confirmed that the rates obtained with perturbative glue-fusion processes are describing precisely the strangeness production rates in QGP, for the here relevant  $T > 250$  MeV temperature range. A fuller discussion of this matter is given in a recent review [8]. Thus we can safely assume today that the first order strangeness production processes are dominating

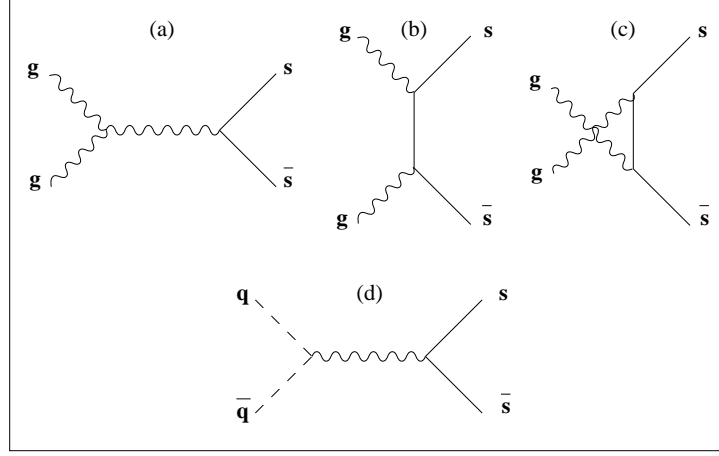


Figure 17: Lowest-order Feynman diagrams for production of  $s\bar{s}$  (and similarly  $c\bar{c}$ ) by gluon fusion and quark pair fusion.

the strangeness production rates in QGP, with  $\tau_s \simeq 2$  fm/ $c$  for the here relevant  $T > 250$  MeV temperature range, see Fig. 23 below. In the next section 6.3 we will address the higher order production processes.

We first consider the angle averaged flavor production cross sections. The evaluation of the lowest order diagrams shown in Fig. 17 yields [68]:

$$\bar{\sigma}_{gg \rightarrow s\bar{s}}(s) = \frac{2\pi\alpha_s^2}{3s} \left[ \left( 1 + \frac{4m_s^2}{s} + \frac{m_s^4}{s^2} \right) \tanh^{-1}W(s) - \left( \frac{7}{8} + \frac{31m_s^2}{8s} \right) W(s) \right], \quad (42)$$

$$\bar{\sigma}_{q\bar{q} \rightarrow s\bar{s}}(s) = \frac{8\pi\alpha_s^2}{27s} \left( 1 + \frac{2m_s^2}{s} \right) W(s). \quad (43)$$

where  $W(s) = \sqrt{1 - 4m_s^2/s}$ . We see in Fig. 18 that the magnitude of both cross sections is similar.

With the production cross sections known, the net change in the strange quark abundance (and similarly charm, though here the annihilation rate is negligible) is given by the difference between the production and annihilation rates. Thus the evolution of flavor abundance in the QGP can be quite simply described by the population equation:

$$\frac{d\rho_s(t)}{dt} = \frac{dN(gg, q\bar{q} \rightarrow s\bar{s})}{d^3x dt} - \frac{dN(s\bar{s} \rightarrow gg, q\bar{q})}{d^3x dt}. \quad (44)$$

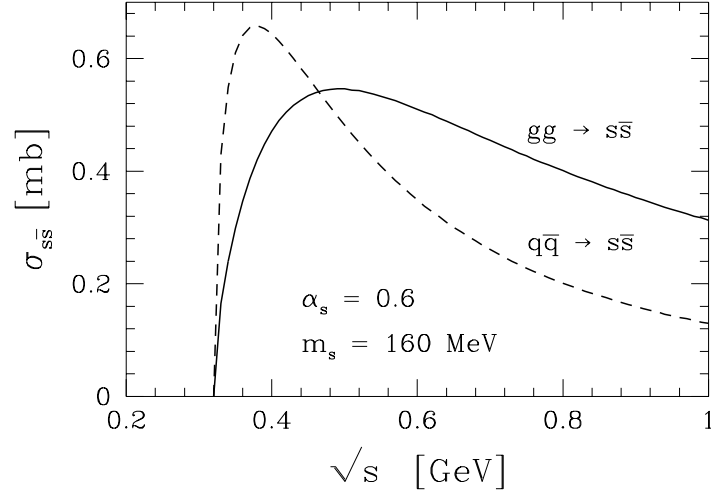


Figure 18: Strangeness production cross sections for  $\alpha_s = 0.6$ ,  $m_s = 160$  MeV.

This can be expressed in terms of the thermally averaged cross sections  $\langle\sigma v_{\text{rel}}\rangle_T$  and particle densities  $\rho$ :

$$\begin{aligned} \frac{d\rho_s(t)}{dt} = & \rho_g^2(t) \langle\sigma v\rangle_T^{gg\rightarrow s\bar{s}} \\ & + \rho_q(t)\rho_{\bar{q}}(t) \langle\sigma v\rangle_T^{q\bar{q}\rightarrow s\bar{s}} - \rho_s(t)\rho_{\bar{s}}(t) \langle\sigma v\rangle_T^{s\bar{s}\rightarrow gg,q\bar{q}}. \end{aligned} \quad (45)$$

In chemical equilibrium, the strange quark density is a constant in time. Setting the left hand side of Eq. (45) equal to 0, we find the detailed balance relation for  $t \rightarrow \infty$ :

$$(\rho_g^\infty)^2 \langle\sigma v\rangle_T^{gg\rightarrow s\bar{s}} + \rho_q^\infty \rho_{\bar{q}}^\infty \langle\sigma v\rangle_T^{q\bar{q}\rightarrow s\bar{s}} = \rho_s^\infty \rho_{\bar{s}}^\infty \langle\sigma v\rangle_T^{s\bar{s}\rightarrow gg,q\bar{q}}. \quad (46)$$

Eq. (46) relates the thermally averaged strangeness annihilation rate to the production rate. We substitute it into Eq. (45). Furthermore, since the kinetic and chemical equilibration of light quarks and gluons occurs on a considerably shorter time scale than the production of strangeness, we can assume that the gluon and light quark density is continually replenished through other channels so that

$$\rho_g(t) \rightarrow \rho_g^\infty; \quad \rho_q(t) \rightarrow \rho_q^\infty; \quad \rho_{\bar{q}}(t) \rightarrow \rho_{\bar{q}}^\infty,$$

and we obtain inserting this also into Eq. (45):

$$\frac{d\rho_s(t)}{dt} \equiv \frac{dN_s(t)}{dV dt} = (A_{gg} + A_{q\bar{q}}) \left[ 1 - \left( \frac{\rho_s(t)}{\rho_s^\infty} \right)^2 \right]; \quad (47)$$

where we also have made use of the fact that  $\rho_s \rho_{\bar{s}} = \rho_s^2$  in QGP, and  $A$  is as defined by

$$A_{AB} = \langle \sigma_{AB}^s v_{AB} \rangle_T \rho_A^\infty \rho_B^\infty; \quad (48)$$

We can easily solve Eq. (47) analytically, when it is possible to assume that the (invariant) production rate  $A = A_{q\bar{q}} + A_{gg}$  per unit volume and time is a constant in time:

$$\begin{aligned} \gamma_s(t) \equiv \frac{\rho_s(t)}{\rho_s^\infty} &= \tanh(t/2\tau_s) \quad \text{for } A = \text{Const.} \\ &\simeq (1 - 2e^{-t/\tau_s}) \quad \text{for } t > \tau_s. \end{aligned} \quad (49)$$

We see that the asymptotic limit is approached from below exponentially.  $\tau_s$  is referred to as the relaxation time constant, here for strangeness (and similarly charm) production in QGP and is given by:

$$\tau_s \equiv \frac{1}{2} \frac{\rho_s^\infty}{(A_{gg} + A_{q\bar{q}} + \dots)}, \quad (50)$$

where the dots indicate that other mechanisms may contribute to the heavy flavor production, further reducing the relaxation time. The equilibrium

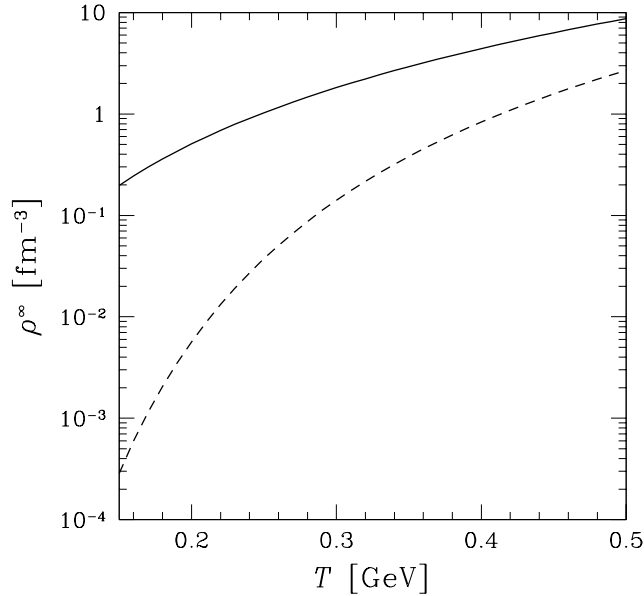


Figure 19: The statistical equilibrium density of strange or antistrange quarks with  $m_s = 160$  MeV (solid line) and charmed or anticharmed quarks with  $m_c = 1500$  MeV (dashed line) as function of temperature  $T$ .

abundance of heavy quarks and antiquarks in the QGP  $\rho_s^\infty$  is given by the convergent series expansion:

$$N_s^\infty = \frac{3}{\pi^2} V T^3 x^2 k_2(x), \quad x = \frac{m_s}{T}, \quad (51)$$

with:

$$k_2(x) \equiv \sum_{l=1}^{\infty} \frac{(-)^{l+1}}{l} K_2(lx). \quad (52)$$

The first term in the expansion Eq. (52) leads to the Boltzmann approximation. The equilibrium density of strange ( $m_s = 160$  MeV) and charmed ( $m_c = 1500$  MeV) quarks is shown in Fig. 19. We note that for  $T \simeq 250$  MeV strangeness equilibrium abundance exceeds one  $\bar{s}$ -quark for each  $\text{fm}^3$  of matter, which charm reaches for  $T \geq 450$  MeV. However, as we shall see, charm production is too slow to reach the equilibrium within the life span of the dense matter and hence this remark is presently only of academic interest.

## 6.2 Thermal strangeness production

We now determine the thermal strangeness production rate:

$$A_s \equiv A_{gg} + A_{u\bar{u}} + A_{d\bar{d}} = \sum_{AB} \langle \sigma v_{AB} \rangle_T \rho_A^\infty \rho_B^\infty = \frac{dN(gg, q\bar{q} \rightarrow s\bar{s})}{d^3x dt}. \quad (53)$$

Thus the general expression for  $A_s$  is:

$$A_s = \int_{4m_s^2}^{\infty} ds 2s \delta(s - (p_A + p_B)^2) \int \frac{d^3p_A}{(2\pi)^3 2E_A} \int \frac{d^3p_B}{(2\pi)^3 2E_B} \times \left[ \frac{1}{2} g_g^2 f_g(p_A) f_g(p_B) \overline{\sigma_{gg}}(s) + n_f g_q^2 f_q(p_A) f_{\bar{q}}(p_B) \overline{\sigma_{q\bar{q}}}(s) \right]. \quad (54)$$

where in principle the particle distributions  $f_i$  could be different from the thermal Bose/Fermi functions we will use here. The bar over the cross sections indicates that we use angle-averaged expressions. In order to obtain the above form, we have introduced a dummy integration over  $s$  and have employed for the relative velocity between two particles

$$\begin{aligned} v_{AB} 2E_A 2E_B &\equiv 2 \lambda^{1/2}(s) \\ &= 2 \sqrt{s - (m_A + m_B)^2} \sqrt{s - (m_A - m_B)^2} \rightarrow 2s, \end{aligned} \quad (55)$$

where the last limit holds for (nearly) massless particles.

We are interested to understand at which values of  $\sqrt{s}$  the actual production processes occur, in order to establish the value of  $\alpha_s$  we should employ. We rewrite the thermal production rate Eq.(54) as an integral over the differential rate  $dA/ds$ :

$$A_i \equiv \int_{4m_i^2}^{\infty} ds \frac{dA_i}{ds} \equiv \int_{4m_i^2}^{\infty} ds \bar{\sigma}_i(s) P_i(s) \quad i = g, q. \quad (56)$$

Here  $P_g(s)ds$  is the number of gluon collisions within the interval of invariant mass  $(s, s + ds)$  per unit time per unit volume, with a similar interpretation applying to  $P_q(s)$ . From Eq. (54) we find:

$$P_g(s) = \frac{1}{2} g_g^2 \int \frac{d^3 p_A f_g(p_A)}{(2\pi)^3 2E_A} \frac{d^3 p_B f_g(p_B)}{(2\pi)^3 2E_B} 2s \delta(s - (p_A + p_B)^2), \quad (57)$$

$$P_q(s) = n_f g_q^2 \int \frac{d^3 p_A f_q(p_A)}{(2\pi)^3 2E_A} \frac{d^3 p_B f_{\bar{q}}(p_B)}{(2\pi)^3 2E_B} 2s \delta(s - (p_A + p_B)^2); \quad (58)$$

where  $P_q$  includes both  $u, d$  collisions in the factor  $n_f$  in an incoherent way, and hence  $g_q = 2 \cdot 3$ . For gluons we have  $g_g = 2 \cdot 8$ . Assuming that the particle distributions depend only on the magnitude of the momentum, and using

$$\delta(s - (p_A + p_B)^2) = \frac{1}{2p_A p_B} \delta\left(\cos\theta - 1 + \frac{s}{2p_A p_B}\right), \quad (59)$$

we can carry out the two angular integrals to obtain:

$$P_g = \frac{4}{\pi^4} s \int_0^\infty dp_A \int_0^\infty dp_B \Theta(4p_A p_B - s) f_g(p_A) f_g(p_B), \quad (60)$$

$$P_q = \frac{9}{4\pi^4} s \int_0^\infty dp_A \int_0^\infty dp_B \Theta(4p_A p_B - s) f_q(p_A) f_{\bar{q}}(p_B). \quad (61)$$

The step function  $\Theta$  arises because of the limits on the value of  $\cos\theta$  in Eq. (59). To proceed, we assume thermal Bose and Fermi distribution for the particle distributions in the fireball rest frame. Possible  $\vec{x}$ -dependence is implicitly contained in  $T$  and  $\mu_q$ :

$$f_g(p) = \frac{1}{e^{p/T} - 1}, \quad (62)$$

$$f_q(p) = \frac{1}{e^{(p-\mu_q)/T} + 1}, \quad (63)$$

$$f_{\bar{q}}(p) = \frac{1}{e^{(p+\mu_q)/T} + 1}. \quad (64)$$

The integrals in Eqs. (60, 61) can be carried out analytically, although only for  $\mu_q = 0$  in the latter case. In this limit we have:

$$\begin{aligned} \int_0^\infty dp_A dp_B \frac{\theta(4p_A p_B - s)}{(e^{p_A/T} \mp 1)(e^{p_B/T} \mp 1)} \\ = \sum_{n=1}^\infty (\pm)^n \int_0^\infty \frac{dp_A}{(e^{p_A/T} \mp 1)} \int_{s/4p_B}^\infty dp_A e^{-np_A/T} \\ = \sum_{n,l=1}^\infty (\pm)^{n+l} \frac{T}{n} \int_0^\infty dp_B e^{-l\frac{p_B}{T}} e^{-n\frac{s}{4p_B T}}. \end{aligned} \quad (65)$$

This integral type is well known [69]:

$$\int_0^\infty dx e^{-\beta/4x} e^{-\gamma x} = \sqrt{\beta/\gamma} K_1(\sqrt{\beta\gamma}). \quad (66)$$

We obtain for the gluon case:

$$P_g = \frac{4Ts^{3/2}}{\pi^4} \sum_{l,n=1}^\infty \frac{1}{\sqrt{nl}} K_1\left(\frac{\sqrt{nl}s}{T}\right). \quad (67)$$

Similar expression follows for quark processes when the chemical potentials vanish:

$$P_q|_{\mu_q=0} = \frac{9Ts^{3/2}}{4\pi^4} \sum_{l,n=1}^\infty \frac{(-)^{n+l}}{\sqrt{ln}} K_1\left(\frac{\sqrt{nl}s}{T}\right). \quad (68)$$

The case with  $\mu_q > 0$  is of greater physical interest in the present context of baryon-rich fireballs. In this case only the antiquark distribution Eq. (64) can be expanded in terms of a geometric series for all values of the quark momentum. Keeping the quark Fermi distribution, we obtain an expression containing one (numerical) integration:

$$P_q = \frac{9T}{4\pi^4} s \sum_{l=1}^\infty \frac{(-)^{l+1}}{l\lambda_q^l} \int_0^\infty dp_A \frac{e^{-l\frac{s}{4p_A T}}}{\lambda_q^{-1} e^{p_A/T} + 1}, \quad (69)$$

where  $\lambda_q = e^{\mu_q/T}$  is the quark number fugacity. The remaining integral over  $dp_A$  has to be solved numerically. In Fig. 20 we show the collision distribution functions Eqs. (67, 69) describing the probability that a pair of gluons (thick lines) or a light quark  $q\bar{q}$ -pair (thin lines) collides at a given  $\sqrt{s}$ , for  $T = 260$  (dotted) and 320 MeV (dashed), which we expect to be



appropriate limits on initial fireball temperatures for the S–W and Pb–Pb collisions. For quarks we have taken  $\lambda_q = 1.5$ , which properly accounts for the baryon abundance in the fireball, see table 2. We also show  $T = 500$  MeV (solid lines), with  $\lambda_q = 1$ , which choice, as we hope, is exploring the future conditions at RHIC/LHC.

The thermal differential production rates  $dA_i/ds$ , Eq. (56) for strangeness are shown in Fig. 21. We note that for the gluon fusion to strangeness processes the peak of the production occurs at relatively low energies  $\sqrt{s} \simeq 0.5$  GeV, and it is slightly more peaked and higher in energy than seen for quark pair processes. The dominance of the gluon channel in favor production arises primarily from the greater statistical probability to collide two gluons in plasma at a given  $\sqrt{s}$ , as compared to the probability of  $q + \bar{q}$  collisions, see Fig. 20 as well as from contributions at  $\sqrt{s}$  away from production threshold.

The differential production rate can be easily integrated, and we show the result in Fig. 22. These results depend, of course, on the choice of the value of the strange quark mass, assumed here to be 160 MeV. The production rates in Figs. 22 and 30, when inserted into Eq. (50), provide the relaxation time constants  $\tau_s$ ,  $\tau_c$ . In Fig. 23 we show strangeness relaxation constant using the same conventions and parameters as in Figs. 22. The dominance of gluon fusion over quark fusion for strangeness production process can be now more easily appreciated, and we note that as function of temperature in the interesting interval the relaxation time drops by an order of magnitude. This in particular explains the phenomenon, that when the QGP fireball cools, the abundance of strangeness freezes out, i.e., strangeness once produced is not reannihilated significantly.

We wish to record here that the strangeness phase space saturation seen in SPS-relativistic heavy ion collision experiments cannot be a simple result of totally conventional physics. In the dense state of highly excited confined HG fireball, there are many different strangeness production channels and a full discussion is beyond the scope of this presentation. The key results were described in detail elsewhere [7, 70]: in a gas consisting of particle states with normal properties, strangeness saturation time scales are very much longer, as is shown in Fig. 24, where the approach to equilibrium abundance as function of time takes nearly 100 fm/c. Thus if this was the actual situation, then the strange particle abundance would be largely result of pre-thermal collisions, and thus could be easily described by folding of a geometric microscopic collision model with the experimental N–N results. There is considerable ongoing effort to simulate, using microscopic models,

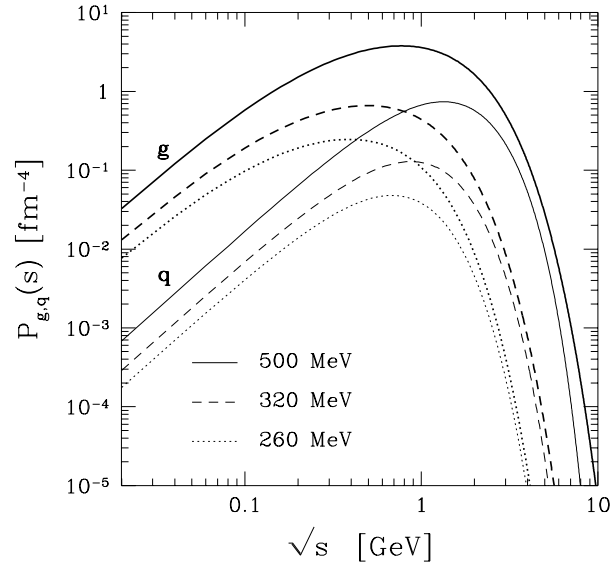


Figure 20: The collision distribution functions for gluons (thick lines) and quarks (thin lines) as function  $\sqrt{s}$ . Computed for temperature  $T = 260$  MeV (dotted lines) and  $T = 320$  MeV (dashed lines). For quarks  $\lambda_q = 1.5$  was used in these two cases. The solid lines show the RHIC domain,  $T = 500$  MeV and  $\lambda_q = 1$ .

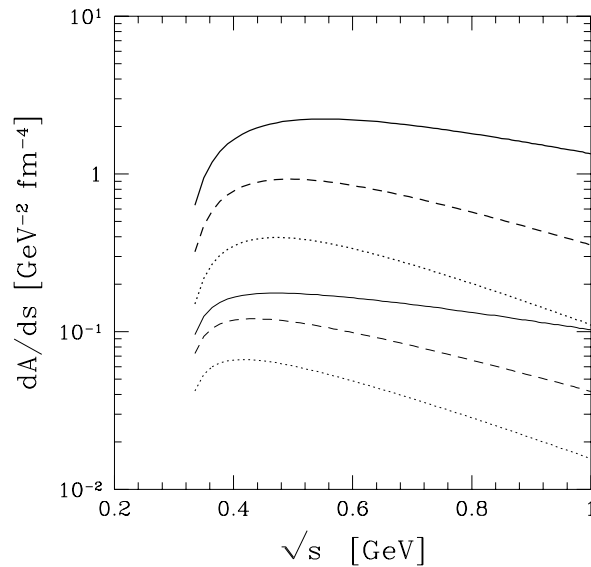


Figure 21: Differential thermal strangeness production rate  $dA_s/ds = P(s)\sigma(s)$ , with  $T = 260$  (dotted) and  $320$  MeV (dashed) and  $m_s = 160$  MeV, for gluons (thick) and  $q\bar{q}$  pairs (thin), with  $\lambda_q = 1.5$ ,  $\alpha_s = 0.6$ ; and for  $T = 500$  MeV with  $\lambda_q = 1$  and  $\alpha_s = 0.4$  (solid line).

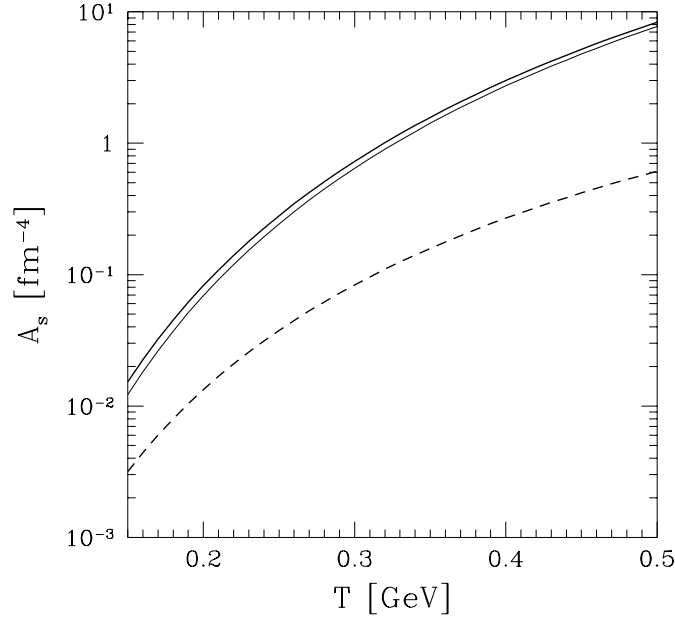


Figure 22: Thermal strangeness production rates  $A_s$  in QGP: total (thick solid line), gluons only (thin solid line), and light quarks only (dashed line), calculated for  $\lambda_q = 1.5$ ,  $m_s = 160$  MeV,  $\alpha_s = 0.6$  as function of temperature.

this initial phase of nuclear collisions, and while these efforts can produce appropriate yields of some particles, the overall reaction picture [45], in particular considering the multistrange baryons and antibaryons is so far not satisfactory, supporting at least the claim that strangeness enhancement requires some new physics phenomenon, if not QGP as we are arguing here. Models that include microscopic deconfinement, such as the dual parton model [71], but which do not assume thermalization, require the introduction of mechanisms to fit the multistrange particle yields at central rapidities.

### 6.3 Running $\alpha_s$ and flavor production

One of the key, and still arbitrary parameters we used above is the choice we have made  $\alpha_s = 0.6$ . While the value seems reasonable, others may prefer a smaller value, and just choosing  $\alpha_s = 0.3$  would lengthen the relaxation time of strangeness  $\tau_s \propto \alpha_s^{-2}$  by factor 4, from 2 fm to 8 fm and thus beyond the expected lifespan of the QGP fireball. We exploit here the recent precise determination of  $\alpha_s(M_Z)$  [72, 73, 74] which allow to eliminate assumptions about  $\alpha_s$  from our calculations.

Running QCD methods can be used [75] to obtain the proper value of

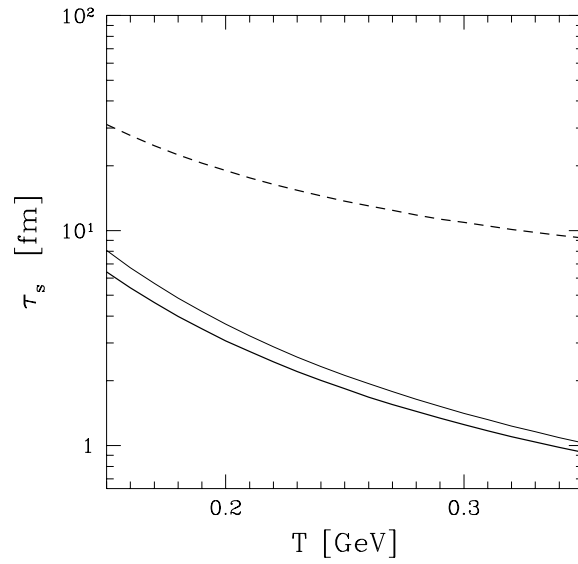


Figure 23: Thermal strangeness relaxation constants in QGP: same conventions and parameters as in Fig. 22.

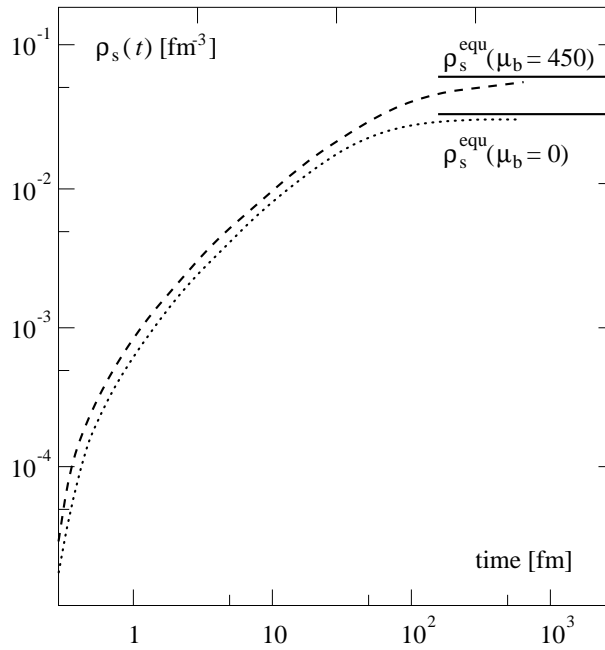


Figure 24: Thermal strangeness production as function of time in a confined hadron gas at  $T = 160$  MeV. Results for two values of baryochemical potential ( $\mu_B = 0$  and 450 MeV are shown. After Koch et al. [7].

$\alpha_s$  allowing to reevaluate strangeness production in a thermal QGP fireball and to justify the choice of the coupling constant we have made. Moreover, since the running QCD resummation is performed, we are able to account for a large class of contributing diagrams. However, the knowledge of the strange quark mass remains limited and will need further refinement, even allowing for the running-QCD effects considered here. Another remaining shortcoming is that up to day there has not been a study of the importance of the final state (radiative gluon) or initial state three body effects in the entrance channel. Such odd- $\alpha_s$  infrared unstable processes have environment induced infrared cut-off (Landau-Pomeranchuk effect) which in dense matter eliminates modes that are softer than the collision frequency.

The running coupling constant  $\alpha_s$  and quark mass satisfy the QCD renormalization group equations<sup>4</sup>:

$$\mu \frac{\partial \alpha_s}{\partial \mu} = \beta(\alpha_s(\mu)), \tag{70}$$

$$\mu \frac{\partial m}{\partial \mu} = -m \gamma_m(\alpha_s(\mu)). \tag{71}$$

These functions  $\beta$  and  $\gamma_m$  are today known for the SU(3)-gauge theory with  $n_f$  fermions, but only in a perturbative power expansion in  $\alpha_s$ ; three leading terms are known for  $\beta$  and two for the  $\gamma_m$  [76]:

$$\beta^{\text{pert}} = -\alpha_s^2 [ b_0 + b_1 \alpha_s + b_2 \alpha_s^2 + \dots ] , \tag{72}$$

$$\gamma_m^{\text{pert}} = \alpha_s [ c_0 + c_1 \alpha_s + \dots ] , \tag{73}$$

with

$$b_0 = \frac{1}{2\pi} \left( 11 - \frac{2}{3} n_f \right) , \quad b_1 = \frac{1}{4\pi^2} \left( 51 - \frac{19}{3} n_f \right) , \tag{74}$$

$$c_0 = \frac{2}{\pi} , \quad c_1 = \frac{1}{12\pi^2} \left( 101 - \frac{10}{3} n_f \right) . \tag{75}$$

The  $b_2$ -coefficient in Eq. (72) is renormalization scheme dependent, and is known, e.g., in the modified minimum subtraction dimensional renormalization ( $\overline{MS}$ ) scheme:

$$b_2^{\text{MS}} = \frac{1}{64\pi^3} \left( 2857 - \frac{5033}{9} n_f + \frac{325}{27} n_f^2 \right) . \tag{76}$$

---

<sup>4</sup>Caution should be exercised not to confuse the chemical potentials with the variable  $\mu$  used here without and index, which denotes the energy scale of running QCD variables.

Since there is no renormalization scheme dependence in the full non perturbative QCD process, cancelation between the different renormalization group terms must occur. The number  $n_f$  of fermions that can be excited, depends on the energy scale  $\mu$ . The form appropriate for the terms linear in  $n_f$  is:

$$n_f(\mu) = 2 + \sum_{i=s,c,b,t} \sqrt{1 - \frac{4m_i^2}{\mu^2}} \left(1 + \frac{2m_i^2}{\mu}\right) \Theta(\mu - 2m_i), \quad (77)$$

with  $m_s = 0.16$  GeV,  $m_c = 1.5$  GeV,  $m_b = 4.8$  GeV. There is very minimal impact of the running of the masses in Eq. (77) on the final result. The bottom mass uncertainty has the greatest impact, since small perturbation of the  $\beta$ -function at  $\mu \simeq 10$  GeV is enhanced strongly when the error propagates to  $\mu = 1$  GeV or  $\mu = 100$  GeV, which are the values being connected to each other.

Even if the perturbative expansion is leading to an adequate theoretical description at small values of  $\alpha_s$ , the extrapolated value of  $\alpha_s$ , as the scale  $\mu$  decreases, can approach and exceed unity, where use of perturbative expansion is not easily justified, and thus effort has to be made to incorporate all known terms in the perturbative expansion of the  $\beta$ -function. Recent work suggests that Pade approximants in QCD expression could improve the precision and enlarge the circle of convergence of the perturbative expansion [77]. A suitable Pade-approximant for the  $\beta$ -function is:

$$\beta \rightarrow \beta^{(0,2)} \equiv \alpha_s^2 b_0 \frac{1}{1 - u\alpha_s + v\alpha_s^2} = \alpha_s^2 b_0 \frac{b_0}{b_0 - b_1\alpha_s + (b_1^2/b_0 - b_2)\alpha_s^2}. \quad (78)$$

The integration of the renormalization equations is facilitated by this modification since it turns out that the numerical solutions are stabilized in that way.

Eq. (70) is numerically integrated beginning with initial value of  $\alpha_s(M_Z)$ , using the perturbative series (72) for the  $\beta$ -function (dotted lines in Fig. 25) or its (0,2) approximant Eq. (78) (full lines). Thick lines correspond to  $\alpha_s(M_Z) = 0.102$ . This value of  $\alpha_s$  is consistent with the precise botonium sum rule result [73]  $\alpha_s(1\text{GeV}) = 0.336 \pm 0.011$ , this extremely precise point is shown in Fig. 25. We recall that the well known  $Z$  line shape LEP data fit leads to  $\alpha_s(M_Z) = 0.123 \pm 0.006$ . However, in this fit there is disagreement between the observed and predicted properties of the  $Z \rightarrow b\bar{b}$  vertex. If one proceeds with line shape fit excluding this branching ratio [72], one obtains  $\alpha_s(M_Z) = 0.101 \pm 0.008$ . The thin solid lines in Fig. 25 are for the initial value  $\alpha_s(M_Z) = 0.115$ , in agreement with some other experimental results [76] also shown in Fig. 25, including some recent HERA data [78], as

well as the recent measurement of the structure of hadronic events by the L3 detector at LEP-II [79]. The sum-rule study of Ellis et al. [74] leads to the point at  $\mu = 1.7$  GeV appearing in the middle between thin and thick curves in the top section of Fig. 25.

The middle section of Fig. 25 shows what the running of  $\alpha_s$  implies for the value  $\Lambda_0$  which is sometimes used to characterize the variation of  $\alpha_s$  based on a first order result. Here  $\Lambda_0(\mu)$  is defined by the implicit equation:

$$\alpha_s(\mu) \equiv \frac{2b_0^{-1}(n_f)}{\ln(\mu/\Lambda_0(\mu))^2}. \quad (79)$$

We see that  $\Lambda_0(1 \text{ GeV}) = 240 \pm 100$  MeV, assuming that the solid lines provide a valid upper and lower limits on  $\alpha_s$ . However, the variation of  $\Lambda_0(\mu)$  is significant for  $\mu < 3$  GeV, questioning the use of first order expressions, seen frequently in literature.

With  $\alpha_s(\mu)$  from the solutions described above Eqs. (71, 73) allow to explore the quark masses. Because Eq. (71) is linear in  $m$ , it is possible to determine the universal multiplicative quark mass scale factor

$$m_r = m(\mu)/m(\mu_0). \quad (80)$$

Since  $\alpha_s$  refers to the scale of  $\mu_0 = M_Z$ , it is a convenient reference point also for quark masses. As seen in the bottom portion of Fig. 25, the change in the quark mass factor is highly relevant, since it is driven by the rapidly changing  $\alpha_s$  near to  $\mu \simeq 1$  GeV. For each of the two different functional dependences  $\alpha_s(\mu)$  we obtain a different function  $m_r$ . Note that the difference between (0,2) approximant result (solid lines) and perturbative expansion (dotted lines) in Fig. 25 is indeed, at fixed  $\mu \simeq 1$  GeV, very large, however it remains insignificant since it amounts to a slight 'horizontal' shift of  $\alpha_s$  and  $m_r$  as function of  $\mu$ .

Like for  $\alpha_s$ , the uncertainty range in  $m_r$  due to the error in the initial value  $\alpha_s(M_Z)$  is considerable. Some of this sensitivity will disappear when we consider the cross sections, and in particular their thermal average weighted with particle distribution. Furthermore, the strangeness production cross section is subject to an implicit infrared stabilization: below  $\sqrt{s} = 1$  GeV the strange quark mass increases rapidly and the threshold mass  $m_s^{\text{th}}$  for the pair production, defined by the solution of the equation

$$m_s^{\text{th}}/m_s(M_Z) = m_r(2m_s^{\text{th}}), \quad (81)$$

is considerably greater than  $m_s(1 \text{ GeV})$ . For example, for  $m_s(M_Z) = 90$  MeV:  $m_s(1 \text{ GeV}) \simeq 160$  and 215 MeV for the two choices of  $\alpha_s(M_Z)$ , within the standard range  $100 < m_s(1 \text{ GeV}) < 300$  MeV; the corresponding threshold values are 470 MeV for the smaller  $\alpha_s$  option (thick lines) and 740 MeV

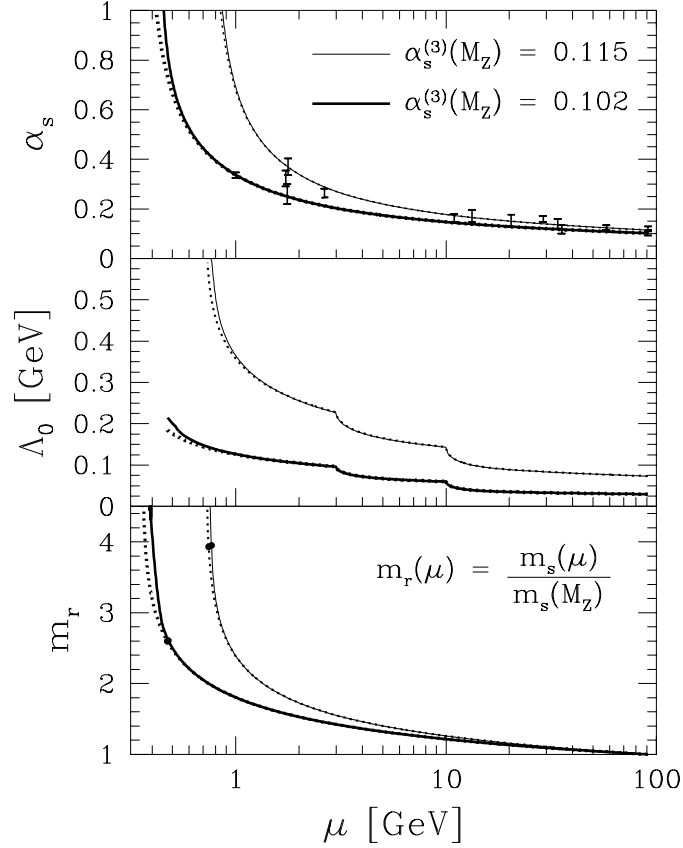


Figure 25:  $\alpha_s(\mu)$ , the  $\Lambda$ -parameter  $\Lambda_0$  and  $m_r(\mu) = m(\mu)/m(M_Z)$  as function of energy scale  $\mu$ . Thick lines correspond to initial value  $\alpha_s(M_Z) = 0.102$ , thin lines are for the initial value  $\alpha_s(M_Z) = 0.115$ . Dotted lines are results using the perturbative expansion for the renormalization group functions, full lines are obtained using (0,2) Padé approximant of the  $\beta$  function. Experimental results for  $\alpha_s$  selected from references [72, 73, 74, 76, 78]. In bottom portion the dots indicate the pair production thresholds for  $m_s(M_Z) = 90$  MeV.

for the higher option (thin line). Both values are indicated by the black dots in Fig. 25.

We note in passing that the same effect occurs for charm quark mass: it is running equally rapidly and we find that an appropriate value at  $\mu = M_Z$  would be 700 MeV, as this choice assures given  $\alpha_s(\mu)$  that  $m_c(1 \text{ GeV}) \simeq 1.5 \text{ GeV}$ . The drop in  $m_c$  at the production threshold,  $\mu \simeq 2.5 \text{ GeV}$  has important ramifications for the rate of thermal charm production.

We can now insert into the generic production cross sections, Eqs. (42, 43) the running QCD parameters, identifying  $\mu \rightarrow \sqrt{s}$ . The resulting



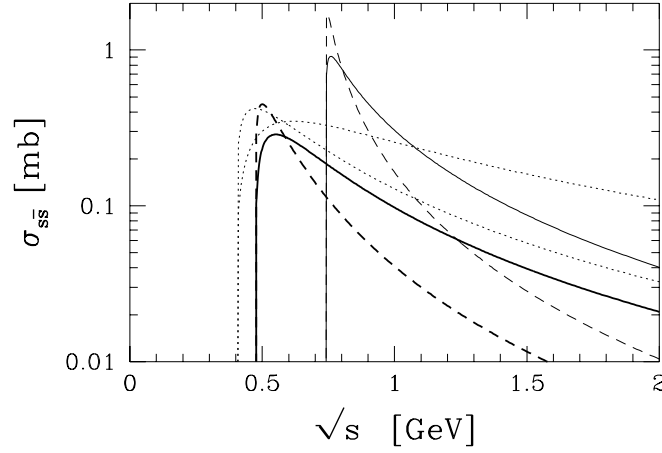


Figure 26: QCD strangeness production cross sections obtained for running  $\alpha_s(\sqrt{s})$  and  $m_s(\sqrt{s})$ . Thick solid line is for the small  $\alpha_s$  option, thin line for the other  $\alpha_s$ -option considered in Fig. 25. Solid lines  $gg \rightarrow s\bar{s}$ ; dashed lines  $q\bar{q} \rightarrow s\bar{s}$ . Dotted lines: results for fixed  $\alpha_s = 0.6$  and  $m_s = 200$  MeV.

cross sections are then a sum of all two particle fusion contributions to strangeness production with two particles in the final state. In Fig. 26, the strangeness production cross sections are shown with  $m_s(M_Z) = 90$  MeV. For the two choices of the running coupling constant considered in Fig. 25 the cross sections for the processes  $gg \rightarrow s\bar{s}$  (solid lines, upper dotted line) and  $q\bar{q} \rightarrow s\bar{s}$  (dashed lines, lower dotted line) are shown. Dotted are cross sections computed with fixed  $\alpha_s = 0.6$  and  $m_s = 200$  MeV cross sections, shown here for comparison. We note that the glue based flavor production dominates at high  $\sqrt{s}$ , while near threshold the cross sections due to light quark heavy flavor production dominate. We note the different thresholds for the two values of  $\alpha_s(\mu)$  used. It is apparent that the cross sections are ‘squeezed’ away from small  $\sqrt{s}$  as the value of  $\alpha_s$  increases, such that the energy integrated cross sections ( $\simeq$  rates) are little changed.

We note that these results justify to considerable extent the use of the perturbative approximation with fixed  $\alpha_s = 0.6$  in the study of QGP based strangeness production processes within the range  $150 < T < 300$  MeV; not only is this value  $\alpha_s = 0.6$  in the middle of the range spanned in the Fig. 25, but moreover, we see that the inelastic (production) cross sections shown in Fig. 26 have similar integrated strength. However the choice of the strange quark mass impacts considerably the result we find, and thus there is systematic uncertainty related to the relatively large range of permissible  $m_s(\mu)$ .

From this point on, given the improved cross sections, the calculation

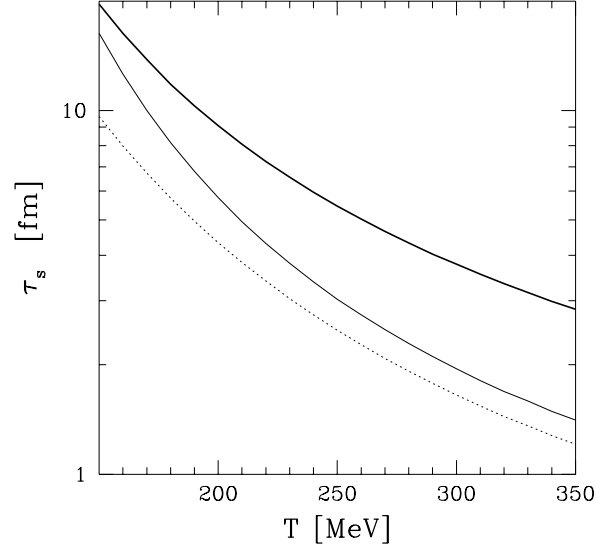


Figure 27: QGP strangeness relaxation time obtained from the running  $\alpha_s$ -cross sections shown in Fig. 26. Thick solid line is for the small  $\alpha_s$  option, thin line for the other  $\alpha_s$ -option considered in Fig. 25. Dotted: results for fixed  $\alpha_s = 0.6$  and  $m_s = 200$  MeV.

of thermal relaxation time constant of strangeness follows the pattern we described in section 6, Eq. (54). The result, the relaxation time constants  $\tau_s$  is shown in Fig. 27 for the two different choices of the strong coupling constant considered here. Dotted line shows, for comparison, the result obtained using the fixed values  $\alpha_s = 0.6$  and  $m_s = 200$  MeV.  $\tau_s$  is defined as before in Eq. (50):

$$\tau_s \equiv \frac{1}{2} \frac{\rho_s^\infty}{(A_{gg} + A_{qq} + \dots)}, \quad (82)$$

but the equilibrium density which the produced particles ‘chase’ require now a second thought, as it depends on the (strange) quark mass, and the question is: at which scale  $\mu$  is  $m$  to be considered. Recall that the equilibrium density is obtained in transport formulation of the evolving particle distributions in consequence of particle-particle collisions. It is thus the characteristic energy of these interactions which determines the energy scale which enters the determination of the mass in the density  $\rho_s^\infty$ . Since the strangeness production phenomena occur at maximum attainable temperature  $T \geq 260$  MeV, the range of values relevant in this paper is  $m_s \simeq 160$ –200 MeV.  $m_s = 200$  MeV leads to the result shown in Fig. 27. The difference between the dotted line and the thin (or even

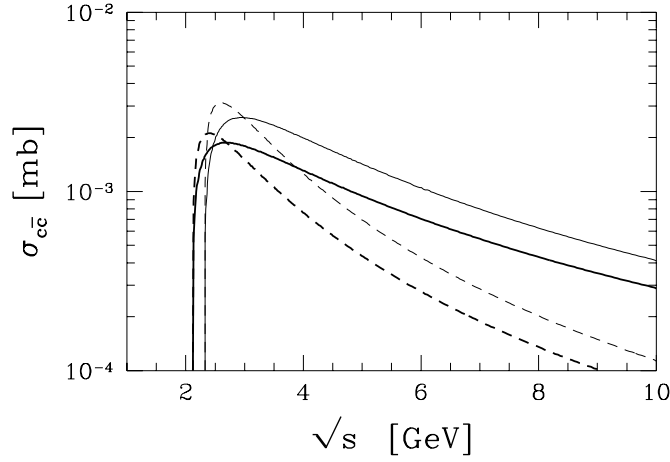


Figure 28: Charm production cross sections for the two running  $\alpha_s$  (thick and thin solid lines) and running charmed mass with  $m_c(M_Z) = 0.7$  MeV; dashed the light quark process, solid lines,  $gg \rightarrow c\bar{c}$ .

thick line, provided that care is taken to choose appropriate value of  $\alpha_s$ ) is barely significant. Thus, the gluon fusion motivated analytical expression (see Eq. (96) below) provides a valid description of the relaxation times in the range of temperatures explored in Fig. 27, in particular view of the remaining uncertainties about the radiative (odd- $\alpha_s$ ) diagrams, the initial value  $\alpha_s(M_Z)$ , and the strange quark mass.

#### 6.4 Thermal charm production

We note that since the mean energy per particle is approximately  $3T$  in the relativistic gas, rather high  $\sqrt{s}$  are reached, allowing in principle the thermal formation of charmed quark pairs. We exploit now the above developments to obtain these results.

In Fig. 28 we show the gluon and quark-pair fusion charm production cross sections, computed for the two running  $\alpha_s(M_Z) = 0.102 = 0.115$  (thick and thin solid lines) and running charmed mass with  $m_c(M_Z) = 0.7$  MeV; dashed lines depict the light quark fusion process, Noteworthy is the smallness of this cross section, due to the relatively large value of  $\sqrt{s}$  required, given that  $\sigma \propto 1/s$ . However, we will show that one cannot neglect the thermal charm production in LHC or even RHIC environments, where the charm production can lead in the end to notable phase space saturation at freeze-out.

The resulting thermal differential production rates  $dA_i/ds$  for charm, Eq. (56), are shown in Fig. 29. We note that the thermal charm production peaks at  $\sqrt{s} \simeq 2.5$  GeV, near to the running mass production threshold.

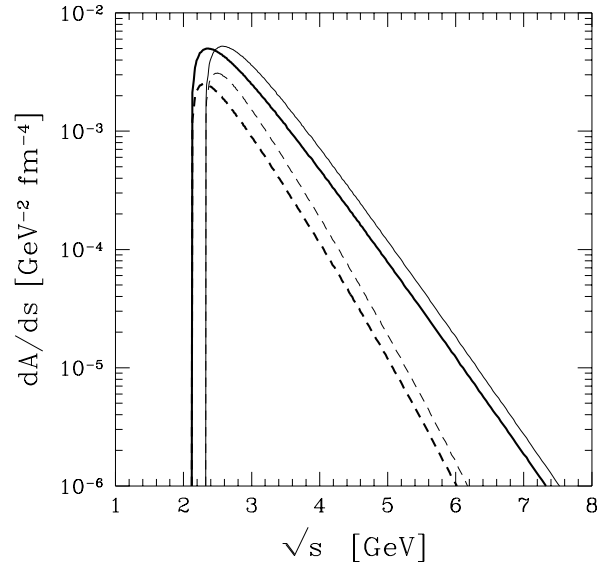


Figure 29: Differential thermal charm production rate  $dA_c/ds = P(s)\sigma(s)$ , with  $T = 500$  MeV, with  $\lambda_q = 1$  for gluons (solid lines) and  $q\bar{q} \rightarrow c\bar{c}$  (dashed, includes three interacting flavors), for the two running  $\alpha_s$  (thick and thin solid lines) and running charmed mass  $m_c$ .

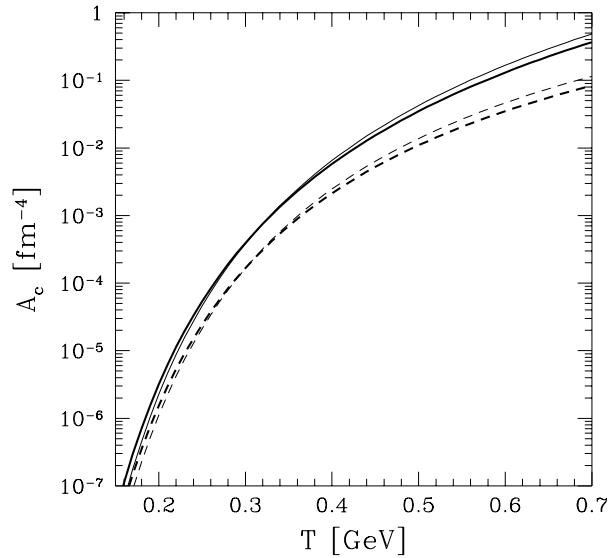


Figure 30: Thermal charm production rates  $A_c$  as function of temperature in QGP: total (solid line), and light quarks only (dashed line), calculated for two cases of running- $\alpha_s$ ,  $m_c$ .

The differential production rate can be easily integrated, and we show the result in Fig. 30. We see that the charm production rate changes by 6 orders of magnitude as the temperature varies between 200 and 700 MeV. This sensitivity on the initial temperature, while understandable due to the fact that  $m/T > 1$ , also implies that since the charm production rate is not vanishingly small, we may have found an interesting probe of the primordial high temperature phase. This was also noted in a case study performed by Levai et al. [80]. Note that the gluon dominance of the production rate is not as pronounced for charm as it is for strangeness because charm formation occurs near to the threshold, where the quark fusion cross section dominates. Only for  $T \geq 400$  MeV we find that the glue fusion dominates the thermal charm production clearly. For charm there is the possibility that the thermal production is overwhelmed by the direct production based on high energy parton interactions. Calculations show [81] that per LHC event there may be a few directly produced charm quark pairs. However, we have a differential production rate for an initial state with chemically equilibrated gluons at  $T \simeq 450$  MeV,  $A_s \simeq 10^2 \text{ fm}^{-4}$ , see Fig. 30, which implies that we should expect up to 20 thermal charmed quark pairs per such event at central rapidity, which yield is clearly dominating the reported direct production rate. Consequently, we continue below to evaluate in detail the evolution of thermal charm yield, which may dominate the production rate and in particular lead to rather surprising features in final particle yields, should the initial plasma temperature be sufficiently large. Moreover, the rates we find for temperatures near 250 MeV, seem to be still within the realm of the observable.

In Fig. 31 we show the charm relaxation constant, see Eq. (50), using the same conventions and parameters as in Fig. 30, and using  $m_c \simeq 1.5$  GeV in order to establish the reference density for the approach to equilibrium. Actually, this running value is temperature dependent, and will be slightly smaller at higher temperatures, since the average interaction energy is greater. We will return to discuss this intricate variation at another occasion. What it implies is that at high temperatures we are ‘chasing’ with the thermal rate a somewhat higher equilibrium density and thus the computed relaxation time underestimates slightly the correct result.

## 7 Evolution of heavy quark Observables

### 7.1 Flow model

We now can proceed to explore two generic (strangeness) observables as function of the impact parameter (baryon content) and collision energy:

- Specific (with respect to baryon number  $B$ ) strangeness yield  $N_s/B$

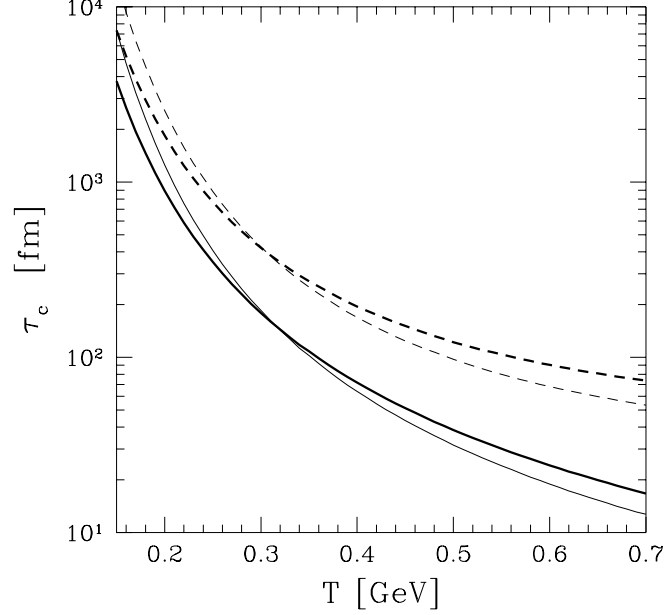


Figure 31: Thermal charm relaxation constant in QGP, calculated for  $\alpha_s$  running.: same conventions and parameters as in Fig. 30.

*Once produced strangeness escapes, bound in diverse hadrons, from the evolving fireball and hence the total abundance observed is characteristic for the initial extreme conditions;*

- Phase space occupancy  $\gamma_s$

*Strangeness freeze-out conditions at particle hadronization time  $t_f$ , given the initially produced abundance, determine the final state observable phase space occupancy of strangeness  $\gamma_s(t_f)$ .*

To pursue this a more specific picture of the temporal evolution is needed: in the earlier discussion in section 4 we have considered the chemical cooling [53] due to the strangeness production. It is a rather complicated matter to account simultaneously for both the chemical cooling, and the flow cooling arising from volume expansion. We shall concentrate here on the flow cooling which dominates the evolution once strangeness reaches chemical equilibrium. We therefore denote all initial values by the subscript ‘in’ in order to distinguish the here proposed schematic model from the earlier discussion of chemical cooling which is important in the early evolution stages.

In first approximation, the particle density in the fireball as taken to being constant and the sharp surface of the volume comprising the dense

matter is allowed to expand in all space directions at most and probably near to maximal sound velocity  $v_c \lesssim c/\sqrt{3}$ . This value is consistent with the hydrodynamic flow studies and also leads to a Doppler blue-shift factor  $F_f = \sqrt{(1+v_c)/(1-v_c)} \lesssim 1.93$  of the freeze-out temperature  $T_f \simeq 140$  MeV, which is consistent with the apparent spectral temperatures, obtained from the initial temperature, see table 2. Onto this collective radial motion there will be superposed additional longitudinal collective motion related to the remainder of the original longitudinal momentum of the colliding particles. Furthermore, the volume and temperature temporal evolution constrained by the adiabatic evolution condition which for massless particles has the form:

$$V \cdot T^3 = \text{Const.} \quad (83)$$

The fireball radius grows according to

$$R = R_{\text{in}} + \frac{1}{\sqrt{3}}(t - t_{\text{in}}), \quad (84)$$

and hence from the adiabatic expansion constraint Eq.(83) we obtain the time dependence of temperature:

$$T = \frac{T_{\text{in}}}{1 + \frac{t-t_{\text{in}}}{\sqrt{3}R_{\text{in}}}}. \quad (85)$$

A set of initial conditions for the SPS experiments follows from the kinematic constraints [18], see table 2, consistent with global event structure, and the hadronic freeze-out condition seen in HBT experiments is [32,33]:

$$\begin{aligned} T_{\text{in}} &= 320 \text{ MeV}; \quad R_{\text{in}} = 5.6 \text{ fm}; \quad t_{\text{in}} = 1 \text{ fm}/c; \quad \lambda_q = 1.6; \quad \text{for Pb-Pb,} \\ T_{\text{in}} &= 280 \text{ MeV}; \quad R_{\text{in}} = 4.7 \text{ fm}; \quad t_{\text{in}} = 1 \text{ fm}/c; \quad \lambda_q = 1.5; \quad \text{for S-Pb/W.} \end{aligned}$$

Here the radius  $R_{\text{in}}$  has been determined such that for the QGP equations of state we employ the baryon number content in the fireball is 380 (Pb-Pb case) and 120 (S-Pb/W case) respectively, corresponding to zero impact parameter collisions. The energy/baryon content at given projectile energy is computed assuming that same stopping governs energy and baryon number which we take for the current discussion to be 50% for S-Pb/W and 100% for Pb-Pb. Also, we take  $\gamma_s(t = t_{\text{in}}) = 0.15$  as the initial strangeness abundance after 1 fm/c. The chosen values of  $\lambda_q$  are of minimal importance, as they enter marginally into the quark-fusion rate, which is a minor contribution to the strangeness production rate. However,  $\lambda_q$  has indirect importance as it determines the initial fireball size for given  $B$  and impacts greatly the strange particle (baryon/antibaryon) ratios. The most important parameter, which follows from the theoretical model developed for the

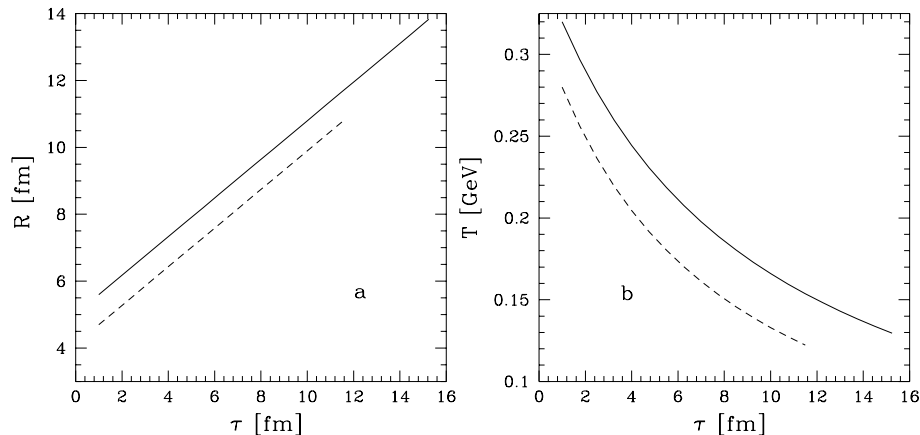


Figure 32: Assumed (see Eqs. (84, 85)) temporal evolution of **a** the radius parameter  $R(t)$  and **b** temperature  $T$  of the thermal fireball formed in Pb–Pb collisions (solid lines) and S–W/Pb collisions (dashed lines).

collision, is the temperature  $T_{\text{in}}$ . We use in the calculations  $\gamma_s(t_{\text{in}}) = 0.15$  as the initial strangeness occupancy factor after 1 fm/c [59].

From Eqs. (84, 85) it follows that the temperature drops to the commonly accepted phase transition value  $T_f \simeq 140$  MeV [3] at  $t = 9.2$  and  $13.5$  fm/c for S–W/Pb and Pb–Pb systems, respectively. At these instants the size of the fireball has reached 9.4 and 12.8 fm, respectively.

Note that some of the results shown below here were obtained with QCD parameters,  $\alpha_s = 0.6$  and  $m_s = 160$  MeV [18], other were computed with running  $\alpha_s$  with initial values as discussed, see Fig. 25 [75]. While these results are nearly consistent with each other, the remaining differences illustrate some of the uncertainties in our theoretical modeling of the heavy flavor production.

## 7.2 Dynamical description of observables in the fireball

As we have discussed in section 4.4 it is rather straightforward to extract from the strange antibaryon experimental particle yields the value of strangeness phase space occupancy  $\gamma_s(t = t_f)$ , since the hadronization value of  $\gamma_s(t_f)$  governs the ratios of particles with different strangeness content. We recall that since the thermal equilibrium is by hypothesis established within a considerably shorter time scale than the (absolute) heavy flavor chemical equilibration, we can characterize the saturation of the phase space by an



average over the momentum distribution, see also Eq. (49):

$$\gamma_{s,c}(t) \equiv \frac{\int d^3p d^3x n_{s,c}(\vec{p}, \vec{x}; t)}{\int d^3p d^3x n_{s,c}^\infty(\vec{p}, \vec{x})}, \quad (86)$$

where  $n_{s,c}$  is the sum over all heavy flavor containing particle densities, and should multistrange/charmed objects be present, this sum contains the associated weight.  $n_{s,c}^\infty$  is the same, but for the equilibrium particle densities. In QGP deconfined state, of course we have just the free quarks. When we assume that the fireball is homogeneous in  $T$  and  $\lambda_q$  we can write:

$$n_s(\vec{p}; t) = \gamma_s n_s^\infty(\vec{p}; T, \mu_s). \quad (87)$$

Since  $\tau_s$  is just of the magnitude of the life span of the deconfined state, see Fig. 23, strangeness will be close to fully saturate the final state phase-space in the QGP fireball. However, this accidental similarity of the life span of the fireball and the relaxation time of strangeness implies that changes in the collision conditions should lead to measurable changes of  $\gamma_s$ . This would be a highly desirable situation, allowing a test of the theoretical predictions. It can be expected that in the near future  $\gamma_s$  will be studied varying a number of parameters of the collision, such as the volume occupied by the fireball (varying size of the colliding nuclei and impact parameter), the trigger condition (e.g., the inelasticity), the energy of colliding nuclei when searching for the threshold energy of abundant strangeness formation. We thus develop in this section a more precise understanding of the time evolution of the observed value of  $\gamma_s$ , as function of the collision parameters. This variable comprises as the dynamic element the specific strangeness yield, indeed we can easily see that: the ratio of the observed phase space occupancy  $\gamma_s(t_f)$  to the specific yield  $N_s/B$  is *independent of the initial conditions and only dependent on the freeze-out:*

$$\frac{\gamma_s(t_f)}{N_s/B} = \frac{B}{N_s^\infty}, \quad (88)$$

where  $N_s^\infty = \rho_s^\infty(T_f)V_f$  is the equilibrium abundance of strangeness in the fireball at dissociation/freeze-out. We thus see that if we can interpret both observables  $\gamma_s(t_f)$  and  $N_s/B$  successfully, we have in all likelihood obtained a valid model both of the initial and freeze-out conditions.

Similarly, as alluded to above in section 6.4, the thermal charm production is sensitive to the initial temperature, but clearly the production of charmed particles will not saturate the initially available phase space. However, it is interesting to see what values of  $\gamma_c$  would be found in the final state, since the equilibrium density of charm at hadronization is very low.

Also here we need to consider in some more detail the temporal evolution with the plasma expansion of the off-equilibrium parameter  $\gamma_c$ .

The general expression for strangeness production is given by Eq. (47). Taking the particle density everywhere in the fireball as constant, we have:

$$\frac{1}{V} \frac{dN_s(t)}{dt} = A [1 - \gamma_s^2] . \quad (89)$$

The  $\gamma_s^2$  term arises when the back reaction, e.g.,  $s\bar{s} \rightarrow gg$  is considered in the Boltzmann approximation, and the unsaturated [53] thermally equilibrated quantum Bose/Fermi phase space distributions are expanded:

$$n_i^{\text{B,F}} = \frac{1}{\gamma_i^{-1} \lambda_i e^{\beta \epsilon_i} \mp 1} \rightarrow \gamma_i \lambda_i^{-1} e^{-\beta \epsilon_i} . \quad (90)$$

Evaluation of relaxation constants with complete quantum phase space [82] has not revealed any significant effects, thus Boltzmann terms provide here a very good approximation. Recall that the subtle difference between  $\gamma$  and  $\lambda$  is that while the latter is conjugated between particles and antiparticles, see Eq. (9),  $\gamma$  is the same for particles and antiparticles. Equivalently, one can introduce different chemical potentials for particles and antiparticles, as was the case in Ref. [82]

It is common practice to illustrate the impact of volume expansion dilution to write  $N = \rho V$  which when inserted on the left hand side of Eq. (89) leads to:

$$\frac{d\rho_s}{dt} + \rho_s \frac{1}{V} \frac{dV}{dt} = A [1 - \gamma_s^2] . \quad (91)$$

The second term on the left hand side is referred to as the volume dilution term.

In order to obtain a dilution equation for  $\gamma_s$ , let us instead proceed, using in Eq. (89) the definition of  $\gamma_s$  in the form:

$$N_s(t) = \gamma_s(t) N_s^\infty(T(t)) . \quad (92)$$

Note that when dividing Eq. (92) by  $V(t)$  we recover our earlier definitions of  $\gamma_s$ , see Eqs. (49, 87).

Inserting Eq. (92) into Eq. (89) we obtain:

$$2\tau_s \left( \frac{d\gamma_s}{dt} + \gamma_s \frac{d}{dt} \ln N^\infty \right) = 1 - \gamma_s^2 . \quad (93)$$

It is noteworthy that  $N^\infty$ , the final total abundance of particles, as given in Eq. (51), changes only slowly in time when the volume and temperature temporal evolution is governed by the adiabatic evolution condition, Eq. (83). Thus the logarithmic derivative in the dilution term in Eq. (93) is in many cases very small since:

$$\frac{d}{dt} \ln N^\infty = \frac{d}{dt} \ln (x^2 k_2(x)) ; \quad x = \frac{m}{T(t)}. \quad (94)$$

What we see happening is that the volume dilution seen in Eq. (91) is nearly completely compensated by the dilution of the value of  $\rho^\infty(T)$  in presence of adiabatic cooling.

In many cases it is sufficient to study an approximate solution of Eq. (93). For  $m_s/T = x < 1$  we have  $x^2 k_2(x) \simeq \text{Const.}$ , and hence we have the analytical solution:

$$\gamma_s \simeq \tanh \left( \int_0^{t_{\text{freeze}}} \frac{dt}{2\tau_s(T(t))} \right) < 1 \quad m_s/T < 1, \quad (95)$$

where the semi-convergent approximation for the dominant gluon fusion term has been used in the past [59]:

$$\tau_s^g m_s = \alpha_s^{-2} \frac{9}{7} \sqrt{\frac{\pi}{2}} \frac{x^{5/2}}{e^{-x}(x + 99/56 + \dots)} \quad (96)$$

in order to argue that the value of  $\gamma_s$  in many cases of interest approaches unity.

But the approximate solution, Eq. (95), presumes that the final freeze-out occurs such that  $m_s/T < 1$ , which condition is not fulfilled if the plasma hadronizes at temperatures of the magnitude  $T = 140$  MeV as seems to be the case today for the baryon rich plasma, see our discussion in section 8.3 and the results of lattice gauge simulations of QCD [3]. We will now show numerically that major deviations from the approximate solution arise and in particular  $\gamma_s$  can easily become much greater than unity, depending on the precise value of the freeze-out temperature. To see this note that a slight rearrangement of Eq. (93) leads to the form:

$$\frac{d\gamma_s}{dt} = \left( \gamma_s \frac{\dot{T} m_s}{T^2} \frac{d}{dx} \ln x^2 k_2(x) + \frac{1}{2\tau_s} [1 - \gamma_s^2] \right), \quad (97)$$

which shows that even when  $1 - \gamma_s^2 < 1$  we still can have a positive derivative of  $\gamma_s$ , since the first term on the right hand side of Eq. (97) is always positive, both  $\dot{T}$  and  $d/dx(x^2 k_2)$  being always negative. Note that  $1/\tau$  becomes small when  $T$  drops below  $m_s$  and whence the dilution term dominates the evolution of  $\gamma_s$ .

### 7.3 Strangeness and charm in final state

The numerical integration of Eq. (97) is now possible, up to the point at which the plasma phase ceases to exist or/and the final state strange particles are emitted. According to our hypothesis, which leads to a successful interpretation of the experimental data, the abundances of rarely produced strange (anti)baryons is not further affected by subsequent evolution. We present  $\gamma_s$  for the case of S–W/Pb collisions (dashed lines) and Pb–Pb collisions (solid lines), in Fig. 33a as function of final time and in Fig. 33b as function of final temperature. We note that for 8 fm/c we obtain the observed value  $\gamma_s \simeq 0.75$  for the S–W/Pb collisions. However, this time is associated with a low final temperature of  $T = 110$  MeV, as can be deduced from the result shown in Fig. 33b. Taking the final temperature value to be  $T \simeq 140$  MeV for the S–W/Pb case, one arrives at  $\gamma_s \simeq 0.57$ . This is slightly less than the experimental result  $\gamma_s \simeq 0.75$  which suggests that our ideal flow temporal evolution model may be leading to a too fast cooling or/and that the perturbative estimate of the strangeness production rate is a bit too low — to reach exact agreement between experiment and theory we would need a cumulative change in these two here relevant quantities (flow velocity and QGP-strangeness production rate) of magnitude 20%. There is clearly plenty of room for an improvement of this magnitude in both these quantities.

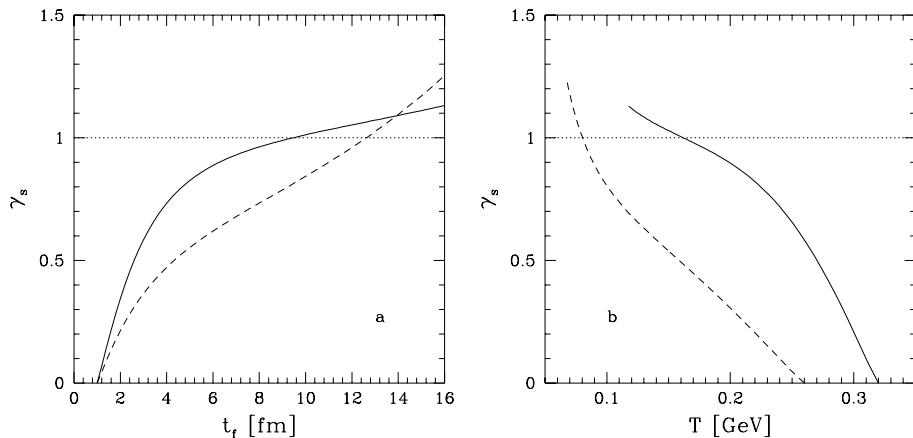


Figure 33: QGP-phase strangeness phase space occupancy  $\gamma_s$  a) as function of time and b) as function of temperature, for  $\alpha_s = 0.6$  and  $m_s = 160$  MeV, for initial conditions pertinent to maximum SPS energies (200A GeV S beam and 158A GeV Pb beam). Solid lines: conditions relevant to central Pb–Pb interactions, dashed lines: conditions relevant to S–W/Pb interactions (see table 2).

When considering the Pb–Pb collisions we are primarily interested to find if it is likely that we reach  $\gamma_s = 1$ . For this to occur, our results, see Fig. 33, suggest that the final QGP fireball temperature should be lower than 160 MeV. Note that allowing for the above discussed likely further increase in production rate and/or reduction in flow, pushes this temperature limit to 210 MeV. We thus can be practically certain that in Pb–Pb collisions at 158A GeV one observes  $\gamma_s \geq 1$  with the associated interesting consequences for strange particle abundances (see section 8.3).

To study the dependence on the impact parameter on strangeness saturation, we vary the magnitude of the initial fireball size  $R_0$ . From geometric considerations one finds roughly the relation between the impact parameter in Pb–Pb collisions,  $b$  and  $R_{\text{in}}$  to be  $R_{\text{in}} \simeq 6 - b/2 > 0$  fm; for small impact parameters  $0 < b < 2$  fm we assume here formation of a ‘standard’ fireball of 5 fm radius. A further assumption is needed regarding initial temperature of the fireball: we will not vary this parameter, leaving it for the Pb–Pb collisions at  $T = 320$  MeV for all fireball sizes. However, for larger impact parameters (small fireball sizes) the actual momentum stopping is reduced and thus the heating and compression of the fireball is less than we have implicitly assumed using a constant value for  $T_{\text{in}}$  for different initial fireball volumes. It is impossible for us to improve on this hypothesis here, since this requires the understanding of the hadronic matter stopping as function of the amount of hadronic matter involved. With this set of initial conditions we integrate the dynamical equation (97) for  $\gamma_s$  up to final temperature  $T \simeq 140$  MeV (see discussion below in section 8) for the 200A GeV S–W/Pb collisions. We find that full strangeness phase space saturation occurs for fireballs with a radius  $R_{\text{in}} > 4$  fm, which includes impacts parameters  $b$  up to about 3-4 fm. This result suggests that there is no need to trigger onto very central collisions in order to observe  $\gamma_s \simeq 1$ . Moreover, The relatively sudden onset of the phase space saturation seen in Fig. 34a as function of fireball size is very probably even more sudden, had we incorporated the changing stopping related to the change of volume.

It is also most interesting to study how  $\gamma_s$  depends on the Pb–Pb collision energy. We obtain this result by varying the initial fireball temperature  $T_{\text{in}}$  and relating this value to the specific energy content in the fireball by the results given in Fig. 15 — we take here the result we obtained for full stopping  $\eta = 1$ . Recall that baryon and energy stopping being equal,  $E/B = 8.6$  GeV corresponds to 158A GeV Pb–Pb collisions. For each initial temperature  $T_{\text{ch}}$  we assume that the initial value of  $\gamma_s$  is 0.15, and integrate the temporal evolution of  $\gamma_s$ , Eq. (97), till the final temperature which is taken for all collision energies to be at  $T = 140$  MeV. As shown

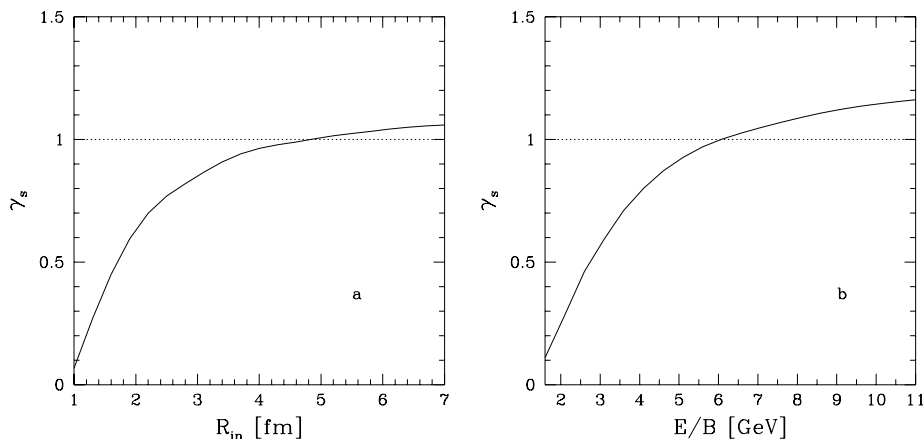


Figure 34: Strangeness phase space occupancy **a)** as function of initial fireball size  $R_{\text{in}}$  assuming initial conditions of the zero impact parameter 158A GeV Pb–Pb collisions; **b)** as function of the CM-specific ion collision energy content, assuming a  $R_{\text{in}} = 5$  fm initial fireball size and freeze-out at 140 MeV.

in Fig. 34**b** for the full SPS range  $4.3 < E/B < 8.6$  GeV we find as expected fully saturated phase space, with  $0.8 < \gamma_s < 1.1$ . Between the AGS  $E/B = 2.6$  GeV and CERN energies  $\gamma_s$  increases from 0.45 to 0.85. We recall that our study of the S–Pb collision system suggests somewhat more effective chemical equilibration, thus the small variation of  $\gamma_s$  with energy reported here may be even less pronounced. On the other hand this small variation impacts the final particle yields as we shall see in section 8.3, in that it makes relative yields of strange antibaryons such as  $\bar{\Lambda}/\bar{p}$ ,  $\bar{\Xi}/\bar{\Lambda}$  nearly independent of collision energy.

We can now briefly return to the discussion of the result of the NA35 collaboration [40] shown in Fig. 11: despite the large error bar it is noticeable that there is a tendency for the  $\bar{\Lambda}/\bar{p}$ -ratio to increase as the collision system becomes smaller. This can be interpreted in terms of  $\gamma_s$  and one finds the normally unexpected result that while S–Au collisions lead to  $\gamma_s \simeq 0.8 \pm 0.2$ , the S–S collisions may require a greater value  $\gamma_s \simeq 1.2 \pm 0.3$ . In the earlier analysis [17] of S–S data (excluding  $\bar{p}$ ) this tendency towards  $\gamma_s \simeq 1$  was also found, while the S–W/Pb results always invariably lead to  $\gamma_s \simeq 0.75$ . In light of the model calculations done above, it is not anymore impossible to imagine that the combination of initial and disintegration conditions of these two systems reverses the naive expectations regarding the final observable values of  $\gamma_s$ , leading to a greater value for the smaller system.

We now explore the saturation of the charmed quark phase space in

conditions sensible for the forthcoming RHIC and LHC environments. We consider the temporal evolution for the initial temperature 500 MeV. Due to the likely dominance of the expansion by the longitudinal flow we take for the adiabatic condition the relation  $LT^3 = \text{Const.}$  We take that  $L$  expands with light velocity. As can be seen in the results shown in Fig. 35 thermal production of charm is small, being very slow, but because the freeze-out temperature should here also be taken in the vicinity of 150 MeV, the phase space occupancy reaches a stunning value *exceeding unity*. Still greater values result for higher initial temperatures and/or lower freeze-out temperatures. We note that the discussion of thermal charm production in this language makes only sense if the number of charmed quark pairs produced in the initial moments is considerably greater than unity. We thus present in Fig. 36 the pair yield as function of initial temperature (assuming small impact parameter collisions). We note that our calculations apply to initial temperatures above 300 MeV and that for  $T_{\text{in}} = 500$  MeV we would be reaching a yield of twenty charm quark pairs per event. We also note that the difference between the thick and thin lines in Figs. 35, 36, indicating that at the energy scale of charm production the uncertainty arising from the error in  $\alpha_s(M_Z)$  is negligible. There remains considerable uncertainty in the evolution model of the fireball, which in the here presented scenario would evolve for up to 25 fm/c.

Let us consider next the running-QCD case and present a series of results for the two strangeness observables  $N_s/B$  and  $\gamma_s(t_f)$  as function of the energy and impact parameter [75]. We present in Fig. 37 the ratio  $N_s/B$  as function of  $B$  and in Fig. 38 as function of  $E/B$ . Solid lines give results for the Pb–Pb collisions, dashed lines correspond to the S–Pb/W case. Thick/thin lines as before refer to small/large  $\alpha_s$  options. In Fig. 37 we see that the specific yield is expected to be 20–40% higher in *central* Pb–Pb collisions than in *central* S–Pb/W collisions — the effect is smaller for the ‘large’  $\alpha_s$  case since we are closer to the saturation of the phase space in the early collision stage. As Fig. 38 shows, the specific yield of strangeness is in a wide range of CM-energies, comprising all the accessible SPS-range, nearly proportional to  $E/B$ . This pattern arises from a number of factors, such as the change in initial temperature with collision energy, the change of strangeness production with temperature, etc. It would be quite surprising to us, if other reaction models without QGP would find this linear behavior with similar coefficients. We therefore believe that this result is an interesting characteristic feature of our QGP thermal fireball model.

The value of  $\gamma_s$  observed by studying the final state hadrons, reflects on the initial production and the enrichment of the strange phase space occupancy by the dilution effect. Consequently it depends, in addition to the

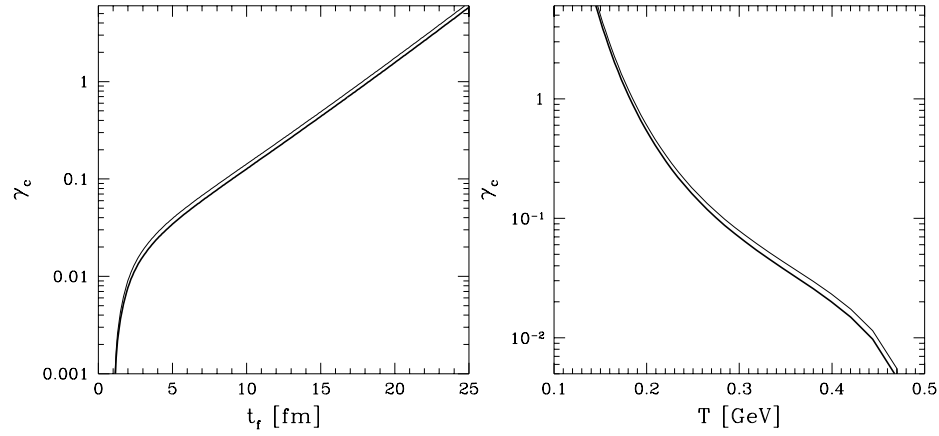


Figure 35: QGP phase charm phase space occupancy  $\gamma_c$  in central Pb–Pb interactions: **a)** as function time and **b)** as function of temperature, for running  $\alpha_s$ .

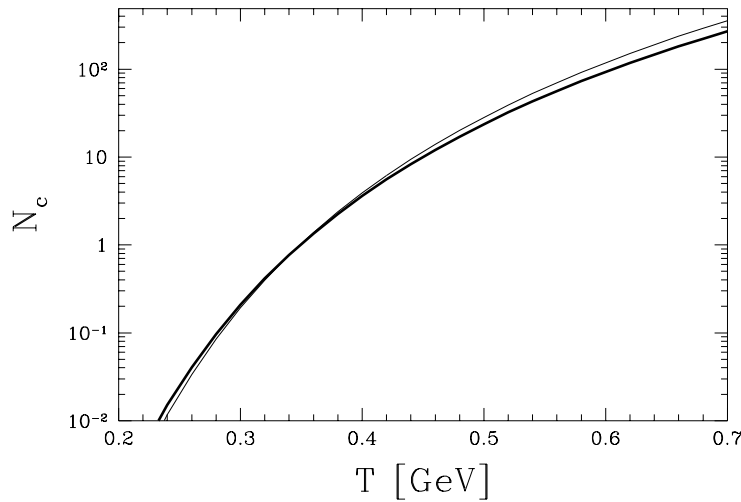


Figure 36: Total charm production yield in longitudinally expanding QGP as function of initial temperature.

dependences we saw in strangeness abundance, sensitively on the freeze-out temperature. High values of  $\gamma_s$  could accompany low freeze-out temperature, provided that there has been extreme initial conditions allowing to reach strangeness phase space saturation long before hadronization. When considering the Pb–Pb collisions at presently explored energy of 158A GeV ( $E/B \simeq 8.6$  GeV), we are primarily interested to know if it is likely that



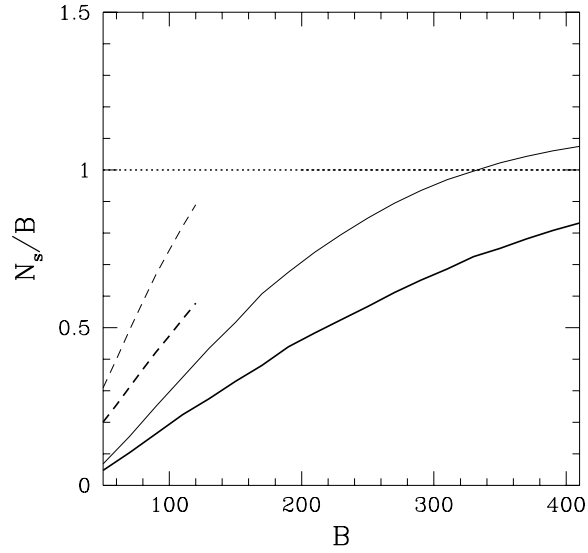


Figure 37: QGP fireball specific strangeness abundance as function of number of participants (solid lines for Pb-Pb, dashed lines for S-W) for running  $\alpha_s$  and  $m_s$ . The freeze-out point is fixed at  $T_f = 140$  MeV. Thick lines for the smaller  $\alpha_s$  option, thin lines for the larger option.

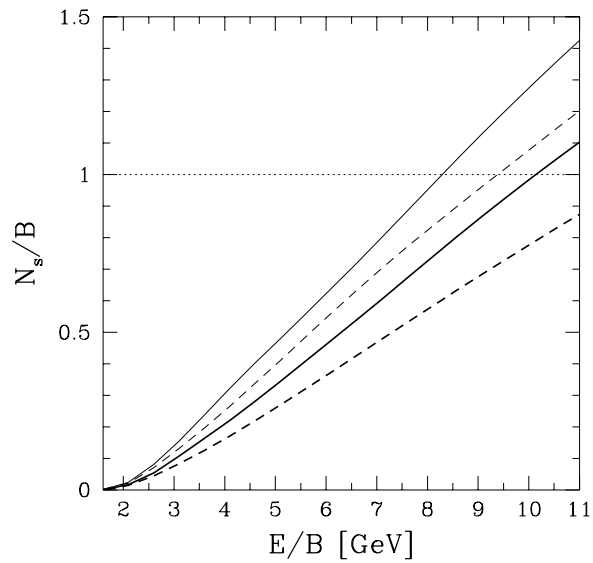


Figure 38: QGP fireball specific strangeness abundance as function of energy per baryon in the fireball  $E/B$ . See Fig. 37 for definitions.

we reach  $\gamma_s = 1$ . In Fig. 39a we present the evolution of  $\gamma_s$  as function of freeze-out temperature in the ‘reasonable’ range  $130 < T_f < 180$  MeV. We assumed here (solid lines) that the fireball was formed in Pb–Pb collisions at nearly zero impact parameter, hence it comprises  $B \simeq 380$  participants and that the energy available for collisions of projectiles with 158A GeV is 8.6 GeV, as is the case should the energy and baryon number stopping be the same. Dashed lines correspond to the 200A GeV S–Pb/W collisions leading to a smaller baryon content  $B = 120$  in central collisions, thus also to smaller  $\gamma_s$  at the same freeze-out temperature. As before, thin lines are for the ‘large’  $\alpha_s$  case, and thus the presented results are systematically ( $\Delta\gamma_s \simeq 0.25$ ) greater than the thick line results. Considering that the freeze-out temperature is not cut in stone as well, this is the typical magnitude of the theoretical uncertainty of the present theoretical evaluation of  $\gamma_s$ .

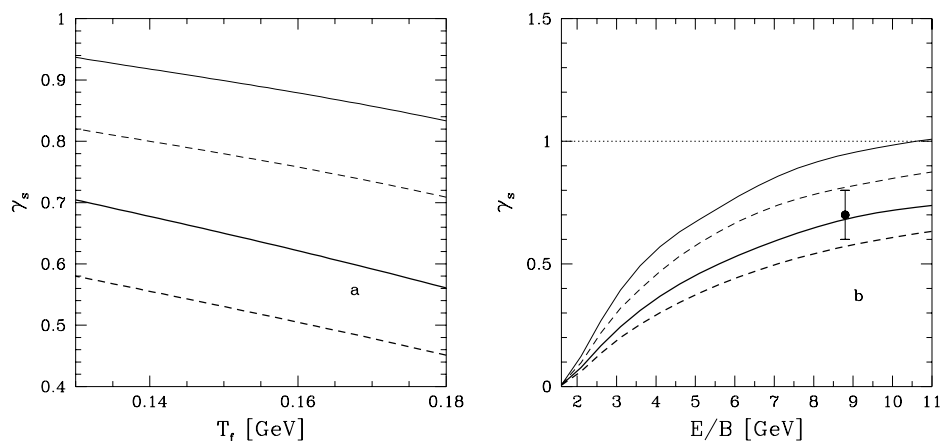


Figure 39: QGP strangeness phase space occupancy  $\gamma_s$  **a)** as function of freeze-out temperature  $T_f$  and **b)** as function of energy per baryon  $E/B$  in the fireball. Lines according to convention in Fig. 37. Initial conditions in **a)** chosen to correspond to Pb–Pb collisions at maximum SPS energies with  $E/B = 8.6$  GeV and  $B \simeq 380$ ; in **b)** we keep the number of constituents at  $B = 380$  in Pb–Pb and  $B = 120$  in S–W and fixed freeze-out point at  $T_f = 140$  MeV. The vertical bar corresponds to the value of  $\gamma_s$  obtain in S–W data analysis [17].

In Fig. 39b we reversed the roles of the variables  $E/B$  and  $T_f$ : we set freeze-out temperature  $T_f = 140$  MeV and consider a zero impact parameter collision with  $B = 380$  (solid lines) and  $B = 120$  (dashed lines) as function of energy content  $E/B$ . The result (dot with vertical bar) we give ( $0.75 \pm 0.1$ ) arises from our analysis [17] of experimental data for 200A GeV S–W/Pb collisions. It is remarkably consistent with our model results. It

may be unwise to view its better agreement with the ‘large’  $\alpha_s$  option as an effective measurement of  $\alpha_s$ : there are too many uncertainties to be refined before we could use strangeness as a measure of the QCD coupling strength. However, our results clearly show that we have the required sensitivity to relate properties of QCD and the perturbative vacuum to the particle yields observed in relativistic nuclear collisions.

## 8 QGP hadronization

### 8.1 Hadronization constraints

It is easy to imagine QGP-hadronization mechanisms that would largely erase memory of the transient deconfined phase. We will not discuss such *re-equilibrating* hadronization models [83] of strange particles which are not observed at least at SPS energies [17]. Instead, we shall focus our attention on the alternative that the particles emerge directly and without re-equilibration from the deconfined phase.

Our approach to hadronization and particle production is schematic and does not involve development of a dynamical model [50]. Instead, we introduce two parameters which describe how far are from the hadronic gas equilibrium the produced meson and baryon abundances. To justify the introduction of these parameters we note that there is no reason whatsoever to expect that the rapid disintegration of the deconfined state will lead to particle abundances that are associated with full chemical equilibrium of any individual particle species in the final state. These hadron nonequilibrium constants  $C_i$  are in principle different for each particle species, but if we presume that the mechanisms that lead to particle production are similar for all mesons ( $i = M$ ), and all baryons ( $i = B$ ), we can group the hadronic particles into these two families, keeping just two unknown quantities. Note that also the *relative* abundances of mesons and baryons emerging from hadronizing QGP are difficult to equilibrate, because processes which convert meson into baryon—antibaryon pairs are relatively slow. The magnitude of these abundance coefficients  $C_i$  is determined theoretically by the need to conserve or increase entropy, conserve baryon number and strangeness in the hadronization process.

We now consider strangeness conservation in the final state: the abundances of the final state strange particles can be gauged by considering the Laplace transform of the phase space distribution which leads to a partition function *like* expression  $\mathcal{Z}_s$ . The individual components comprise aside of the chemical factors  $\lambda_q, \lambda_s$  the non-equilibrium coefficients  $\gamma_s$  and  $C_B^s, C_M^s$

(we have added here the superscript ‘s’ to the factors  $C$  since at present we look only at strange particles):

$$\ln \mathcal{Z}_s = \frac{VT^3}{2\pi^2} \left\{ (\lambda_s \lambda_q^{-1} + \lambda_s^{-1} \lambda_q) \gamma_s C_M^s F_K + (\lambda_s \lambda_q^2 + \lambda_s^{-1} \lambda_q^{-2}) \gamma_s C_B^s F_Y \right. \\ \left. + (\lambda_s^2 \lambda_q + \lambda_s^{-2} \lambda_q^{-1}) \gamma_s^2 C_B^s F_\Xi + (\lambda_s^3 + \lambda_s^{-3}) \gamma_s^3 C_B^s F_\Omega \right\}, \quad (98)$$

where the kaon, hyperon, cascade and omega degrees of freedom are included. Here  $T$  is the freeze-out temperature. The phase space factors  $F_i$  of the strange particles are (with  $g_i$  describing the statistical degeneracy):

$$F_i = \sum_j g_{ij} W(m_{ij}/T). \quad (99)$$

In the resonance sums  $\sum_j$  all known strange hadrons should be counted. The function  $W(x)$  arises from the phase-space integral of the different particle distributions  $f(\vec{p})$ . For the Boltzmann particle phase space (appropriate when the final state mass is equal or greater than the temperature of the source) and when the integral includes the entire momentum range, we have

$$W(x) \equiv (4\pi)^{-1} \int d^3(p/T) f(\vec{p}) = x^2 K_2(x), \quad (100)$$

where as before  $x = m/T$  and  $K_2(x)$  is the modified Bessel function.

There is a strong constraint between the two fugacities  $\lambda_q$ , and  $\lambda_s$  arising from the requirement of strangeness conservation among the final state particles, which was discussed at length recently [17]. The non-trivial relations between the parameters characterizing the final state are in general difficult to satisfy and the resulting particle distributions are constrained in a way which differs considerably between different reaction scenarios which we have considered in detail: the rapidly disintegrating QGP or the equilibrated HG phase. These two alternatives differ in particular by the value of the strange quark chemical potential  $\mu_s$ :

1. In a strangeness neutral QGP fireball  $\mu_s$  is always exactly zero, independent of the prevailing temperature and baryon density, since both  $s$  and  $\bar{s}$  quarks have the same phase-space size.
2. In any state consisting of locally confined hadronic clusters,  $\mu_s$  is generally different from zero at finite baryon density, in order to correct the asymmetry introduced in the phase-space size by a finite baryon content.

At non-zero baryon density, that is for  $\mu_B \equiv 3\mu_q \neq 0$ , there is just one (or perhaps at most a few) special value  $\mu_B^0(T)$  for which  $\langle s \rangle = \langle \bar{s} \rangle$  at  $\mu_s^{\text{HG}} = 0$ , which condition mimics the QGP. We have studied these values carefully [17] for the final state described by Eq. (98): here the condition of strangeness conservation takes the simple analytical form [17, 13]:

$$\mu_q^0 = T \cosh^{-1} \left( R_C^s \frac{F_K}{2F_Y} - \gamma_s \frac{F_{\Xi}}{F_Y} \right), \quad \text{for } \mu_s^{\text{HG}} = 0. \quad (101)$$

Here, and when we consider relative abundance of particles, only the ratio

$$R_C^s = C_M^s / C_B^s \quad (102)$$

appears. We note that there is at most one non-trivial real solution of Eq. (101) for monotonous arguments of  $\cosh^{-1}$ , and only when this argument is greater than unity.

Clearly, the observation [17, 42] of  $\lambda_s = 1$  ( $\mu_s = 0$ ) is, in view of the accidental nature of this value in the confined phase, a rather strong indication for the direct formation of final state hadrons from a deconfined phase. In such a process the particle abundances retain memory of the chemical (fugacity) parameters, the conservation of strangeness and other properties is assured by the (non-equilibrium hadronic gas) abundance numbers of the particles produced. For example the number of baryons emitted even at very low temperatures must remain conserved and thus cannot be tiny despite the thermal suppression factor  $e^{-m/T}$  — a big change in chemical potentials would require lengthy reequilibration. These effects are absent since  $\lambda_s = 1$ , at least in the strangeness chemical potential: for the S–W/Pb collisions at 200A GeV this was found already in the first data analysis [41] and this remarkable result was corroborated by an extensive study of the resonance decays and flow effects [17]. For the S–S collisions at 200A GeV a further refinement [42] which allows for a rapidity dependence of  $\lambda_q$  due to flow further underpins the finding  $\lambda_s = 1$ .

We can thus safely conclude that strange particles produced in 200A GeV Sulphur interactions with diverse targets indicate a particle source which displays a symmetry in phase space size of strange and antistrange particles, which fact is more than just an accident of parameters considering that it appears for two widely different collision systems, S–S and S–W/Pb. A natural explanation is that such a source is deconfined, and that it disintegrates so rapidly, that its properties remain preserved in emitted strange particles. It will be very interesting to see, if this behavior will be confirmed in the Pb–Pb system, with present experiments operating at 158A GeV and possibly later at different collision energies.

We now explore the values of the parameter  $R_C^s$ . We consider the constraint imposed by Eq. (101), taking  $\gamma_s = 0.7$  (the deviation from unity is of little numerical importance),  $\lambda_s = 1$ . For  $\lambda_q$  we take three values in Fig. 41: the solid line is for  $\lambda_q = 1.5$ , choice motivated by the case of S–W/Pb collisions at 200A GeV, the long-dashed line is for  $\lambda_q = 1.6$  suitable for the case of Pb–Pb 160A GeV collisions; the short-dashed curve is for  $\lambda_q = 2.5$ , the value which our model calculations suggest for the 40A GeV collisions (see table 2). The value  $R_C^s = 1$  is found for  $T \leq 200$  MeV at  $\lambda_q \simeq 1.48$ –1.6. For lower disintegration temperatures we would have  $R_C^s < 1$ , as shown in Fig. 41.

The physical observable which we find to be primarily sensitive to the parameter  $R_C^s$ , and to a lesser degree to the other thermal model parameters, is the kaon to hyperon abundance ratio at fixed  $m_\perp$ :

$$R_K|_{m_\perp} \equiv \frac{K_S^0}{\Lambda + \Sigma^0}. \quad (103)$$

When computing this ratio, we have incorporated the decay pattern of all listed resonances numerically and included the descendants of strong and weak decays in order to facilitate comparison below with experimental data. In Fig. 40 we show  $R_K|_{m_\perp}$  as function of  $R_C^s$  for  $\lambda_q = 1.5, 1.6, 2.5$ , with the same line conventions as in the Fig. 41. We assumed that the distribution of parent particles for kaons and hyperons is according to the thermal equilibrium condition evaluated at temperature implied by Fig. 41.

There is no officially reported value for the  $R_K$  ratio. However, WA85 collaboration [21] has presented results for the yields of  $\Lambda$ ,  $\bar{\Lambda}$  and  $K_S$  obtained in S–W collisions at 200A GeV, shown here in Fig. 4, in the interval  $1.1 < m_\perp < 2.6$  GeV for the central rapidity region  $2.5 < y < 3$ . No cascading corrections were applied to these experimental results. From these results we obtain  $R_K|_{m_\perp} = 0.11 \pm 0.02$ . This implies a far off-HG-equilibrium result  $R_C^s = 0.38$  as can be seen in Fig. 40, which according to Fig. 41 leads to a freeze-out temperature  $T_f \simeq 145$  MeV. The equilibrium HG source with  $R_C^s \simeq 1$  ( $R_K|_{m_\perp} \simeq 0.3$ ) is experimentally completely excluded. The factor  $R_C^s \neq 1$  confirms the expectation that these strange particles are produced in non-equilibrium processes — in our model they originate from directly disintegrating QGP fireball. Strangeness conservation constraint fixes the freeze-out condition at  $T \simeq 145$  MeV.

The final issue is how, from the value  $R_C^s \simeq 0.4$ , we can infer the values of the abundance constants  $C_M^s$  and  $C_B^s$  which (see Eqs. (98, 102)) express the relative strange meson and baryon production abundance to the thermal equilibrium values. If we argue that the strange meson abundance, akin to total meson abundance is enhanced by factor two (i.e.,  $C_M^s = 2$ ) as we found studying the entropy enhancement [13], then the conclusion would be

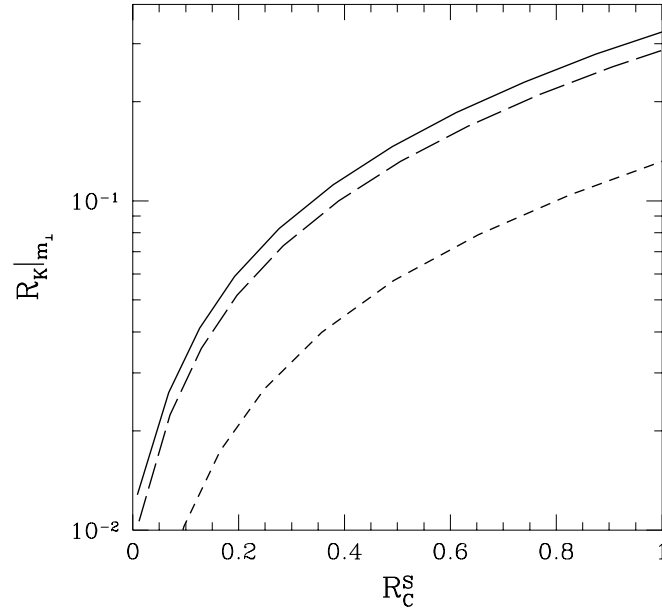


Figure 40:  $R_K|_{m_\perp}$  as function of  $R_C^s$  for  $\lambda_q = 1.5$  (solid line),  $\lambda_q = 1.6$  (long-dashed line) and  $\lambda_q = 2.5$  (short-dashed line).

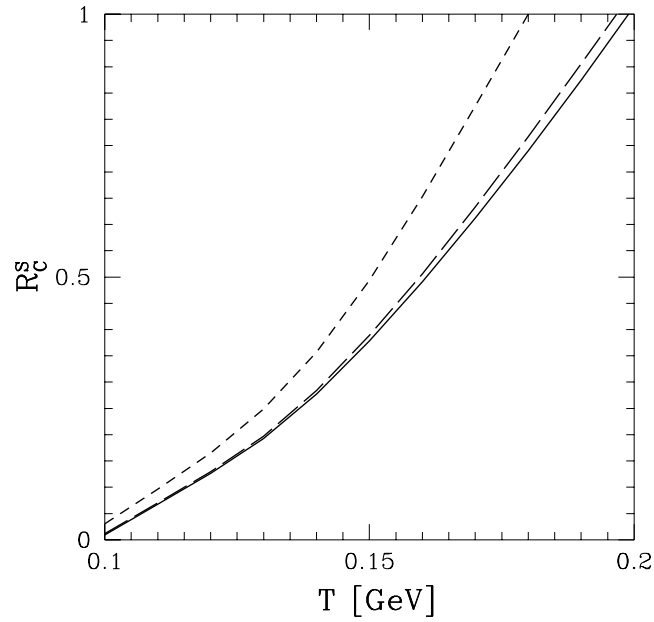


Figure 41: Strangeness neutrality line:  $R_C^s$  versus freeze-out temperature for  $\lambda_q = 1.5$  (solid line),  $\lambda_q = 1.6$  (long-dashed line) and  $\lambda_q = 2.5$  (short-dashed line).

that the strange baryons are enhanced (against their tiny HG equilibrium abundance at  $T_f \simeq 145$  MeV) by the factor  $C_B^s = 5$ .

We thus see that the hadronization abundance of mesons is enhanced by factor 2 and that of baryons by factor  $2 \cdot 2.5 = 5$  compared to the yields that would be expected from a chemically equilibrated HG phase dissociating at about  $T = 145$  MeV. Clearly, one of the important aspects of this result is the relation of the meson enhancement factor to entropy production in heavy ion collision, and we briefly recapitulate the situation which lead to the expected enhancement of meson yield.

## 8.2 Entropy content of heavy ion collisions

One of the fundamental differences between the QGP and the conventional Hagedorn type hadron gas (HG) structure of the fireball, is the specific entropy content per baryon ( $S/B$ ) evaluated at some given (measured) values of statistical parameters. This entropy content can be determined in terms of the final state particle multiplicity. However, in the central rapidity region only few experiments have been able to obtain a full phase space coverage. Because of the need to observe relatively small momentum particles, this is a particularly difficult experimental task and at present the best experimental access to this issue is by means of emulsion techniques. We present here one set of preliminary experimental results which give already a pretty good representation of the specific entropy content in the fireball.

The EMU05 collaboration [84] has studied S–Pb collision at 200 GeV A using a thin Pb-foil placed in front of a emulsion stack. They have concentrated the analysis on central collision events requiring a total final state charged multiplicity to be greater than 300, corresponding to a total central particle multiplicity between 450–1000. They present the multiplicities per interval in rapidity, separately for positive and negative particles. From these data, one can determine the number of protons in the central fireball

$$N_p = \int_{\text{CR}} \frac{d(N^+ - N^-)}{dy} dy \simeq 28. \quad (104)$$

This gives a baryonic number of the fireball  $B$  nearly equal to 60 and corresponds to a stopping  $\eta_B \simeq 50\%$  for the participant nucleons, the reference value being obtained from the geometric tube-like interaction region model, in this case:

$$N_F = \frac{3}{2} A_P^{2/3} A_T^{1/3} + A_P = \frac{3}{2} 32^{2/3} 207^{1/3} + 32 \simeq 120. \quad (105)$$

If we take for the entropy per particle the thermal value for an isolated system of massless particles  $S/N \sim 4$ , (in fact at high  $T$  for massive hadrons



$S/N$  is  $\geq 4$ ), we obtain taking the full multiplicity  $700 \pm 250$ :

$$S/B \sim 50 \pm 20.$$

A more precise analysis of this experiment can be performed by starting from the ratio:

$$D_Q \equiv \frac{\frac{dN^+}{dy} - \frac{dN^-}{dy}}{\frac{dN^+}{dy} + \frac{dN^-}{dy}}, \quad (106)$$

which is found in this experiment to be  $0.085 \pm 0.010$  in the central region (see Fig. 42).

We note that in the numerator of  $D_Q$  the charge of particle pairs produced cancels and hence this value is effectively a measure of the baryon number, but there is a significant correction arising from the presence of strange particles. The denominator is a measure of the total multiplicity — its value is different before or after disintegration of the produced unstable hadronic resonances. Using as input the distribution of final state particles as generated within the hadron gas final state it is found [13] that  $D_Q \cdot S/B$  is nearly independent of the thermal parameters and varies between 4.8, before disintegration of the resonances, to 3 after disintegration (see Fig. 43). It is less than clear that the conservative assumption of the hadronic gas final state is justified, and if we were to assume that, e.g., the deconfined state is hadronizing into the final hadronic particles suddenly, production of resonances would be largely suppressed, and thus the greater value 4.8 would apply. Using the above value of  $D_Q$  we find for the entropy per baryon of the final state we obtain for the entropy content of the emulsion events analyzed by EMU05:

$$35 < S/B < 60,$$

with the upper limit applying in the case that few heavy meson resonances are produced.

We recall that in table 1 we have listed in the bottom entry the entropy content of the final state in different hadronization scenarios. These are the chemical equilibrium results (except for strangeness flavor) for the hadronic gas formed at the given statistical conditions. We note that low temperature hadronization scenario appears to be consistent with the constraints of the EMU05 experiments. Hadronization at these conditions cannot, however, be considered seriously to lead to chemically equilibrated meson and baryon abundances, since the observed final state meson abundance is on average 50% greater than the equilibrium HG value [17]. Several features of final state particle abundances thus suggest that the dissociation of the

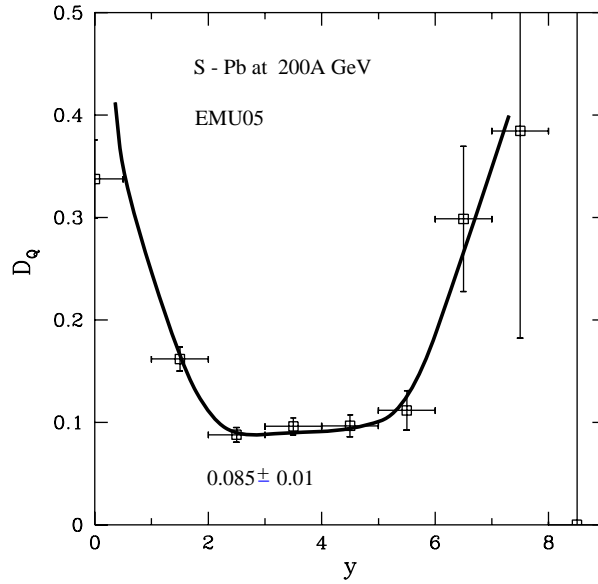


Figure 42: Emulsion data [84] for the charged particle multiplicity from central S-Pb collisions at 200A GeV as a function of rapidity: the difference of positively and negatively charged particles normalized by the sum of both polarities.

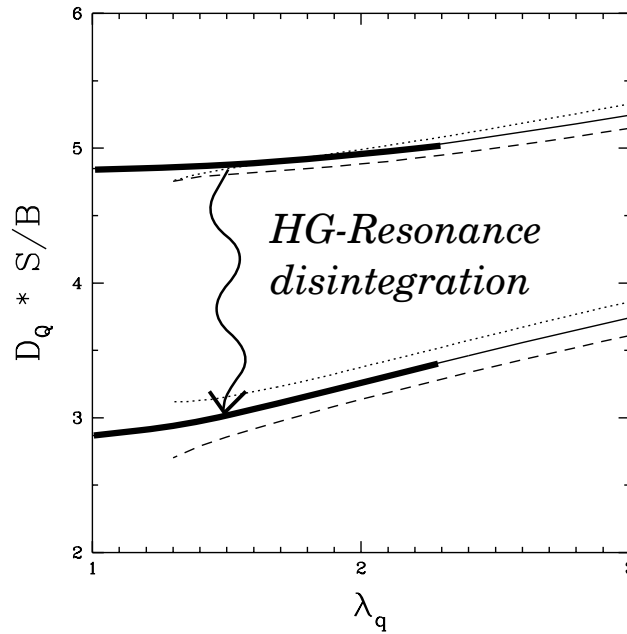


Figure 43: The product  $D_Q \cdot (S/B)$  before (upper curves) and after (lower curves) resonance disintegration, as a function of  $\lambda_q$ , for fixed  $\lambda_s = 1 \pm 0.05$  and conserved zero strangeness in HG. Note the suppressed zero on the vertical axis.

fireball of dense hadronic matter is not leading to chemical equilibrium abundances of final state particles — this is consistent with the sudden ‘explosion’ picture of this process we are employing.

It should be clearly observed at this point that the presence of the high entropy phase precludes a reaction picture of relativistic heavy ion collisions based on conventional thermal hadron gas and adiabatic fireball evolution: the observed high inverse transverse mass slope  $T \simeq 230$  MeV in S–W interactions at 200A GeV implies a initial specific entropy content (see also table 1) which is 1/3 of the final state value. Such a state would have to undergo very entropy generating expansion, and to best of our knowledge there is no experimental evidence for this, nor is there a suggestion of a mechanism that could accomplish such a task. On the other hand, we find that the entropy content of a dense hot QGP fireball formed at the required chemical conditions and later evolving adiabatically (see table 2) just corresponds to the expected value of specific entropy. This allows to conclude that the only currently known reaction picture of relativistic heavy ions involves formation of the thermal QGP fireball.

In our model of thermal fireball evolution the excess entropy is present in the early formation stage of the fireball, and as discussed, the mechanisms of (rapid) entropy formation are not understood. We show in Fig. 44, for the S–W case at  $E/B = 8.8$  GeV and stopping parameter  $\eta = 0.5$ , the qualitative evolution as function of time of  $T$  and  $S/B$ . This result was obtained with the hypothesis

$$\gamma_g = \gamma_q, \quad \gamma_s = \frac{1}{5}\gamma_q \quad \text{when} \quad \gamma_q \leq 1.$$

We observe the considerable drop in temperature from the initial stage to the freeze-out point. *A contrario*, the entropy content which determines the final particle multiplicities evolves very little and 70% of the entropy is already present when quarks and gluons are still far from the equilibrium abundance. Practically all the rise in entropy is due to the formation of the strange flavor (20%), the remaining 10% arise as consequence of the slight change in the value of  $\lambda_q$  given that we enforce during the collision period the condition of dynamical pressure equilibrium.

### 8.3 Final state strange baryon yields

The ratios of strange baryon to strange antibaryon abundance, considering the same type of particles, depends only on the chemical properties of the source. We show in Fig. 45 the three ratios and also  $\bar{p}/p$ . Since we assume  $\lambda_s = 1$ , we obtain here in particular  $R_\Omega = \lambda_s^{-6} = 1$ . However, since some re-equilibration is to be expected towards the HG behavior  $\lambda_s > 1$ , we expect  $\lambda_s = 1 + \epsilon$ , with  $\epsilon$  small, and thus for this ratio  $R_\Omega = 1 - 6\epsilon < 1$ .

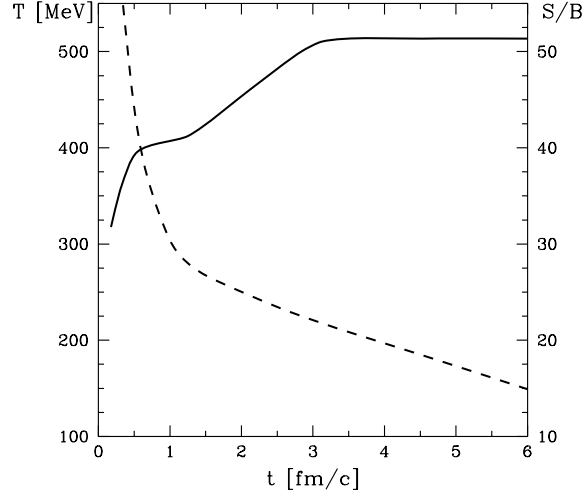


Figure 44: The qualitative evolution of  $T$  (dashed line) and  $S/B$  (solid line) versus time, for the S-W case at  $E/B = 8.8$  GeV and stopping parameter  $\eta = 0.5$ .

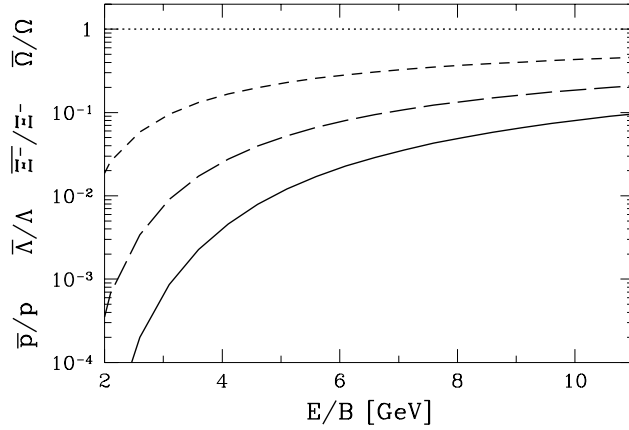


Figure 45: Antibaryon to baryon abundance ratios as function of energy per baryon  $E/B$  in a QGP-fireball:  $R_N = \bar{p}/p$  (solid line),  $R_\Lambda = \bar{\Lambda}/\Lambda$  (long-dashed line),  $R_\Xi = \bar{\Xi}/\Xi$  (short-dashed line) and  $R_\Omega = \bar{\Omega}/\Omega$  (dotted line)

An interesting question which arises quite often is how the individual particle and in particular total antibaryon yields vary with energy. Eq. (98) allows to determine the absolute particle yields as function of fireball energy. Considerable uncertainty is arising from the off-equilibrium nature of the hadronization process, which in particular makes it hard to estimate how the different heavy particle resonances are populated, and also, how the abundance factors  $C_B^s$  vary as function of energy. Some of this

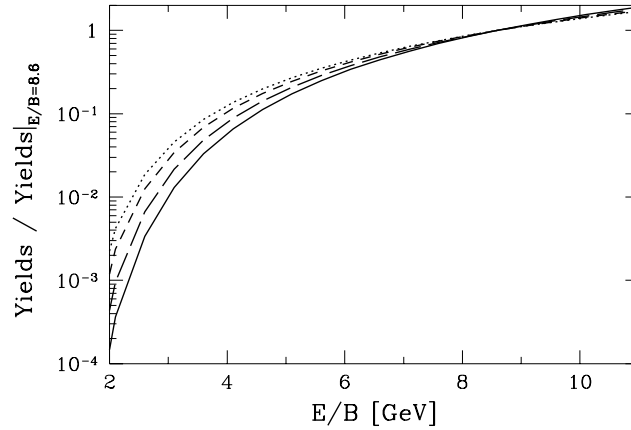


Figure 46: Relative antibaryon yields as function of  $E/B$  in a QGP-fireball with  $\gamma_s = 1$ .  $\bar{p}$  (solid line),  $\bar{\Lambda}$  (long-dashed line)  $\bar{\Xi}^-$  (short-dashed line) and  $\bar{\Omega}$  (dotted line), all normalized to their respective yields at  $E/B = 8.6$  GeV.

uncertainties are eliminated when we normalize the yields at an energy, which we take here to be the value  $E/B = 8.6$  GeV which is applicable to the SPS experiments. In Fig. 46 the so normalized yields of antibaryons taking the freeze-out temperature  $T = 150$  MeV are shown (we also assume  $\gamma_s = 1$ ,  $\eta_p = 1$  and absence of any re-equilibration after particle emission/production).

These yields are decreasing in qualitatively similar systematic fashion with energy, as would be expected from the microscopic considerations, but the decrease of more strange antibaryons is less pronounced. The quantitative point to note is that at AGS ( $E/B = 2.5$  GeV) the yield from a disintegrating QGP-fireball is a factor 100–400 smaller compared to yields at  $E/B = 8.6$  GeV. Since the particle rapidity density  $dN/dy$  is not that much smaller at the lower energies (recall that the specific entropy, see table 2, drops only by factor 3.5, implying a reduction in specific multiplicity by a factor 5), it is considerably more difficult at the lower energies to search for antibaryons than it is at higher energies. We should remember that the results presented in Fig. 46 are obtained assuming formation of the QGP-fireball and same freeze-out and hadronization conditions for all energies shown. We have obtained the result presented in Fig. 46 assuming that the strange phase space saturation is given by the dynamical evolution of a three dimensional radial expansion and freeze-out at  $T = 140$  MeV. Our result was that all particle yields behave in the same qualitative fashion, with the curves falling nearly directly on top of each other. This implies, as we shall see in more detail below, that in a dynamical calculation there is very little, if any variability in particle ratios with energy.

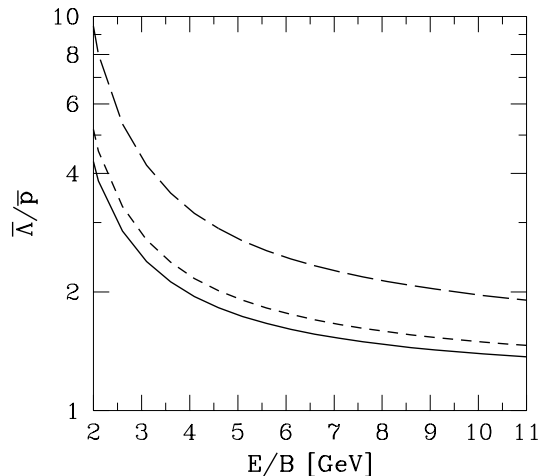


Figure 47: Strange antibaryon ratio  $\bar{\Lambda}/\bar{p}$ , as function of  $E/B$  in a QGP-fireball for  $\gamma_s = 1$ ; solid lines are for full phase space coverage, short dashed line for particles with  $p_{\perp} \geq 1$  GeV and long dashed line for particles with  $m_{\perp} \geq 1.7$  GeV.

We next present the particle ratio results assuming first  $\gamma_s = 1$ , and we turn to consider the variation of  $\gamma_s$  with energy below. The choice  $\gamma_s = 1$  is appropriate if we had a relatively large, long-lived QGP fireball created in central collisions of largest available nuclei, or if our computation of the variation of  $\gamma_s$  with energy was underestimating strongly the actual production rates. In the Figs. 47–49 we show three ratios and for each ratio three results: solid lines depicts the result for the full phase space coverage, short dashed line for particles with  $p_{\perp} \geq 1$  GeV and long dashed line for particles with  $m_{\perp} \geq 1.7$  GeV. In Fig. 47 we show the ratio  $\bar{\Lambda}/\bar{p}$ , in Fig. 48 the ratio  $\bar{\Xi}^-/\bar{\Lambda}$  and in Fig. 49 the ratio  $\bar{\Omega}/\bar{\Xi}^-$ . Because  $\lambda_q$  rises with decreasing  $E/B$  and we have kept  $\gamma_s = 1$ , we find that these three ratios increase quite strongly *as the collision energy is reduced*. The behavior of particle ratios shown in Figs. 47–49 may be of considerable importance, since in reaction models in which QGP is not assumed and the particles are made in a sequence of microscopic collisions these ratios *do increase* from production thresholds with the collision energy, reflecting in this behavior the phase space factors inherent in the reaction cross section.

We now directly compare our theoretical results with the experimental data we have reported in section 3.3: the WA85  $\Omega/\Xi^-$  production ratio obtained for the S-W at 200A GeV [39]; the  $\bar{\Lambda}/\bar{p}$  ratio of the NA35 collaboration obtained for the S-Au system at 200A GeV [40]. Fig. 50 shows a comparison of our ab initio calculation and the pertinent experimental

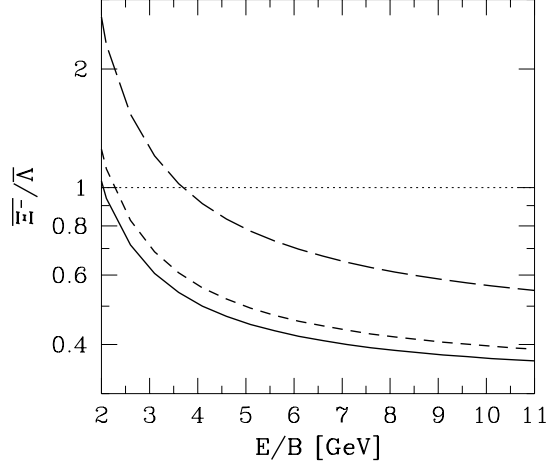


Figure 48: Strange antibaryon ratio  $\overline{\Xi}^-/\overline{\Lambda}$  for  $\gamma_s = 1$ , with the same conventions as in Fig. 47.

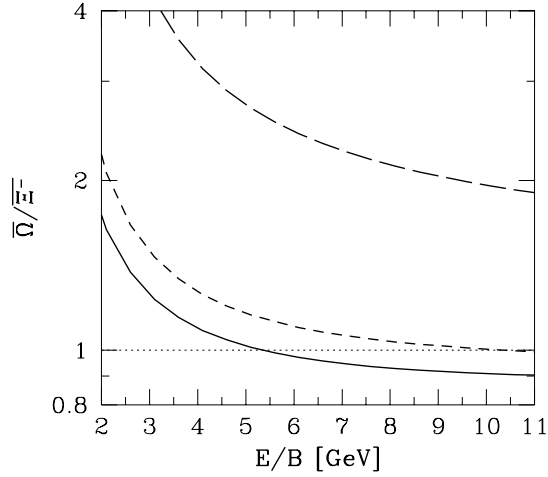


Figure 49: Strange antibaryon ratio  $\overline{\Omega}/\overline{\Xi}^-$  for  $\gamma_s = 1$ , with the same conventions as in Fig. 47.

results. We use the same cuts on the range of  $p_\perp$  as in the experiment: the experimental points show the results  $\overline{\Lambda}/\overline{p} \simeq 0.8 \pm 0.25$  (NA35) for full phase space,  $\overline{\Xi}^-/\overline{\Lambda} = 0.21 \pm 0.02$  (WA85) for  $p_\perp > 1.2$  GeV; and  $(\overline{\Omega} + \overline{\Xi}^-)/(\overline{\Xi}^- + \overline{\Xi}^-) = 0.8 \pm 0.4$  (WA85) for  $p_\perp > 1.6$  GeV. The values  $\gamma_s = 0.70$  and  $\eta_p = 0.5$  also bring about good agreement of our model with

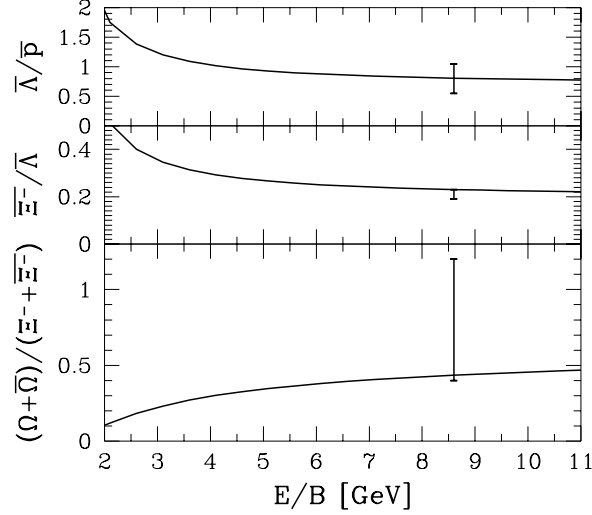


Figure 50: Strange antibaryon ratios for S–W/Pb collisions as function of  $E/B$  in a QGP-fireball:  $\bar{\Lambda}/\bar{p}$  (full phase space),  $\bar{\Xi}^-/\bar{\Lambda}$  for  $p_\perp > 1.2$  GeV and  $(\bar{\Omega}+\bar{\Omega})/(\bar{\Xi}^-+\bar{\Xi}^-)$  for  $p_\perp > 1.6$  GeV; experimental results shown are from experiments NA35, WA85.

the precise value of  $\bar{\Xi}^-/\bar{\Lambda}$ . Fig. 50 shows also the impact of the change of the collision energy on these results, using 50% stopping, rather than  $\eta = 1$  used in Figs. 47–49. We can conclude that the fact that the two ratio  $\bar{\Lambda}/\bar{p}$  (NA35) and  $(\bar{\Omega} + \bar{\Omega})/(\bar{\Xi}^- + \bar{\Xi}^-)$  (WA85) are satisfactorily explained, provides a very nice confirmation of the consistency of the thermal QGP fireball model. Moreover, considering that we have now the power to compute without ad hoc assumptions within the framework of dynamical model, it is quite remarkable that such a good agreement with the two very recent results could be attained.

It is worthwhile to note that even when we incorporate in these strange antibaryon ratios in Figs. 47–49 the variation of  $\gamma_s$  shown in Fig. 34, with considerable decrease of  $\gamma_s$  with decreasing energy (here shown as function of lab energy in the collision, (logarithmic scale), we still retain the remarkable behavior that the ratios do not decrease significantly with decreasing energy down to the energy thresholds for the production of the (multi)strange (anti)baryons. There can be little doubt that if this behavior should be observed down to some low energy in heavy ion collisions, and subsequently a sudden drop should occur, we could safely conclude about a change in the reaction scenario, and probably even pinpoint the mechanisms presented here as being at the origin of this result.



Finally, let us redraw some of the above results in Fig. 52 as function of the beam energy, for the central collisions of symmetric (Pb–Pb, Au–Au) and asymmetric (S–W/Pb) systems. To the left in Fig. 52 we present  $\gamma_s(t_f)$  used in Fig. 51, which depends as discussed on both the initial production and the enrichment of the strange phase space occupancy by the dilution effect, and thus on freeze-out conditions, here assumed to occur at  $T_f = 140$  MeV. High values of  $\gamma_s$  should accompany low freeze-out temperature, provided that there has been extreme initial conditions allowing to produce strangeness. To the right we present the specific strangeness yield. We recall that for S–Ag collisions at 200A GeV a recent evaluation of the strangeness yield leads to  $N_s/B = 0.86 \pm 0.14$  (see table 4 of Ref. [10]) which fits also nicely into the range of values shown at 200 GeV in Fig. 52.

## 9 Summary and conclusions

While it is today impossible, based solely on current experimental results, to claim that the ‘macroscopic’, deconfined QCD-phase has been discovered in the 200A GeV collisions, we have developed the experimental and theoretical ‘strangeness’ tools which allow to resolve in the foreseeable future this question. Today, we can affirm that the natural hypothesis of a QGP-fireball provides us within the thermal fireball model with a very com-

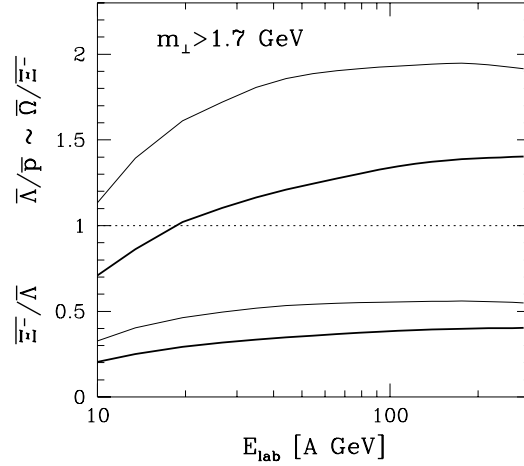


Figure 51: Fixed  $m_{\perp}$   $\bar{\Lambda}/\bar{p}$  and  $\bar{\Xi}^-/\bar{\Lambda}$  as function of beam energy  $E_{lab}$  in the collision (logarithmic scale) arising from a Pb–Pb central interaction fireball, taking into account variation of  $\gamma_s$  computed with running  $\alpha_s$ ,  $m_s(M_Z) = 90$  MeV, for thick lines  $\alpha_s(M_Z) = 0.102$ , for thin lines  $\alpha_s(M_Z) = 0.115$ .

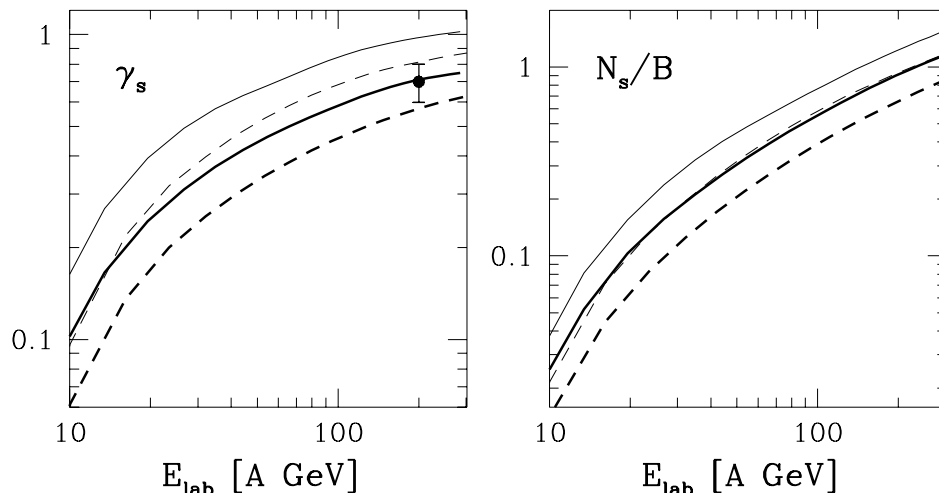


Figure 52:  $\gamma_s(t_f)$  and  $N_s/B$  as function of beam energy for central S–W/Pb collisions (dashed lines) and Pb–Pb collisions (solid lines) assuming  $m_s(M_Z) = 90$  MeV, for thick lines  $\alpha_s(M_Z) = 0.102$ , for thin lines  $\alpha_s(M_Z) = 0.115$ , three dimensional expansion of the fireball with  $v = c/\sqrt{3}$ , and stopping 50% (S–W/Pb), 100% (Pb–Pb). For  $\gamma_s$  we take freeze-out at  $T_f = 140$  MeV — the vertical bar corresponds to the value of  $\gamma_s$  found in S–W data analysis [41].

prehensive and satisfactory explanation of all available experimental data both at 200A GeV and 10-15A GeV. While the lower energy is also well described by the HG type models, the 200A GeV results are incompatible with an assumed HG structure of the interacting hadronic matter in the thermal fireball, or cascades of conventional hadrons studied in transport approaches [45].

We have described in detail how production and final state manifestation of strangeness in antibaryon yields, can help today to identify and study the properties of the deconfined phase. Our exploration of thermal charm production has shown that open charm could become an interesting probe of initial conditions reached at LHC energies.

We have shown that the experimental results suggest that the thermal (kinetic) equilibrium is established, while the chemical (particle abundance) equilibrium in the processes governing final state particle freeze-out is not achieved in 200A GeV collisions. Motivated by the absence of chemical particle abundance equilibrium, we developed and used here a picture of final state hadron production which involves rapid disintegration of the QGP-fireball. Central to the particle abundances are then the chemical properties of the QGP-fireball and we have discussed these comprehensively

as function of collision energy and stopping.

We have shown how a kinetic reaction picture model allows to determine the thermal conditions reached in high density deconfined matter created in heavy ion collisions. It is based on the observation that during the collision the compression of the quark-gluon matter can proceed until the internal pressure exerts sufficiently strong counter force. Using so established initial conditions and adiabatic fireball expansion, we have shown that the thermal conditions we find at the end of the evolution, see bottom of table 2, are in good agreement with our expectations derived from particle yields seen in S–Pb/W 200 GeV A collisions. To wit we needed to make a reasonable choice of the physical parameters: at  $T = 250\text{--}300$  MeV we took  $\alpha_s = 0.6$ , justified for the purpose of strangeness production by our study of running QCD properties in section 6.3, for stopping we adopted  $\eta = 50\%$  based on experimental data [57], about equal for baryon number, energy and momentum. Given these assumptions, we were able to study the current strange particle data at 200A GeV and have reached good agreement with experiment.

We studied in detail the production and evolution of total strangeness abundance in a dynamical QGP fireball evolution model. As expected we found that the large strangeness abundance produced in the early stages will not be reannihilated. We presented the yields as function of both, the collision energy and number of participating baryons (impact parameter). We saw that the yield is rising linearly with the CM-energy per baryon, and that as far as data is available, it is in excellent agreement with the 200A GeV experiment S–Ag [10]. We also explored in detail the evolution of the strangeness phase space occupancy. Strangeness can overpopulate the available phase space at plasma disintegration at low freeze-out temperatures, and thus strange antibaryon abundances could show  $\gamma_s > 1$ , even though our reaction picture leads to values  $\gamma_s \simeq 1$  — as this discussion shows,  $\gamma_s$  is a sensitive probe of both the initial, and final freeze-out conditions.

The last figures shown above in many ways are fruit of the many individual developments we presented here. The computation of relative strange antibaryon yields shown in Fig. 51 was done without ad hoc parameters but there remains some uncertainty about  $m_s(M_Z)$  and the reaction mechanism, here in particular stopping fraction  $\eta$ . This result is special as it shows that the strange antibaryon ratio as the energy of the interaction is reduced, but deconfined phase still reached, is at worse slightly declining, but still anomalously large at AGS (10A GeV) or at minimal energies reachable at SPS (40A GeV). This justifies an exploration of the energy behavior of this central rapidity observable.

Similar comments apply to the less directly measured observables, the

freeze-out strangeness occupancy  $\gamma_s(t_f)$  and the specific strangeness yield, shown above in Fig. 52. In particular the large strangeness yield deserves attention, which as we noted earlier is essentially linearly proportional to the available CM-energy in the fireball.

Our results overall imply that in key features the strange particle production results obtained at 200A GeV, are consistent with the QGP hypothesis of the central, thermal fireball. However, in order to ascertain the possibility that indeed the QGP phase is already formed at 200A GeV a more systematic exploration as function of collision energy of these observables would be needed — conclusions drawn from a small set of experimental results suffer from the possibility that some coincidental and unknown features in the reaction mechanisms could simulate just the observed QGP-like properties. It is highly unlikely that this would remain the case, should a key feature such as collision energy be varied. We stress that our description and hence the anomalous behavior of particle production discussed here is based on collective mechanisms (QGP-fireball), which is intrinsically different from microscopic approaches, in particular when these are based on a hadronic cascade picture.

We hope to have conveyed to the reader the reason why we firmly believe, considering the results we have reported, that experimental data on strange (anti)baryon production provides the best hadronic signatures, and diagnostic tools, of the deconfined matter. It seems that the discovery of the deconfined QGP-phase of hadronic matter is just around the corner.

J.R. acknowledges partial support by DOE, grant DE-FG03-95ER40937. Laboratoire de Physique Théorique et Hautes Energies (LPTHE) is: Unité associée au CNRS UA 280.

## References

- [1] R. Hagedorn, *Suppl. Nuovo Cimento* **2**, 147 (1965); Cargèse lectures in Physics, Vol. **6**, Gordon and Breach (New York 1977) and references therein; see also contributions in: J. Letessier, H. Gutbrod and J. Rafelski *Hot Hadronic Matter*, Plenum Press NATO-ASI series B346, New York (1995);  
H. Grote, R. Hagedorn and J. Ranft, *Particle Spectra*, CERN black report (1970).
- [2] J. W. Harris and B. Müller, *The search for the Quark-Gluon Plasma*, to appear in: *Ann. Rev. Nucl. Science*, preprint hep-ph/9602235 (1996).
- [3] C. DeTar, *Quark Gluon Plasma in Numerical Simulations of lattice QCD*, in: *Quark Gluon Plasma 2*, p. 1, R.C. Hwa, ed., World Scientific, (Singapore 1995).  
T. Blum, L. Kärkkäinen, D. Toussaint, S. Gottlieb, *Phys. Rev. D* **51**, 5153 (1995).
- [4] E.L. Feinberg, *Nuovo Cimento A* **34**, 39 (1976);  
E. Shuryak, *Phys. Lett. B* **78**, 150 (1978).

- [5] C.-Y. Wong *Introduction to High Energy Heavy Ion Collisions*, World Scientific, (Singapore 1994).
- [6] J. Rafelski, *Phys. Rep.* **88** 331 (1982);  
J. Rafelski and R. Hagedorn, in: *Statistical Mechanics of Quarks and Hadrons*, H. Satz, ed., North Holland, (Amsterdam 1981) p. 253;  
J. Rafelski, in: *Workshop on Future Relativistic Heavy Ion Experiments*, R. Bock and R. Stock, eds., GSI-Yellow Report 81-6, (Darmstadt 1981) p. 282;  
M. Jacob and J. Rafelski, *Phys. Lett. B* **190**, 173 (1985).
- [7] P. Koch, B. Müller, and J. Rafelski, *Phys. Rep.* **142**, 167 (1986);  
H.-C. Eggers, and J. Rafelski, *Int. J. Mod. Phys. A* **6**, 1067 (1991);  
J. Rafelski, J. Letessier and A. Tounsi, Flavor flow signatures of quark-gluon plasma, in: *Relativistic Aspects of Nuclear Physics*, T. Kodama et al., eds., World Scientific, (Singapore 1996).
- [8] J. Sollfrank and U. Heinz, The role of strangeness in ultrarelativistic nuclear collisions, in: *Quark Gluon Plasma 2*, R.C. Hwa, ed., World Scientific, (Singapore 1995) p. 555.
- [9] *Strangeness in Hadronic Matter: S'95* Proceedings of Tucson workshop, January 1995, American Institute of Physics Proceedings Series Vol. **340**, J. Rafelski, ed., (New York 1995).
- [10] M. Gaździcki and D. Röhrich, *Strangeness in Nuclear Collisions* preprint IKF-HENPG/8-95, *Z. Physik C* (1996).
- [11] J. Bartke et al. (NA35 Collaboration) *Z. Physik C* **48**, 191 (1990);  
T. Alber et al. (NA35 Collaboration) *Z. Physik C* **64**, 195 (1994).
- [12] H. Bialkowska, M. Gaździcki, W. Retyk and E. Skrzypczak, *Z. Physik C* **55**, 347 (1992).
- [13] J. Rafelski, J. Letessier and A. Tounsi, *XXVI International Conference on High Energy Physics*, Dallas, (1992) AIP-Conference Proceedings No 272, J.R. Sanford, ed., p. 272;  
J. Letessier, A. Tounsi, U. Heinz, J. Sollfrank and J. Rafelski, *Phys. Rev. Lett.* **70**, 3530 (1993);  
M. Gaździcki, *Z. Physik C* **66**, 659 (1995).
- [14] *Hot Hadronic Matter*, Proceedings of NATO-Advanced Research Workshop held in Divonne (1994), J. Letessier, H.H. Gutbrod and J. Rafelski, eds., NATO Physics series Vol. B **346**, Plenum Press, (New York 1995).
- [15] D. Boal, C.K. Gelbke and B. Jennings, *Rev. Mod. Phys.* **62**, 553 (1990).
- [16] T. Matsui and H. Satz, *Phys. Lett. B* **178**, 416 (1986).
- [17] J. Letessier, A. Tounsi, U. Heinz, J. Sollfrank and J. Rafelski, *Phys. Rev. D* **51**, 3408 (1995);  
J. Sollfrank, M. Gaździcki, U. Heinz and J. Rafelski, *Z. Physik C* **61**, 659 (1994);  
J. Letessier, J. Rafelski and A. Tounsi, *Phys. Lett. B* **321**, 394 (1994).
- [18] J. Letessier, J. Rafelski and A. Tounsi, *Energy dependence of strange particle yields from a quark-gluon plasma fireball* Preprint AZPH-TH/95-13 and PAR/LPTHE/95-24, submitted to *Phys. Rev. C*;  
*Quark-gluon plasma formation and strange antibaryons*, Preprint AZPH-TH/95-14R and PAR/LPTHE/95-36R, submitted to *Phys. Lett. B* ; *Phys. Lett. B* **333**, 484 (1994).

- [19] E. Andersen et al., *Phys. Lett. B* **320**, 328 (1989).
- [20] A. Schnabel and J. Rafelski, *Phys. Lett. B* **207**, 6 (1988); and in: Proceedings of the 3rd Conference on the Intersection between Particle and Nuclear Physics, Rockport, 1988, G. Bunce, ed., AIP Proceedings Series No. 176, p.1068, (New York 1988).
- [21] D. Di Bari et al., (WA85 Collaboration) *Nucl. Phys. A* **590**, 307c (1995); D. Evans (WA85 collaboration), in: [9], p.234 (1995).
- [22] J. Beachler et al. (NA35 Collaboration), *Phys. Rev. Lett.* **72**, 1419 (1994).
- [23] R. Santo et al. (WA80 collaboration), *Nucl. Phys. A* **566**, 61c (1994); R. Albrecht et al. (WA80 collaboration), *Production of  $\eta$  Mesons in 200A GeV S+S and S+Au*. Münster Preprint IKP-MS-95/0701; K.H. Kampert and H. Gutbrod, private communication.
- [24] J.B. Kinson et al. (WA94 collaboration), *Nucl. Phys. A* **590**, 317c (1995); S. Abatzis et al. (WA94 collaboration) *Phys. Lett. B* **354**, 178 (1995).
- [25] J. Letessier and A. Tounsi, *Phys. Rev. D* **40**, 2914 (1989); M. Kataja, J. Letessier, P.V. Ruuskanen and A. Tounsi, *Z. Physik C* **55**, 153 (1992).
- [26] M. Masera et al. (NA34/3 Collaboration) *Nucl. Phys. A* **590**, 93c (1995).
- [27] I. Tserruya, *Nucl. Phys. A* **590**, 127c (1995).
- [28] P. Wurm et al. (NA45 Collaboration) *Nucl. Phys. A* **590**, 103c (1995).
- [29] S. Ramos et al. (NA38 Collaboration) *Nucl. Phys. A* **590**, 117c (1995), and references therein.
- [30] D.E. Kharzeev and H. Satz, *Charmonium Composition and Nuclear Suppression*, CERN-TH/95-214, *Phys. Lett. B*, in press (1996).
- [31] S. Chapman, P. Scotto and U. Heinz, *Heavy Ion Physics* **1**, 1 (1995); S. Chapman, J. R. Nix and U. Heinz, *Phys. Rev. C* **52**, 2694 (1995); U. A. Wiedemann, P. Scotto and U. Heinz, *Phys. Rev. C* **53**, February 15 (1996).
- [32] T. Alber et al. (NA35 Collaboration), *Z. Physik C* **66**, 77 (1995).
- [33] B.V. Jacak et al. (NA44 Collaboration), *Nucl. Phys. A* **590**, 215 (1995).
- [34] M. Gazdzicki and D. Roehrich, Frankfurt University Preprint, IKF-HENPG/8-95, in print, *Z. Physik C* (1996).
- [35] *Particle Production in Highly Excited Matter*, Proceedings of IICiocco NATO Summer School, July 1992, H.H. Gutbrod and J. Rafelski, eds., NATO Physics series Vol. B **303**, Plenum Press, (New York 1993).
- [36] E. Quercigh, in: [35], p. 175 (1993).
- [37] J. Bartke et al. (NA35 Collaboration), *Z. Physik C* **48**, 191 (1990).
- [38] H. Bialkowska, M. Gazdzicki, W. Retyk and E. Skrzypczak, *Z. Physik C* **55**, 347 (1992).
- [39] F. Antinori, in: [9]; S. Abatzis et al. (WA85 collaboration), *Phys. Lett. B* **347**, 158 (1995).
- [40] T. Alber et al. (NA35 collaboration), preprint IKF-HENPG/5-95, submitted to *Phys. Lett. B* (1995); J. Günther et al. (NA35 collaboration), *Nucl. Phys. A* **590**, 487c (1995).

- [41] J. Rafelski, *Phys. Lett. B* **262**, 333 (1991); *Nucl. Phys. A* **544**, 279c (1992).
- [42] C. Slotta, J. Sollfrank and U. Heinz, in: [9].
- [43] M. Gaździcki, private communication.
- [44] S. Abatzis, et al. (WA85 collaboration), *Phys. Lett. B* **316**, 615 (1993);  
D. Evans et al. (WA85 collaboration), *Nucl. Phys. A* **566**, 225c (1994);  
S. Abatzis, et al. (WA85 collaboration), *Phys. Lett. B* **347**, 158 (1995).
- [45] N.S. Amelin, L.V. Bravina, L. P. Csernai, V.D. Toneev, K.K. Gudima and S.Yu. Sivoklokov, *Phys. Rev. C* **47**, 2299 (1993);  
H. Sorge, *Phys. Lett. B* **344**, 35 (1995).
- [46] T. Åkesson et al. (AFS-ISR Collaboration), *Nucl. Phys. B* **246**, 1 (1984).
- [47] P. Bordalo for the NA38 collaboration, in: [9], p. 152;  
and *Phys. Lett. B* (in press).
- [48] J. Rafelski and M. Danos, *Phys. Lett. B* **192**, 432 (1987); *Phys. Rev. D* **27**, 671 (1983).
- [49] T. Biró and J. Zimányi, *Phys. Lett. B* **113**, 6 (1982); *Nucl. Phys. A* **395**, 525 (1983).
- [50] L.P. Csernai and I.N. Mishustin, *Phys. Rev. Lett.* **74**, 5005 (1995).
- [51] J. Rafelski and M. Danos *Phys. Rev. C* **50**, 1684 (1994);
- [52] J. Letessier, J. Rafelski and A. Tounsi, *Phys. Lett. B* **328**, 499 (1994).
- [53] J. Letessier, J. Rafelski and A. Tounsi, *Phys. Rev. C* **50**, 406 (1994); *Acta. Phys. Pol. A* **85**, 699 (1993).
- [54] K. S. Lee, U. Heinz and E. Schnedermann, *Z. Physik C* **48**, 525 (1990);  
E. Schnedermann and U. Heinz, *Phys. Rev. Lett.* **69**, 2908 (1992); *Phys. Rev. C* **47**, 1738 (1993);  
E. Schnedermann, J. Sollfrank and U. Heinz, in: [35], p. 175.
- [55] J. Rafelski, *Phys. Lett. B* **190**, 167 (1987).
- [56] J. Sollfrank, P. Koch and U. Heinz, *Phys. Lett. B* **253**, 256 (1991); *Z. Physik C* **52**, 593 (1991).
- [57] I. Otterlund, *Physics of Relativistic Nuclear Collisions*, in: [35], p. 57,  
S.P. Sorensen et al., *Nuclear Stopping Power*, in: *Proc. XXI Int. Symposium on Multiparticle Dynamics 1991*, World Scientific, (Singapore 1992).
- [58] S.R. de Groot, W.A. van Leeuwen and Ch.G. van Weert, *Relativistic Kinetic Theory*, North Holland, (Amsterdam 1980).
- [59] J. Rafelski and B. Müller, *Phys. Rev. Lett.* **48**, 1066 (1982); **56**, 2334E (1986).
- [60] J. Letessier, J. Rafelski and A. Tounsi, *Phys. Lett. B* **323**, 393 (1994).
- [61] G.S.F. Stephans et al. (E859 collaboration), *Nucl. Phys. A* **566** (1994) 269c.
- [62] D.P. Morrison et al. (E859 collaboration), *Nucl. Phys. A* **566** (1994) 457c.
- [63] M. Gonin et al. (E802/E866 collaboration), *Nucl. Phys. A* **566**, 601c, (1994).
- [64] Y. Pang, T.J. Schlagel and S.H. Kahana, *Phys. Rev. Lett.* **68**, 2743 (1992);  
T.J. Schlagel, S.H. Kahana and Y. Pang, *Phys. Rev. Lett.* **69**, 1290 (1992).

- [65] T.S. Biró, P. Lévai and B. Müller, *Phys. Rev. D* **42**, 3078 (1990).
- [66] T. Altherr and D. Seibert, *Phys. Lett. B* **313**, 149 (1993); *Phys. Rev. C* **49**, 1684 (1994).
- [67] N. Bilić, J. Cleymans, I. Dadić and D. Hislop, *Phys. Rev. C* **52**, 401 (1995).
- [68] B. Combridge, *Nucl. Phys. B* **151**, 429 (1979).
- [69] I. Gradshteyn and I. Ryzhik, *Table of integrals, series, and products* Academic Press INC., (1980).
- [70] P. Koch and J. Rafelski, *Nuc. Phys. A* **444**, 678 (1985).
- [71] A. Capella, *Strangeness Enhancement in Heavy Ion Collisions* Preprint LPTHE Orsay 94-113;  
A. Capella, A. Kaidalov, A. Kouider Akil, C. Merino and J. Tran Thanh Van, Preprint LPTHE Orsay 95-41, June 1995.
- [72] P. Langacker, *Precision Experiments, Grand Unification, and Compositeness*, preprint NSF-ITP-140, UPR-0683T, (1995).
- [73] M.B. Voloshin, *Precision determination of  $\alpha_s$  and  $m_b$  from QCD sum rules for  $b\bar{b}$* , preprint TPI-MINN-95/1-T and UMN-TH-11326-95, (1995).
- [74] J. Ellis, E. Gardi, M. Karliner and M.A. Samuel, *Padé approximants, Borel transforms and renormalons: the Bjorken sum rule as a case study*, preprint, CERN-TH/95-1155 (1995).
- [75] J. Letessier, J. Rafelski and A. Tounsi, *Impact of QCD and QGP properties on strangeness production*, submitted to *Phys. Lett. B*, Preprint AZPH-TH/96-08, PAR/LPTHE/96-10, (1996);  
J. Rafelski, J. Letessier and A. Tounsi,  $\alpha_s(M_Z)$  and Strangeness Production to appear in: proceedings of Snowbird Nuclear Dynamics Workshop, February 1996, W. Bauer and G. Westphal, eds., Plenum Press, (New York 1996).
- [76] I. Hinchliffe, *Quantum Chromodynamics*, update August 1995 (URL: <http://pdg.lbl.gov/>), in: L. Montanet et al., *Phys. Rev. D* **50**, 1173 (1994);  
T. Muta, *Foundations of Quantum Chromodynamics*, World Scientific, (Singapore 1987).
- [77] M.A. Samuel, J. Ellis and M. Karliner, *Phys. Rev. Lett.* **74**, 4380 (1995).
- [78] ZEUS Collaboration, *Phys. Lett. B*, **363**, 201 (1995).
- [79] L3 Collaboration, *Study of the structure of hadronic events and determination of  $\alpha_s$  at  $\sqrt{s} = 130$  and  $136$  GeV*, submitted to: *Phys. Lett. B*, CERN preprint PPE/95-192 (1995).
- [80] P. Levai, B. Müller and X.-N. Wang, *Phys. Rev. C* **51**, 3326 (1995).
- [81] I. Sarcevic and P. Valerio, *Phys. Rev. C* **51**, 1433 (1995).
- [82] T. Matsui, B. Svetitsky and L.D. McLerran, *Phys. Rev. D* **34**, 783 (1986).
- [83] H.W. Barz, B.L. Friman, J. Knoll and H. Schulz, *Nucl. Phys. A* **484**, 661 (1988);  
*Nucl. Phys. A* **519**, 831 (1990).
- [84] Y. Takahashi et al. (CERN-EMU05 collaboration), private communication and to be published.